


9 April 2010 | \$10

Science



 AAAS

EDITORIAL

- 137 Cancer Therapy Reform
Arthur D. Levinson

NEWS OF THE WEEK

- 150 NSF Board Draws Flak for Dropping Evolution From *Indicators*
- 151 Scientists Ask Minister to Disavow Predecessor's Book
- 153 Cancer Gene Patents Ruled Invalid
- 154 Candidate Human Ancestor From South Africa Sparks Praise and Debate
>> *Research Articles pp. 195 and 205*
- 155 From *Science's* Online Daily News Site
- 157 Fresh Signs of Volcanic Stirrings Are Radiating From Venus
- 157 Scientists Count the Costs of Chile's Quake
- 158 Asking the Right Question Requires Right Mix of Science and Politics
- 159 From the *Science* Policy Blog

NEWS FOCUS

- 160 EVOLUTION OF BEHAVIOR
Did Working Memory Spark Creative Culture?
Does 'Working Memory' Still Work?
>> *Science Podcast*
- 164 Did Modern Humans Get Smart or Just Get Together?
- 165 Conquering by Copying
A Winning Combination
>> *Research Article p. 208*

LETTERS

- 169 Food Security: Population Controls
A. H. Westing
Food Security: Green Revolution Drawbacks
V. Rull

- Food Security: Beyond Technology
D. W. Bromley
Food Security: Crop Species Diversity
H. Dempewolf et al.
Food Security: GM Crops Threaten Biodiversity
R. Tirado and P. Johnston
Food Security: Rigorous Regulation Required
M. Mellon
Food Security: Focus on Agriculture
J. R. Porter et al.
Food Security: Fossil Fuels
R. E. White and R. Grossman
Food Security: Perception Failures
A. Subramanian et al.

170 CORRECTIONS AND CLARIFICATIONS

BOOKS ET AL.

- 175 The Art of Not Being Governed
J. C. Scott, reviewed by F. Barth

POLICY FORUM

- 177 The Barometer of Life
S. N. Stuart et al.

PERSPECTIVES

- 179 The Microbes Made Me Eat It
D. A. Sandoval and R. J. Seeley
>> *Report p. 228*
- 180 Holding On by a Hard-Shell Thread
P. B. Messersmith
>> *Report p. 216*
- 181 Central Chile Finally Breaks
R. Madariaga et al.
- 183 Probing the Nanoscale
R. F. Cook
- 184 Poisonous Contacts
S. C. Kogan
>> *Report p. 240*
- 185 Graphene Spreads the Heat
R. Prasher
>> *Report p. 213*

CONTENTS continued >>



page 160



page 175

Downloaded from <http://science.sciencemag.org/> on September 13, 2018



COVER

Cranium of *Australopithecus sediba* (specimen UW88-50), a new species of australopithec found at the Malapa site in South Africa. Two partial skeletons, dated to about 1.9 million years ago, share many derived features with *Homo* and may thus shed light on the evolution of that genus. See the related Research Articles on pages 195 and 205 and the related News story on page 154.

Photo: Brett Eloff, courtesy of Lee Berger and the University of the Witwatersrand

DEPARTMENTS

- 133 This Week in *Science*
139 Editors' Choice
144 *Science* Staff
149 Random Samples
252 New Products
253 *Science* Careers

REVIEW

- 187 Four-Dimensional Electron Microscopy
A. H. Zewail

RESEARCH ARTICLES

- 195 *Australopithecus sediba*: A New Species of Homo-Like Australopithec from South Africa
L. R. Berger et al.
>> *Science Podcast*
- 205 Geological Setting and Age of *Australopithecus sediba* from Southern Africa
P. H. G. M. Dirks et al.
A new species of *Australopithecus*, about 1.9 million years old, shows many derived features with *Homo*, helping to reveal its evolution.
>> *News story p. 154*
- 208 Why Copy Others? Insights from the Social Learning Strategies Tournament
L. Rendell et al.
Learning from what others do is more efficient than learning all on one's own.
>> *News story p. 165; Science Podcast*

REPORTS

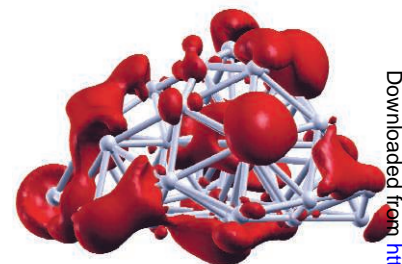
- 213 Two-Dimensional Phonon Transport in Supported Graphene
J. H. Seol et al.
The thermal conductivity of graphene supported on silicon dioxide remains high, despite phonon scattering by the substrate.
>> *Perspective p. 185*
- 216 Iron-Clad Fibers: A Metal-Based Biological Strategy for Hard Flexible Coatings
M. J. Harrington et al.
Marine mussel byssal threads have an outer coating in which proteins are linked to metal ions.
>> *Perspective p. 180*
- 220 Solvent-Mediated Electron Hopping: Long-Range Charge Transfer in $\text{IBr}^-(\text{CO}_2)$ Photodissociation
L. Sheps et al.
The presence of an intervening carbon dioxide molecule dramatically changes the electron transfer probability between two halogen atoms.

- 224 Increased Silver Activity for Direct Propylene Epoxidation via Subnanometer Size Effects
Y. Lei et al.
Clusters of three silver atoms deposited on alumina are active for the low-temperature direct formation of propylene oxide.
- 228 Metabolic Syndrome and Altered Gut Microbiota in Mice Lacking Toll-Like Receptor 5
M. Vijay-Kumar et al.
The innate immune system may promote metabolic health through effects on gut microbes.
>> *Perspective p. 179*
- 232 Variation in Transcription Factor Binding Among Humans
M. Kasowski et al.
Transcription factor binding sites vary among individuals and are correlated with differences in expression.
- 235 Heritable Individual-Specific and Allele-Specific Chromatin Signatures in Humans
R. McDaniell et al.
An appreciable amount of variation in chromatin status and transcription factor binding has a genetic basis.
- 240 Arsenic Trioxide Controls the Fate of the PML-RAR α Oncoprotein by Directly Binding PML
X.-W. Zhang et al.
Arsenic, a drug used clinically for leukemia, binds directly to an oncogenic protein, thereby promoting its degradation.
>> *Perspective p. 184*
- 243 Transnuclear Mice with Predefined T Cell Receptor Specificities Against *Toxoplasma gondii* Obtained via SCNT
O. Kirak et al.
Researchers describe a method to obtain transgenic mice for the study of T cell responses to infectious disease.

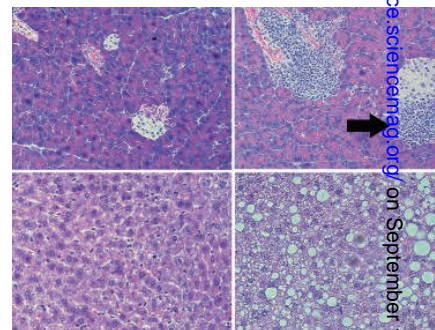
CONTENTS continued >>



pages 180 & 216



page 224



pages 179 & 228

Out of the ages.
Australopithecus sediba
makes its debut.



PALEOANTHROPOLOGY

Candidate Human Ancestor From South Africa Sparks Praise and Debate

“Dad, I found a fossil!”

Lee Berger glanced over at the rock his 9-year-old son, Matthew, was holding and figured the bone sticking out of it was probably that of an antelope, a common find in ancient South African rocks. But when Berger, a paleoanthropologist at the University of the Witwatersrand, Johannesburg, took a closer look, he recognized it as something vastly more important: the collar bone of an ancient hominin. Then he turned the block around and spotted a hominin lower jaw jutting out. “I couldn’t believe it,” he says.

Now on pages 195 and 205 of this issue of *Science*, Berger and his co-workers claim that these specimens, along with numerous other fossils found since 2008 in Malapa cave north of Johannesburg and dated as early as 2 million years ago, are those of a new species dubbed *Australopithecus sediba*. *Sediba* means “wellspring” in the Sesotho language, and Berger’s team argues that the fossils have a mix of primitive features typical of australopithecines and more advanced characteristics typical of later humans. Thus, the team says, the new species may be the best candidate yet for the immediate ancestor of our genus, *Homo*.

That last claim is a big one, and few scientists are ready to believe it themselves just yet. But whether the new hominins are *Homo* ancestors or a side branch of late-surviving australopithecines, researchers agree that because of their completeness—including a skull and many postcranial bones—the fossils offer vital new clues to a murky area in human evolution. “This is a

really remarkable find,” says paleontologist Meave Leakey of the National Museums of Kenya in Nairobi, who thinks it’s an australopithecine. “Very lovely specimens,” says biological anthropologist William Kimbel of Arizona State University (ASU), Tempe, who thinks they are *Homo*.

Such different views of how to classify these fossils reflect a still-emerging debate over whether they are part of our own lineage or belong to a southern African side branch. The oldest *Homo* specimens are scrappy and enigmatic, leaving researchers unsure about the evolutionary steps between the australopithecines and *Homo*. Some think that the earliest fossils assigned to that genus, called *H. habilis* and *H. rudolfensis* and dated to as early as 2.3 million years ago, are really australopithecines. “The transition to *Homo* continues to be almost totally confusing,” says paleoanthropologist Donald Johanson of ASU Tempe, who has seen the new fossils. So it is perhaps no surprise that the experts disagree over whether the new bones represent australopithecines or early *Homo*. And for now, at least, they don’t seem to mind the uncertainty. “All new discoveries make things more confusing” at first, says anthropologist Susan Antón of New York University.

The finds stem from a project Berger embarked on in early 2008 with geologist Paul Dirks, now at James Cook University in Townsville, Australia, to identify new caves likely to hold hominin fossils. Malapa, just 15 kilometers northeast of famous hominin sites such as Sterkfontein, had been explored by lime miners in the early 20th

century; they apparently threw the block that Matthew Berger found out of the cave. (Matthew was originally included as a co-author on one of the papers, but *Science*’s reviewers nixed that idea, Berger says.)

When Berger’s team excavated inside the cave, it found more of that first individual, a nearly complete skull and a partial skeleton of a boy estimated to be 11 or 12 years old, plus an adult female skeleton, embedded in cave sediments. These fossils are reported in *Science*. The researchers also found bones of at least two other individuals, including an infant and another adult female, that are yet to be published.

Dirks enlisted several experts to help date the fossils. Labs in Bern, Switzerland, and Melbourne, Australia, independently performed uranium-lead radiometric dating, taken from cave deposits immediately below the fossils. They yielded dates of 2.024 million and 2.026 million years respectively, with maximum error margins of $\pm 62,000$ years. Paleomagnetic studies suggest that layers holding the fossils were deposited between 1.95 million and 1.78 million years ago, and animal bones found with the hominins were consistent with these dates.

The uranium-lead dating is “credible” and indicates that the fossils are no more than 2 million years old, says geochronologist Paul Renne of the Berkeley Geochronology Center in California, citing the strong reputations of the Bern and Melbourne groups. But Renne regards the paleomagnetic work, which relies on correctly identifying ancient polarity reversals in Earth’s magnetic field, as less convincing. The cave’s stratigraphy might not be complete enough to formally rule out a much younger paleomagnetic signal for the fossils, he says. Geochemist Henry Schwarcz of McMaster University in Hamilton, Canada, notes that the team suggests that the hominin bodies might have been moved by river flows after they fell into the cave from holes in the earth above. If so, the fossils may not be tightly associated with the dated deposits below and above them, Schwarcz says. But Dirks rejects that suggestion, pointing out that the bones were partly articulated with each other, implying that they were buried soon after death.

For now, many researchers are accepting the dates and moving on to consider the team’s hypothesis that *A. sediba* represents a new species transitional between australopithecines and early *Homo*. That idea fits with Berger’s long-held—and controversial—view that *A. africanus*, rather than the earlier species to which

CREDIT: L. BERGER ET AL., SCIENCE

Downloaded from www.sciencemag.org on November 12, 2014

ScienceNOW

“Lucy” belongs, *A. afarensis*, was the true ancestor of *Homo*. (Some of Berger’s other past claims have sparked strong criticism, including a highly publicized 2008 report of small-bodied humans on Palau, which Berger thought might shed light on the tiny hobbits of Indonesia. But other researchers say the Palau bones belong to a normalized modern human population.)

The team’s claims for *A. sediba* are based on its contention that the fossils have features found in both genera. On the australopithecine side, the hominin boy’s brain, which the team thinks had reached at least 95% of adult size, is only about 420 cubic centimeters in volume, less than the smallest known *Homo* brain of about 510 cc. The small body size of both skeletons, a maximum of about 1.3 meters, is typical of australopithecines, as are the relatively long arms. The team says *A. sediba* most resem-



Fossil finder. Nine-year-old Matthew Berger at the moment of discovery at Malapa cave.

bles *A. africanus*, which lived in South Africa between about 3.0 million and 2.4 million years ago and is the most likely ancestor for the new species.

But *A. sediba* differs from *A. africanus* in traits that also link it to *Homo*. Compared with other australopithecines, *A. sediba* has smaller teeth, less pronounced cheekbones, and a more prominent nose, as well as longer legs and changes in the pelvis similar to those seen in later *H. erectus*. This species, also known in Africa as *H. ergaster* and considered an ancestor of *H. sapiens*, first appears in Africa about 1.9 million years ago. Some features of *A. sediba*’s pelvis, such as the ischium (bottom portion), which

is shorter than in australopithecines, “do look like they are tending more in a *Homo* direction,” says Christopher Ruff, a biological anthropologist at Johns Hopkins Medical School in Baltimore, Maryland.

The claimed *Homo*-like features suggest to some people that the fossils belong in that genus rather than *Australopithecus*. “I would have been happier with a *Homo* designation,” based on the small size of the teeth and also their detailed structure, such as the shape of their cusps, says Antón. “It’s *Homo*,” agrees Johanson, citing features such as the relative thinness of the hominin’s lower jaw.

But others are unconvinced by the *Homo* argument. The characteristics shared by *A. sediba* and *Homo* are few and could be due to normal variation among australopithecines or because of the boy’s juvenile status, argues Tim White, a paleoanthropologist at the University of California, Berkeley. These characters change as a hominin grows, and the features of a young australopithecine could mimic those of ancient adult humans. He and others, such as Ron Clarke of Witwatersrand, think the new fossils might represent a late-surviving version of *A. africanus* or a closely related sister species to it, and so will be chiefly informative about that lineage. “Given its late age and *Australopithecus*-grade anatomy, it contributes little to the understanding of the origin of genus *Homo*,” says White.

Putting *A. sediba* into *Homo* would require “a major redefinition” of that genus, adds paleoanthropologist Chris Stringer of the Natural History Museum in London. At no earlier than 2 million years old, *A. sediba* is younger than *Homo*-looking fossils elsewhere in Africa, such as an upper jaw from Ethiopia and a lower jaw from Malawi, both dated to about 2.3 million years ago. Berger and his co-workers agree that the Malapa fossils themselves cannot be *Homo* ancestors but suggest that *A. sediba* could have arisen somewhat earlier, with the Malapa hominins being late-surviving members of the species.

The team thought long and hard about putting the fossils into *Homo* but decided that given the small brain and other features, the hominin was “australopithecine-grade,” says team member Steven Churchill of Duke University in Durham, North Carolina. However they are classified, the Malapa finds “are important specimens in the conversation” about the origins of our genus, says Antón, and “will have to be considered in the solution.”

—MICHAEL BALTER

From *Science’s* Online Daily News Site

Mass of the Common Quark Finally Nailed Down

Using supercomputers and mind-bogglingly complex simulations, researchers have calculated the masses of particles called “up quarks” and “down quarks” that make up protons and neutrons with 20 times greater precision than the previous standard. The new numbers could be a boon to theorists trying to decipher particle collisions at atom smashers like Europe’s Large Hadron Collider or trying to develop deeper theories of the structure of matter.

<http://bit.ly/commonquark>

Notorious Drug Stanches Bleeding

Despite its horrifying history of causing birth defects, thalidomide has recently made a comeback as a treatment for diseases such as the cancer multiple myeloma. Now, a new study suggests that the drug may also ease the symptoms of a genetic disease called hereditary hemorrhagic telangiectasia—a discovery that could guide researchers to novel therapies for HHT and other vascular diseases.

<http://bit.ly/goodthalidomide>

Wind Turbines Would Support A Stable Grid

Individual wind turbines and even whole wind farms remain at the mercy of local weather for how much electricity they can generate. But researchers have confirmed that linking up such farms along the entire U.S. East Coast could provide a surprisingly consistent source of power. In fact, such a setup could someday replace much of the region’s existing generating capacity, which is based on coal, natural gas, nuclear reactors, and oil. <http://bit.ly/windnetwork>

That Tortilla Costs More Than You Think

Which costs more, a dollar’s worth of sugar or a dollar’s worth of paint? That’s not a trick question: The sugar costs more, if you count the liters of water that go into making it, according to a new study. Uncovering the water behind the dollars in sectors including cotton farming and moviemaking could help industries use water more wisely.

<http://bit.ly/watercost>

Read the full postings, comments, and more at news.sciencemag.org/sciencenow.

Australopithecus sediba: A New Species of *Homo*-Like Australopith from South Africa

Lee R. Berger,^{1,2*} Darryl J. de Ruiter,^{3,1} Steven E. Churchill,^{4,1} Peter Schmid,^{5,1} Kristian J. Carlson,^{1,6} Paul H. G. M. Dirks,^{2,7} Job M. Kibii¹

Despite a rich African Plio-Pleistocene hominin fossil record, the ancestry of *Homo* and its relation to earlier australopithecines remain unresolved. Here we report on two partial skeletons with an age of 1.95 to 1.78 million years. The fossils were encased in cave deposits at the Malapa site in South Africa. The skeletons were found close together and are directly associated with craniodental remains. Together they represent a new species of *Australopithecus* that is probably descended from *Australopithecus africanus*. Combined craniodental and postcranial evidence demonstrates that this new species shares more derived features with early *Homo* than any other australopith species and thus might help reveal the ancestor of that genus.

The origin of the genus *Homo* is widely debated, with several candidate ancestors being proposed in the genus *Australopithecus* (1–3) or perhaps *Kenyanthropus* (4). The earliest occurrence of fossils attributed to *Homo* (*H. aff. H. habilis*) at 2.33 million years ago (Ma) in Ethiopia (5) makes it temporally antecedent to all other known species of the genus *Homo*. Within early *Homo*, the hypodigms and phylogenetic relationships between *H. habilis* and another early species, *H. rudolfensis*, remain unresolved (6–8), and the placement of these species within *Homo* has been challenged (9). *H. habilis* is generally thought to be the ancestor of *H. erectus* (10–13), although this might be questioned on the basis of the considerable temporal overlap that existed between them (14). The identity of the direct ancestor of the genus *Homo*, and thus its link to earlier *Australopithecus*, remains controversial. Here we describe two recently discovered, directly associated, partially articulated *Australopithecus* skeletons from the Malapa site in South Africa, which allow us to investigate several competing hypotheses regarding the ancestry of *Homo*. These skeletons cannot be accommodated within any existing fossil taxon; thus, we establish a new species, *Australopithecus sediba*, on the basis of a com-

ination of primitive and derived characters of the cranium and postcranium.

The following is a description of *Au. sediba*: Order Primates Linnaeus 1758; suborder Anthropoidea Mivart 1864; superfamily Hominoidea Gray 1825; family Hominidae Gray 1825; genus *Australopithecus* DART 1925; species *Australopithecus sediba* sp. nov.

Etymology. The word *sediba* means “fountain” or “wellspring” in the seSotho language.

Holotype and paratype. Malapa Hominin 1 (MH1) is a juvenile individual represented by a partial cranium, fragmented mandible, and partial postcranial skeleton that we designate as the species holotype [Figs. 1 and 2, supporting online material (SOM) text S1, figs. S1 and S2, and table S1]. The first hominin specimen recovered from Malapa was the right clavicle of MH1 (UW88-1), discovered by Matthew Berger on 15 August 2008. MH2 is an adult individual represented by isolated maxillary teeth, a partial mandible, and partial postcranial skeleton that we designate as the species paratype. Although MH1 is a juvenile, the second molars are already erupted and in occlusion. Using either a human or an ape model, this indicates that MH1 had probably attained at least 95% of adult brain size (15). Although additional growth would have occurred in the skull and skeleton of this individual, we judge that it would not have appreciably altered the morphology on which this diagnosis is based.

Locality. The two *Au. sediba* type skeletons were recovered from the Malapa site (meaning “homestead” in seSotho), situated roughly 15 km NNE of the well-known sites of Sterkfontein, Swartkrans, and Kromdraai in Gauteng Province, South Africa. Detailed information regarding geology and dating of the site is in (16).

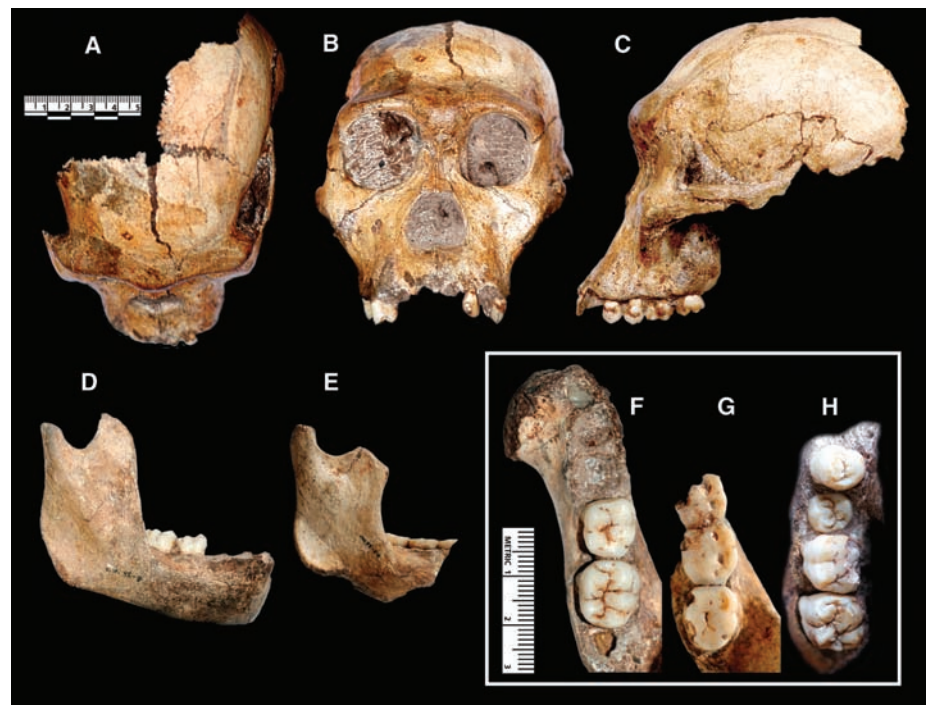


Fig. 1. Craniodental elements of *Au. sediba*. UW88-50 (MH1) juvenile cranium in (A) superior, (B) frontal, and (C) left lateral views. (D) UW88-8 (MH1) juvenile mandible in right lateral view, (E) UW88-54 (MH2) adult mandible in right lateral view, (F) UW88-8 mandible in occlusal view, (G) UW88-54 mandible in occlusal view, and (H) UW88-50 right maxilla in occlusal view (scale bars are in centimeters).

¹Institute for Human Evolution, University of the Witwatersrand, Private Bag 3, Wits 2050, South Africa. ²School of Geosciences, University of the Witwatersrand, Private Bag 3, Wits 2050, South Africa. ³Department of Anthropology, Texas A&M University, College Station, TX 77843, USA. ⁴Department of Evolutionary Anthropology, Box 90383, Duke University, Durham, NC 27708, USA. ⁵Anthropological Institute and Museum, University of Zürich, Winterthurerstrasse 190, CH-8057 Zürich, Switzerland. ⁶Department of Anthropology, Indiana University, Bloomington, IN 47405, USA. ⁷School of Earth and Environmental Sciences, James Cook University, Townsville, Queensland 4811, Australia.

*To whom correspondence should be addressed. E-mail: profleeberger@yahoo.com

Diagnosis. *Au. sediba* can be distinguished from other species of *Australopithecus* by a combination of characters presented in Table 1; comparative cranial measures are presented in Table 2. A number of derived characters separate *Au. sediba* from the older chronospecies *Au. anamensis* and *Au. afarensis*. *Au. sediba* exhibits neither the extreme megadontia, extensive cranial cresting, nor facial prognathism of *Au. garhi*. The suite of derived features characterizing *Au. aethiopicus*, *Au. boisei*, and *Au. robustus*, in particular the pronounced cranial muscle markings, derived facial morphology, mandibular corpus robusticity, and postcanine megadontia, are absent in *Au. sediba*. The closest morphological comparison for *Au. sediba* is *Au. africanus*, as these taxa share numerous similarities in the cranial vault, facial skeleton, mandible, and teeth (Table 1). Nevertheless, *Au. sediba* can be readily differentiated from *Au. africanus* on both craniodental and postcranial evidence. Among the more notable differences, we observe that although the cranium is small, the vault is relatively transversely expanded with vertically oriented parietal walls and widely spaced temporal lines; the face lacks the pro-

nounced, flaring zygomatics of *Au. africanus*; the arrangement of the supraorbital torus, nasoalveolar region, infraorbital region, and zygomatics result in a derived facial mask; the mandibular symphysis is vertically oriented with a slight bony chin and a weak post-incisive planum; and the teeth are differentiated by the weakly defined buccal grooves of the maxillary premolars, the weakly developed median lingual ridge of the mandibular canine, and the small absolute size of the postcanine dentition. These exact differences also align *Au. sediba* with the genus *Homo* (see SOM text S2 for hypodigms used in this study). However, we consider *Au. sediba* to be more appropriately positioned within *Australopithecus*, based on the following craniodental features: small cranial capacity, pronounced glabellar region, patent premaxillary suture, moderate canine jugum with canine fossa, small anterior nasal spine, steeply inclined zygomaticoalveolar crest, high masseter origin, moderate development of the mesial marginal ridge of the maxillary central incisor, and relatively closely spaced premolar and molar cusps.

Postcranially, *Au. sediba* is similar to other australopiths in its small body size, its relatively

long upper limbs with large joint surfaces, and the retention of apparently primitive characteristics in the upper and lower limbs (table S2). *Au. sediba* differs from other australopiths, but shares with *Homo* a number of derived features of the os coxa, including increased buttressing of the ilium and expansion of its posterior portion, relative reduction in the distance between the sacroiliac and hip joints, and reduction of distance from the acetabulum to the ischial tuberosity. These synapomorphies with *Homo* anticipate the reorganization of the pelvis and lower limb in *H. erectus* and possibly the emergence of more energetically efficient walking and running in that taxon (17). As with the associated cranial remains, the postcranium of *Au. sediba* is defined not by the presence of autapomorphic features but by a unique combination of primitive and derived traits.

Cranium. The cranium is fragmented and slightly distorted. The minimum cranial capacity of MH1 is estimated at 420 cm³ (SOM text S4). The vault is ovoid, with transversely expanded, vertically oriented parietal walls. The widely spaced temporal lines do not approach the midline. Postorbital constriction is slight. The weakly arched supraorbital torus is moderately developed and laterally extended, with sharply angled lateral corners and a weakly defined supratoral sulcus. A robust glabellar region is evident, with only a faint depression of the supraorbital torus at the midline. The frontal process of the zygomatic faces primarily laterally and is expanded medially but not laterally. The zygomatic prominence does not show antero-lateral expansion. The zygomatics are weakly flared laterally, resulting in an uninterrupted frontal profile of the facial mask that is squared superiorly and tapered inferiorly. The zygomaticoalveolar crests are long, straight, and steeply inclined, resulting in a high masseter origin. The root of the zygomatic begins at the anterior margin of M¹. The nasal bones are widened superiorly, become narrowest about one-third of the way down, and flare to their widest extent at their inferior margin. The nasal bones are elevated as a prominent ridge at the internasal suture, with an increasingly anterior projection inferiorly. The bone surface of the maxilla retreats gently away from the nasal aperture laterally, resulting in an everted margin of the superolateral portion of the aperture relative to the infraorbital region. The inferolateral portion of the nasal aperture becomes bluntly rounded. The infraorbital region is slightly convex (18) and is oriented at an approximately right angle to the alveolar plane. There is a trace of a premaxillary suture near the superolateral margin of the nasal aperture. Prominent canine juga delineate moderately developed canine fossae. Anterior pillars are absent. The inferior margin of the nasal aperture is marked by a stepped nasal sill and a small but distinct anterior nasal spine. The subnasal region is straight in the coronal plane and only weakly projecting relative

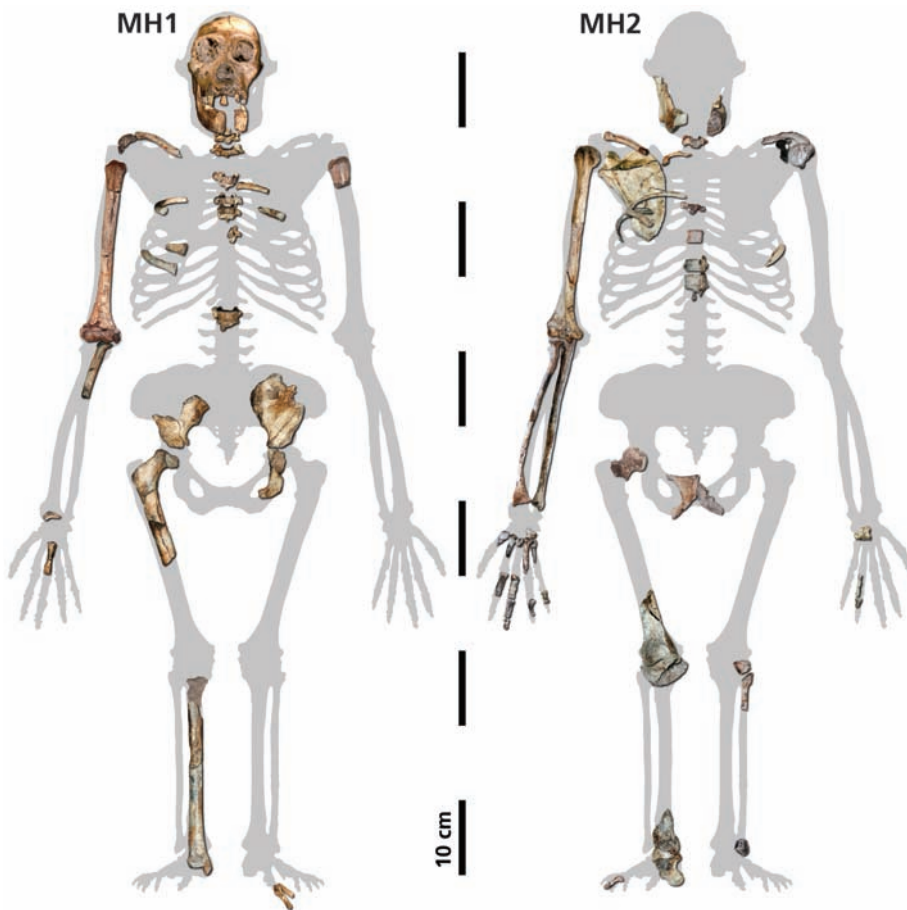


Fig. 2. Associated skeletal elements of MH1 (left) and MH2 (right), in approximate anatomical position, superimposed over an illustration of an idealized *Au. africanus* skeleton (with some adjustment for differences in body proportions). The proximal right tibia of MH1 has been reconstructed from a natural cast of the proximal metaphysis.

Table 1. List of characters used to diagnose *Au. sediba*. These characters are commonly used in hominin phylogenetic studies (11, 38–40) or have been recorded as diagnostic for various hominin taxa in the past (3, 10, 36). Recognizing the potential pitfalls of performing a cladistic analysis on possibly interdependent characters of uncertain valence, we produced a cladogram from the data in this table as a test of the phylogenetic position of *Au. sediba* (fig. S3). Our most parsimonious cladogram places *Au. sediba* at the stem of the *Homo* clade.

Characters	<i>Au. gfarensis</i>	<i>Au. garhi</i>	<i>Au. africanus</i>	<i>Au. sediba</i>	<i>H. habilis</i>	<i>H. rudolfensis</i>	<i>H. erectus</i>	<i>Au. aethiopicus</i>	<i>Au. boisei</i>	<i>Au. robustus</i>
Vault										
Cranial capacity (1)	Small	Small	Small	Small	Intermed.	Large	Large	Small	Small	Small
A-M incursion of temporal lines on frontal bone (9)	Strong	Moderate	Moderate	Weak	Weak	Weak	Weak	Strong	Strong	Strong
Position of temporal lines on parietal bones	Crest	Crest	Variable	Wide	Variable	Wide	Wide	Crest	Crest	Crest
Compound temporal nuchal crest (males)	Extensive	?	Absent	Absent	Variable	Absent	Absent	Extensive	Variable	Absent
Postorbital constriction (5)	Marked	Moderate	Moderate	Slight	Moderate	Moderate	Slight	Marked	Marked	Marked
Pneumatization of temporal squama	Extensive	?	Extensive	Reduced	Reduced	Reduced	Reduced	Extensive	Variable	Reduced
Facial hafting	Low	Low	Low	Low	Low	Low	Low	High	High	High
Frontal trigon	Present	Present	Absent	Absent	Absent	Absent	Absent	Present	Present	Present
Supraglenoid gutter width	Narrow	?	Narrow	Narrow	Narrow	Narrow	Narrow	Wide	Wide	Wide
Horizontal distance between TMJ and M2/M3 (6)	Long	?	Long	Short	Short	Long	Short	Long	Long	Long
Parietal transverse expansion/tuber	Absent	Absent	Absent	Present	Present	Present	Present	Absent	Absent	Absent
Facial skeleton										
Supraorbital expression	Costa supr.	Costa supr.	Intermed.	Torus	Torus	Intermed.	Torus	Costa supr.	Costa supr.	Costa supr.
Supraorbital contour	Less arched	Less arched	Variable	Arched	Arched	Arched	Arched	Less arched	Variable	Arched
Glabellar region forms as prominent block	No	No	Variable	Yes	No	Variable	No	No	Yes	Yes
Lat. half of infraorbital margin blunt	No	?	No	No	No	No	No	Yes	No	Yes
Zygomatic arch relative to inferior orbital margin	Above	?	Level	Level	Level	?	Level	Above	Above	Above
Convexity/concavity of infraorbital region	?	?	Convex	Convex	Concave	Concave	Convex	Concave	Concave	Concave
Nasal bone projection above frontomaxillary suture	Expanded	?	Variable	No	No	No	No	Tapered	Expanded	Expanded
Inferior width of projecting nasal bone (25)	Wide	?	Variable	Wide	Variable	Narrow	Wide	Not proj.	Not proj.	Not proj.
Infraorbital foramen height (32)	High	?	Variable	High	High	?	High	Low	Low	Low

continued on next page

Characters	<i>Au. afarensis</i>	<i>Au. garhi</i>	<i>Au. africanus</i>	<i>Au. sediba</i>	<i>H. habilis</i>	<i>H. rudolfensis</i>	<i>H. erectus</i>	<i>Au. aethiopicus</i>	<i>Au. boisei</i>	<i>Au. robustus</i>
Canine jugs prominence/anterior pillars	Prominent	Prominent	Variable	Prominent	Variable	Weak	Weak	Weak	Weak	Pillars
Patency of premaxillary suture	Obliterated	?	Occasional	Trace	Obliterated	Obliterated	Obliterated	Obliterated	Obliterated	Occasional
Inferolateral nasal aperture margin	Sharp	Sharp	Variable	Blunt	Variable	Sharp	Blunt	Blunt	Variable	Blunt
Eversion of superior nasal aperture margin	?	?	None	Slight	Slight	Slight	Slight	Slight	Variable	None
Nasoalveolar triangular frame/gutter	Triangular	?	Triangular	Triangular	Triangular	Triangular	Triangular	Gutter	Gutter	Gutter
Nasal cavity entrance	Stepped Convex	Stepped Convex	Stepped Straight	Stepped Straight	Variable Straight	Stepped Straight	Stepped Straight	Smooth Concave	Smooth Concave	Smooth Concave
Nasoalveolar clivus contour in coronal plane	Marked Present	Marked Present	Variable Present	Weak Present	Variable Present	Weak Absent	Weak Absent	Marked Absent	Moderate Absent	Moderate Absent
Canine fossa	Absent	Absent	Absent	Absent	Absent	Absent	Absent	Absent	Absent	Present
Maxillary fossula	Procumb.	Procumb.	Variable	Vertical	Variable	Vertical	Vertical	Vertical	Vertical	Vertical
Incisor procumbency	Absent	?	Anterior	Anterior	Anterior	?	Enlarged	Posterior	Posterior	Posterior
Anterior nasal spine rel. to nasal aperture	Med. and lat.	?	Med. and lat.	Medial	Medial	Medial	Medial	Med. and lat.	Med. and lat.	Med. and lat.
Expansion of frontal process of zygomatic bone	?	?	Indented	Curved	Curved	Curved	Curved	?	Curved	Curved
Angular indentation of lateral orbital margin	Prominent	?	Prominent	Slight	Slight	?	Slight	Prominent	Prominent	Prominent
Zygomatic prominence development	Marked	?	Marked	Slight	Slight	Slight	Slight	Marked	Marked	Marked
Lateral flaring of zygomatic arches	Tapered	?	Tapered	Squared	Squared	Squared	Squared	Tapered	Tapered	Tapered
Outline of superior facial mask	Straight	?	Straight	Straight	Notch	Notch	Notch	Straight	Straight	Straight
Zygomatocoalveolar crest/malar notch	Obtuse	?	Obtuse	Right	Right	Right	Right	Obtuse	Obtuse	Obtuse
Infraorbital plate angle relative to alveolar plane	No	?	No	No	No	No	No	No	No	Yes
Zygomatocomaxillary steps and fossae present	Low	Low	High	High	Low	Low	Low	High	High	High
Height of masseter origin (35)	Thin	?	Thin	Thin	Thin	?	Thin	Thick	Thick	Thick
Malar thickness (31) relative to zygomatics	Posterior	Posterior	Variable	Posterior	Posterior	Level	Posterior	Anterior	Anterior	Anterior
Facial prognathism (7) (sellion-prosthion angle)	Prognathic	Prognathic	Variable	Mesognath.	Mesognath.	Mesognath.	Orthogn.	Prognathic	Mesognath.	Mesognath.
Masseteric position relative to sellion	Anterior	?	Posterior	Posterior	Posterior	?	Posterior	Anterior	Anterior	Anterior
Lateral anterior facial contour	Bipartite	Bipartite	Variable	Straight	Variable	Straight	Straight	Straight	Straight	Straight

Characters	<i>Au. afarensis</i>	<i>Au. garhi</i>	<i>Au. africanus</i>	<i>Au. sediba</i>	<i>H. habilis</i>	<i>H. rudolfensis</i>	<i>H. erectus</i>	<i>Au. aethiopicus</i>	<i>Au. boisei</i>	<i>Au. robustus</i>
Palate										
Protrusion of incisors beyond bi-canine line	Yes	Yes	Yes	Yes	Yes	No	Yes	No	No	No
Anterior palatal depth	Shallow	Shallow	Deep	Deep	Variable	Deep	Variable	Shallow	Deep	Shallow
Dental arcade shape	Rectangle Present	Rectangle Present	Variable Absent	Parabolic Absent	Parabolic Variable	Parabolic Absent	Parabolic Absent	Rectangle Absent	Parabolic Absent	Parabolic Absent
Maxillary I2/C diastema										
Mandible										
Orientation of mandibular symphysis	Receding	?	Receding	Vertical	Vertical	Vertical	Vertical	Vertical	Vertical	Vertical
Bony chin (<i>mentum osseum</i>)	Absent	?	Slight	Slight	Slight	Slight	Slight	Slight	Slight	Slight
Direction of mental foramen opening	Variable	?	Variable	Lateral	Lateral	Lateral	Lateral	Lateral	Lateral	Lateral
Post-incisive planum	Prominent	?	Prominent	Weak	Prominent	Weak	Weak	Prominent	Prominent	Prominent
Torus marginalis and marginal tubercles	Prominent	?	Moderate	Moderate	Moderate	Prominent	Prominent	?	Prominent	Prominent
Mandibular corpus	Small	?	Small	Small	Small	Variable	Small	Large	Large	Large
cross-sectional area at M ₁ (50)										
Teeth										
Incisor-to-postcanine ratio (maxillary) (60)	Large	Moderate	Moderate	Moderate	Moderate	Moderate	Large	?	Small	Small
Canine-to-postcanine ratio (maxillary/mandibular) (61, 62)	Large	Large	Large	Large	Large	Large	Large	?	Small	Small
Postcanine crown area (maxillary/mandibular) (57, 59)	Moderate	Large	Large	Moderate	Moderate	Large	Small	Large	Large	Large
Maxillary I ¹ : MMR development, lingual face	Moderate	?	Moderate	Moderate	Weak	Weak	Weak	?	Moderate	Moderate
Maxillary C: development of lingual ridges	Marked	Marked	Marked	Weak	Weak	Marked	Marked	?	Marked	Weak
Maxillary premolar molarization	None	Minor	Minor	None	Minor	Minor	None	Marked	Marked	Marked
Maxillary premolars: buccal grooves	Marked	Marked	Marked	Weak	Weak	Marked	Weak	?	Weak	Weak
Median lingual ridge of mandibular canine	Prom.	?	Prom.	Weak	Weak	Weak	Weak	?	Weak	Weak
Mandibular P ₃ root number	2	?	2	2	1	2	1	?	2	2
Protoconid/metaconid more mesial cusp (molars)	Equal	?	Equal	Protoconid	Protoconid	Protoconid	Protoconid	?	Equal	Equal
Peak of enamel forms between roots of molars	No	?	Yes	Yes	No	No	No	?	No	Yes
Relative enamel thickness	Thick	Thick	Thick	Thick	Thick	Thick	Thick	Hyper	Hyper	Hyper
Positions of apices of lingual (LC) and buccal (BC) cusps of premolars and molars relative to occlusal margin	LC at margin, BC slightly lingual	margin, BC slightly lingual	LC slightly buccal, BC moderately lingual	LC slightly buccal, BC moderately lingual	margin, BC slightly lingual	margin, BC slightly lingual	margin, BC slightly lingual	buccal, BC strongly lingual	buccal, BC strongly lingual	buccal, BC strongly lingual

Item	Measurement description in (6)	Measurement	Au. afarensis	Au. africanus	Au. sediba	H. habilis	H. rudolfensis	H. erectus	Au. aethiopicus	Au. boisei	Au. robustus
41		Intercanine distance	26	30	30	30	33	31	—	29	27
42		Palate breadth (ekm-ekm)	68	64	63	70	80	66	83	82	67
43		Mandibular symphysis height	39	38	32	27	36	34	—	47	42
44		Mandibular symphysis depth	60	20	19	19	24	19	—	28	25
45		Mandibular corpus height at P ₄	34	33	28	30	38	30	—	42	38
46		Mandibular corpus depth at P ₄	19	21	18	20	22	19	—	28	24
47		Cross-sectional area at P ₄ (calculated as an ellipse)	511	558	382	427	653	458	—	910	709
48		Mandibular corpus height at M ₁	33	32	28	29	36	30	35	41	37
49		Mandibular corpus depth at M ₁	19	21	18	20	23	20	26	28	26
50		Cross-sectional area at M ₁ (calculated as an ellipse)	488	532	396	421	667	469	715	913	759
51		Mandibular corpus height at M ₂	31	31	25	31	36	30	—	41	35
52		Mandibular corpus depth at M ₂	22	25	22	23	26	21	—	31	28
53		Cross-sectional area at M ₂ (calculated as an ellipse)	536	612	436	537	745	504	—	980	770
54		Height of mental foramen relative to alveolar margin	20	19	13	13	17	13	—	20	20
55		Maxillary incisor crown area (I ¹ +I ²)	143	135	109	132	137	136	—	117	109
56		Maxillary canine crown area	107	104	79	95	118	96	—	76	79
57		Maxillary postcanine crown area	713	868	731	755	829	617	—	1012	941
58		Mandibular canine crown area	87	95	68	83	—	79	—	72	61
59		Mandibular molar crown area	550	651	536	565	668	466	—	781	678
60		Maxillary incisor to postcanine ratio	20.0	15.6	14.9	17.4	16.6	22.1	—	11.5	11.6
61		Maxillary canine to postcanine ratio	15.0	11.9	10.8	12.6	14.2	15.5	—	7.5	8.4
62		Mandibular canine to molar ratio	15.8	14.6	12.7	14.6	—	16.7	—	9.2	9.0

to the facial plane. The face is mesognathic. The palate is consistently deep along its entire extent, with a parabolic dental arcade.

Mandible. Descriptions apply to the more complete juvenile (MH1) mandible unless otherwise stated. The nearly vertical mandibular symphysis presents a weak lateral tubercle, resulting in a slight mental trigone, and a weak mandibular incurvation results in a slight *mentum osseum*. The post-incisive planum is weakly developed and almost vertical. Both mandibular corpora are relatively gracile, with a low height along the alveolar margin. The extramolar sulcus is relatively narrow in both mandibles. In MH1, a moderate lateral prominence displays its greatest protrusion at the mesial extent of M₂, with a marked decrease in robusticity to P₄; in MH2 the moderate lateral prominence shows its greatest protrusion at M₃, with a marked decrease in robusticity to M₂. The alveolar prominence is moderately deep with a notable medial projection posteriorly. The anterior and posterior subalveolar fossae are continuous. The ramus of MH1 is tall and narrow, with nearly parallel, vertically oriented anterior and posterior borders; the ramus of MH2 is relatively broader, with nonparallel anterior and posterior borders (fig. S2). The mandibular notch is relatively deep and narrow in MH1 and more open in MH2. The coronoid extends farther superiorly than the condyle. The condyle is mediolaterally broad and anteroposteriorly narrow. The endocondyloid buttress is absent in MH1, whereas in MH2 a weak endocondyloid buttress approaches the condyle without reaching it.

Dental size and proportions. The dentition of the juvenile (MH1) is relatively small, whereas preserved molars of the adult (MH2) are even smaller (Fig. 3 and fig. S4). For MH1, the maxillary central incisor is distinguishable only from the reduced incisors of *Au. robustus*. The maxillary canine is narrower than all canines of *Au. africanus* except TM 1512, whereas the mandibular canine falls well below the range of *Au. africanus*. Premolars and molars are at the lower end of the *Au. africanus* range and within that of *H. habilis*–*H. rudolfensis* and *H. erectus*. Molar dimensions of the adult individual (MH2) are smaller than those of *Au. africanus*, are at or below the range of those of *H. habilis*–*H. rudolfensis*, and are within the range of those of *H. erectus*. *Au. sediba* mirrors the *Au. africanus* pattern of maxillary molars that increase slightly in size posteriorly, though it differs in that the molars tend to be considerably larger in the latter taxon. Conversely, the *Au. sediba* pattern varies slightly from that seen in specimens KNM-ER 1813, OH 13, and OH 65 and *H. erectus*, wherein the molars increase from M¹ to M² but then decrease to M³. In broad terms, the teeth of *Au. sediba* are similar in size to teeth of specimens assigned to *Homo* but share the closely spaced cusp apices seen in *Australopithecus*.

Postcranium. Preserved postcranial remains of *Au. sediba* (table S1) denote small-bodied

hominins that retain an australopith pattern of long upper limbs, a high brachial index, and relatively large upper limb joint surfaces (table S2). In addition to these aspects of limb and joint proportions, numerous other features in the upper limb are shared with sibling species of *Australopithecus* (to the exclusion of later *Homo*), including a scapula with a cranially oriented glenoid fossa and a strongly developed axillary border; a prominent conoid tubercle on the clavicle, with a pronounced angular margin; low proximal-to-distal humeral articular proportions; a distal humerus with a marked crest for the brachioradialis muscle, a large and deep olecranon fossa with a septal aperture, and a marked trochlear/capitulum keel (19); an ulna with a pronounced flexor carpi ulnaris tubercle; and long, robust, and curved manual phalanges that preserve strong attachment sites for the flexor digitorum superficialis muscle.

Numerous features of the hip, knee, and ankle indicate that *Au. sediba* was a habitual biped. In terms of size and morphology, the proximal and distal articular ends of the femur and tibia fall within the range of variation of specimens attributed to *Au. africanus*. However, several derived features in the pelvis link the Malapa specimens with later *Homo*. In the os coxa (Fig. 4), *Au. sediba* shares with *Homo* a pronounced acetabulocrystal buttress; a more posterior position of the crystal tubercle; a superoinferiorly extended posterior iliac blade, with an expanded retroauricular area; a sigmoid-shaped anterior inferior iliac spine; a reduced lever arm for weight transfer between the auricular surface and the acetabulum; an enlarged and rugose iliofemoral ligament attachment area; a tall and thin pubic symphyseal face; and a relatively short ischium with a deep and narrow tuberoacetabular sulcus. These features are present in taxonomically un-

assigned postcranial remains from Koobi Fora (KNM-ER 3228) and Olduvai Gorge (OH 28), which have been argued to represent early *Homo* (20), as well as in early *Homo erectus* (21). An os coxa from Swartkrans (SK 3155) has been considered by some to also represent early *Homo* (22) but can be seen to possess the australopith pattern in most of these features. In addition, *Au. sediba* shares with later *Homo* the human-like pattern of low humeral-to-femoral diaphyseal strength ratios, in contrast to the ape-like pattern seen in the *H. habilis* specimen OH 62 (table S2).

Although aspects of the pelvis are derived, the foot skeleton is more primitive overall, sharing with other australopiths a flat talar trochlea articular surface with medial and lateral margins with equal radii of curvature, and a short, stout, and medially twisted talar neck with a high horizontal angle and a low neck torsion angle

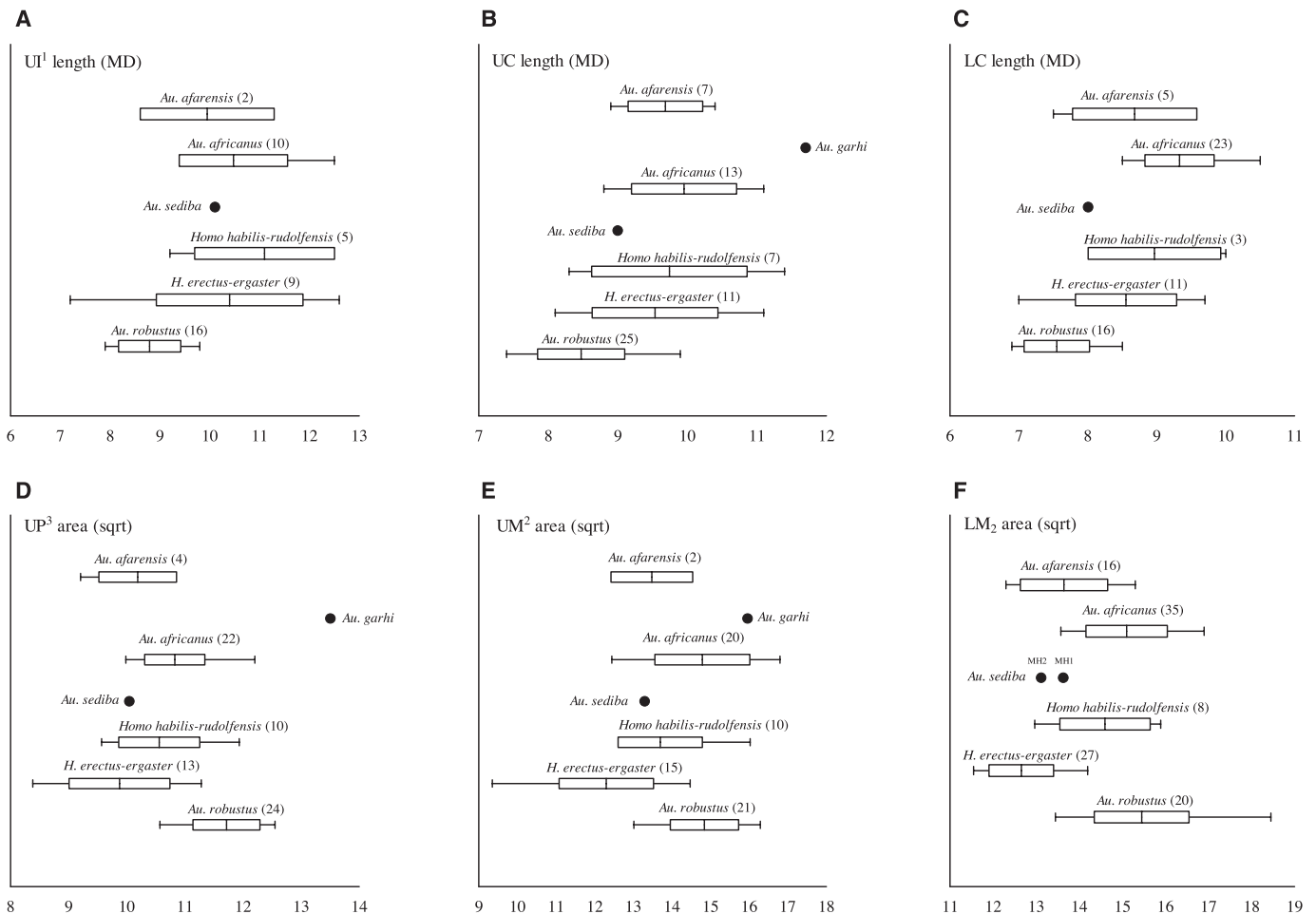


Fig. 3. Dental size of a selection of *Au. sediba* teeth compared to other early hominin taxa; see fig. S4 for additional teeth. Dental measurements were taken as described by Wood (6). Owing to small sample sizes, *H. habilis* and *H. rudolfensis* were combined. (A) Upper central incisor mesiodistal (MD) length. (B) Upper canine MD length. (C) Lower canine MD length. (D) Square root of calculated [MD \times BL (BL, buccolingual)] upper third premolar area. (E) Square root of calculated (MD \times BL) upper second molar area. (F) Square root of calculated (MD \times BL) lower second molar area. Measures were taken on original specimens by D.J.D. for *Au. africanus*, *Au. robustus*,

and *Au. sediba*. Measurements for *Au. afarensis*, *H. habilis*, *H. rudolfensis*, and *H. erectus* are from (6). P^4 is not fully erupted on the right side of MH1, therefore measures of the maxillary postcanine dentition are presented for the left side only. Dental metrics for *Au. sediba* are as follows (MD, BL, in millimeters): Maxillary: MH1: RI1 10.1, 6.9; LI2 7.7 (damaged), 5.1; RC 9.0, 8.8; LP3 9.0, 11.2; LP4 9.2, 12.1; LM1 12.9, 12.0; LM2 12.9, 13.7; LM3 13.3, 14.1; MH2: RM3 11.3, 12.9. Mandibular: MH1: LC 8.0, 8.5; RM1 12.5, 11.6; RM2 14.4, 12.9; RM3 14.9, 13.8; MH2: RM1 11.8, 11.1; RM2 14.1, 12.2; RM3 14.2, 12.7; LM3 14.1, 12.5.

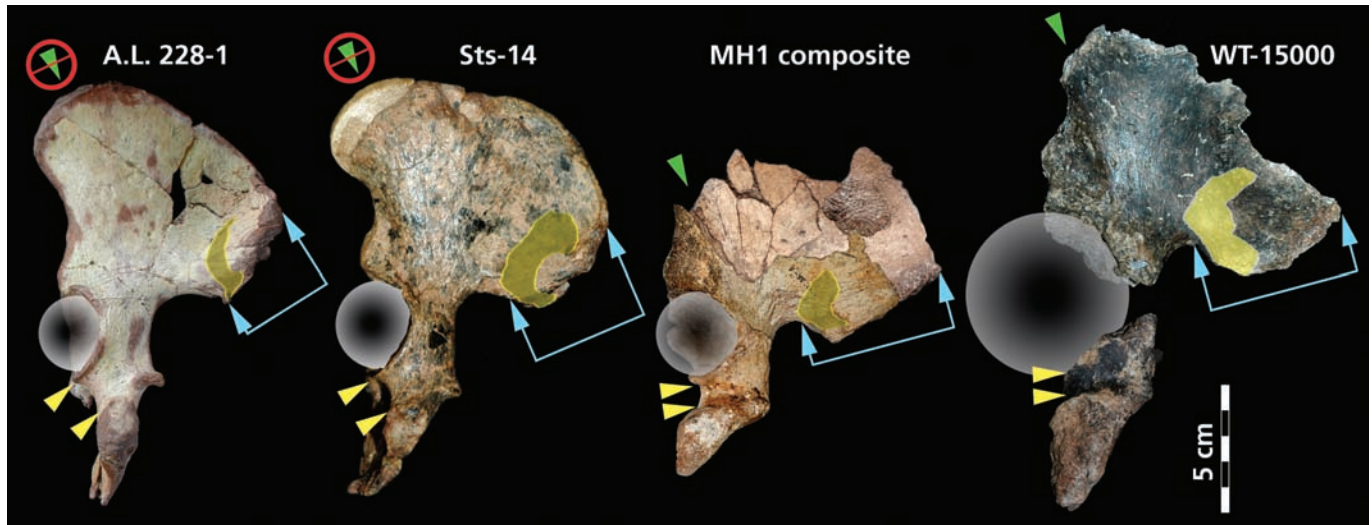


Fig. 4. Representative ossa coxae, in lateral view, from left to right, of *Au. afarensis* (AL 288-1), *Au. africanus* (Sts 14), *Au. sediba* (MH1), and *H. erectus* (KNM-WT 15000). The specimens are oriented so that the iliac blades all lie in the plane of the photograph (which thus leads to differences between specimens in the orientation of the acetabula and ischial tuberosities). MH1 possesses derived, *Homo*-like morphology compared to other australopithecines, including a relative reduction in the weight transfer distance from the sacroiliac (yellow) to hip (circle)

joints; expansion of the retroauricular surface of the ilium (blue arrows) (determined by striking a line from the center of the sphere representing the femoral head to the most distant point on the posterior ilium; the superior arrow marks the terminus of this line, and the inferior arrow marks the intersection of this line with the most anterior point on the auricular face); narrowing of the tuberoacetabular sulcus (delimited by yellow arrows); and pronouncement of the acetabulocrystal (green arrows) and acetabulosacral buttresses.

(table S2 and fig. S5). The calcaneus is markedly primitive in its overall morphology: the bone is strongly angled along the proximodistal axis, with the point of maximum inflexion occurring at an enlarged peroneal trochlea; the lateral plantar tubercle is lacking; the calcaneal axis is set about 45° to the transverse plane; and the calcaneocuboid facet is vertically set and lacks an expanded posterior projection for the beak of the cuboid (23).

Discussion. The age and overall morphology of *Au. sediba* imply that it is most likely descended from *Au. africanus*, and appears more derived toward *Homo* than do *Au. afarensis*, *Au. garhi*, and *Au. africanus*. Elsewhere in South Africa, the Sterkfontein cranium Stw 53, dated to 2.0 to 1.5 Ma, is generally considered to represent either *H. habilis* (10, 24, 25) or perhaps an undiagnosed form of early *Homo* (26). It played an important role in the assignment of OH 62 to *H. habilis* (27). However, the derived craniodental morphology of *Au. sediba* casts doubt on the attribution of Stw 53 to early *Homo* [see also (28)]: Stw 53 appears to be more primitive than MH1 in retaining closely spaced temporal lines; marked postorbital constriction; a weakly developed supraorbital torus; narrow, nonprojecting nasal bones; anterior pillars; marked nasoalveolar prognathism; medial and lateral expansion of the frontal process of the zygomatic bone; and laterally flared zygomatics. If Stw 53 instead represents *Au. africanus*, the assignment of OH 62 to *H. habilis* becomes tenuous. Attribution of the partial skeleton KNM-ER 3735 to *H. habilis* was tentatively based, in part, on a favorable comparison with OH 62 and on the hypothesis that there were no other contemporaneous non-

robust australopith species to which it could be assigned in East Africa (29). As a result, the interpretation of KNM-ER 3735 as *H. habilis* also becomes uncertain.

The phylogenetic significance of the co-occurrence of derived postcranial features in *Au. sediba*, *H. erectus*, and a sample of isolated fossils generally referred to *Homo* sp. indet. (table S2) is not clear: The latter might represent early *H. erectus*, it might sample the postcranium of *H. rudolfensis* (which would then imply an evolutionary pathway from *Au. sediba* to *H. rudolfensis* to *H. erectus*), or it might represent the postcranium of *H. habilis* [which would suggest that OH 62 and KNM-ER 3735 (two specimens with ostensibly more primitive postcranial skeletons) do not belong in this taxon]. If the latter possibility holds, it could suggest a phylogenetic sequence from *Au. sediba* to *H. habilis* to *H. erectus*. Conversely, although the overall postcranial morphology of *Au. sediba* is similar to that of other australopiths, a number of derived features of the os coxa align the Malapa hominins with later *Homo* (*H. erectus*) to the exclusion of other australopiths. Additionally, *Au. sediba* shares a small number of cranial traits with *H. erectus* that are not exhibited in the *H. habilis*–*H. rudolfensis* hypodigm, including slight postorbital constriction and convexity of the infraorbital region (18). Following on this, MH1 compares favorably with SK 847 (*H. erectus*) in the development of the supraorbital torus, nasal bones, infraorbital region, frontal process of the zygomatic, and subnasal projection. However, MH1 differs from SK 847 in its relatively smaller size, the robust glabellar region, the weakly developed supratoral sulcus, the steeply inclined zygomaticoalveolar crests with a

high masseter origin, and the moderate canine juga, all features aligning MH1 with *Australopithecus*. It is thus not possible to establish the precise phylogenetic position of *Au. sediba* in relation to the various species assigned to early *Homo*. We can conclude that combined craniodental and postcranial evidence demonstrates that this new species shares more derived features with early *Homo* than does any other known australopith species (Table 1 and table S2) and thus represents a candidate ancestor for the genus, or a sister group to a close ancestor that persisted for some time after the first appearance of *Homo*.

The discovery of a <1.95-million-year-old (16) australopith that is potentially ancestral to *Homo* is seemingly at odds with the recovery of older fossils attributed to the latter genus (5) or of approximately contemporaneous fossils attributable to *H. erectus* (6, 30). However, it is unlikely that Malapa represents either the earliest or the latest temporal appearance of *Au. sediba*, nor does it encompass the geographical expanse that the species once occupied. We hypothesize that *Au. sediba* was derived via cladogenesis from *Au. africanus* (≈3.0 to 2.4 Ma), a taxon whose first and last appearance dates are also uncertain (31). The possibility that *Au. sediba* split from *Au. africanus* before the earliest appearance of *Homo* cannot be discounted.

Although the skull and skeleton of *Au. sediba* do evince derived features shared with early *Homo*, the overall body plan is that of a hominin at an australopith adaptive grade. This supports the argument, based on endocranial volume and craniodental morphology, that this species is most parsimoniously attributed to the genus *Australopithecus*. The Malapa specimens dem-

onstrate that the evolutionary transition from a small-bodied and perhaps more arboreal-adapted hominin (such as *Au. africanus*) to a larger-bodied, possibly full-striding terrestrial biped (such as *H. erectus*) occurred in a mosaic fashion. Changes in functionally important aspects of pelvic morphology, including a reduction of the sacroacetabular weight-bearing load arm and enhanced acetabulosacral buttressing (reflecting enhancement of the hip extensor mechanism), enlargement of the iliofemoral ligament attachment (reflecting a shift in position of the line of transfer of weight to behind the center of rotation of the hip joint), enlargement of the acetabulocrystal buttress (denoting enhancement of an alternating pelvic tilt mechanism), and reduction of the distance from the acetabulum to the ischial tuberosity (reflecting a reduction in the moment arm of the hamstring muscles) (20, 32) occurred within the context of an otherwise australopith body plan, and seemingly before an increase in hominin encephalization [in contrast to the argument in (33)]. Relative humeral and femoral diaphyseal strength measures (table S2) also suggest that habitual locomotor patterns in *Au. sediba* involved a more modern human-like mechanical load-sharing than that seen in the *H. habilis* specimen OH 62 (34, 35). Mosaic evolutionary changes are mirrored in craniodental morphology, because the increasingly wide spacing of the temporal lines and reduction in post-orbital constriction that characterize *Homo* first appeared in an australopith and before significant cranial expansion. Moreover, dental reduction, particularly in the postcanine dentition, preceded the cuspal rearrangement (wide spacing of postcanine tooth cusps) that marks early *Homo*.

The pattern of dental eruption and epiphyseal fusion exhibited by MH1 indicates that its age at death was 12 to 13 years by human standards, whereas in MH2 the advanced degree of occlusal attrition and epiphyseal closure indicates that it had reached full adulthood (SOM text S1). Although juvenile, MH1 exhibits pronounced development of the supraorbital region and canine juga, eversion of the gonial angle of the mandible, and large rugose muscle scars in the skeleton, all indicating that this was a male individual. And, although fully adult, the mandible and skeleton of MH2 are smaller than in MH1, which, combined with the less rugose muscle scars and the shape of the pubic body of the os coxa, suggests that MH2 was a female. In terms of dental dimensions, MH1 has mandibular molar occlusal surface areas that are 10.7% (M_1) and 8.1% (M_2) larger than those of MH2. Dimorphism in the postcranial skeleton likewise is not great, though the juvenile status of MH1 tends to confound efforts to assess adult body size. The diameter of the proximal epiphysis for the femoral head of MH1 (29.8 mm) is approximately 9.1% smaller than the superoinferior diameter of MH2's femoral head (32.7 mm). It is likely that MH1 would have experienced some appositional increase in joint size before maturity, thus this disparity would probably have de-

creased somewhat. The distal humeral epiphysis of MH1 is fully fused and its articular breadth (35.3 mm) is only marginally larger than that of MH2 (35.2 mm). Thus, although the dentition and postcranial skeleton are at odds in the degree of apparent size differences, the overall level of dimorphism, if these sex attributions are correct, appears slight in the Malapa hominins and was probably similar to that evinced by modern humans.

References and Notes

- R. A. Dart, *Nature* **115**, 195 (1925).
- D. C. Johanson, T. D. White, *Science* **203**, 321 (1979).
- B. Asfaw *et al.*, *Science* **284**, 629 (1999).
- M. G. Leakey *et al.*, *Nature* **410**, 433 (2001).
- W. H. Kimbel, D. C. Johanson, Y. Rak, *Am. J. Phys. Anthropol.* **103**, 235 (1997).
- B. Wood, *Koobi Fora Research Project, Volume 4: Hominid Cranial Remains* (Clarendon Press, Oxford, 1991).
- G. P. Rightmire, *Am. J. Phys. Anthropol.* **90**, 1 (1993).
- R. J. Blumenshine *et al.*, *Science* **299**, 1217 (2003).
- B. Wood, M. Collard, *Science* **284**, 65 (1999).
- P. V. Tobias, *Olduvai Gorge Volume 4: The Skulls, Endocasts and Teeth of Homo habilis* (Cambridge Univ. Press, Cambridge, 1991).
- D. S. Strait, F. E. Grine, *J. Hum. Evol.* **47**, 399 (2004).
- D. E. Lieberman, *Nature* **410**, 419 (2001).
- The *H. erectus* hypodigm includes African specimens that are referred to the taxon *H. ergaster* by some. Unless otherwise stated, we collectively refer to *H. habilis*, *H. rudolfensis*, *H. erectus*, and *H. ergaster* materials as "early *Homo*."
- F. Spoor *et al.*, *Nature* **448**, 688 (2007).
- P. V. Tobias, *The Brain in Hominid Evolution* (Columbia Univ. Press, New York, 1971).
- P. H. G. M. Dirks *et al.*, *Science* **328**, 205 (2010).
- D. M. Bramble, D. E. Lieberman, *Nature* **432**, 345 (2004).
- Rak (36) describes a feature in the infraorbital region of *Au. boisei* that he refers to as a nasomaxillary basin: a concave depression that is surrounded by a more elevated topography. We see a similar concavity in the infraorbital region of specimens of *H. habilis*–*H. rudolfensis* (KNM-ER 1470, KNM-ER 1805, KNM-ER 1813, and OH 24), although it is not clear whether they represent homologous structures. In specimens of *Au. africanus*, *Au. sediba*, and *H. erectus*, we recognize a slight convexity in this area.
- Some humeri that are probably best attributed to *Australopithecus* lack marked development of the trochlear/capitular keel [or "lateral crest": see (37)], and thus the absence of a marked crest does not reliably differentiate *Australopithecus* from *Homo*. However, although some specimens of early *Homo* (such as KNM-WT 15000) have crests that are more strongly developed than those of modern humans, none exhibit the marked crests of the australopiths. Thus, the marked crest seen in the Malapa humeri can be seen to be shared with *Australopithecus* rather than *Homo*.
- M. D. Rose, *Am. J. Phys. Anthropol.* **63**, 371 (1984).
- A. Walker, C. B. Ruff, in *The Nariokotome Homo erectus Skeleton*, A. Walker, R. E. F. Leakey, Eds. (Harvard Univ. Press, Cambridge, MA, 1993), pp. 221–233.
- C. K. Brain, E. S. Vrba, J. T. Robinson, *Ann. Transv. Mus.* **29**, 55 (1974).
- L. C. Aiello, C. Dean, *An Introduction to Human Evolutionary Anatomy* (Academic Press, London, 1990).
- A. R. Hughes, P. V. Tobias, *Nature* **265**, 310 (1977).
- D. Curnoe, P. V. Tobias, *J. Hum. Evol.* **50**, 36 (2006).

- F. E. Grine, W. L. Jungers, J. Schultz, *J. Hum. Evol.* **30**, 189 (1996).
- D. C. Johanson *et al.*, *Nature* **327**, 205 (1987).
- R. J. Clarke, *S. Afr. J. Sci.* **104**, 443 (2008).
- R. E. F. Leakey, A. Walker, C. V. Ward, H. M. Grausz, in *Hominidae*, G. Giacobini, Ed. (Jaca Books, Milano, Italy, 1989), pp. 167–173.
- L. Gabunia, A. Vekua, *Nature* **373**, 509 (1995).
- T. D. White, in *Paleoclimate and Evolution with Emphasis on Human Origins*, E. S. Vrba, G. H. Denton, T. C. Partridge, L. H. Burckle, Eds. (Yale Univ. Press, New Haven, CT, 1995), pp. 369–384.
- J. T. Stern Jr., R. L. Susman, *Am. J. Phys. Anthropol.* **60**, 279 (1983).
- C. O. Lovejoy, *Gait Posture* **21**, 113 (2005).
- C. Ruff, *Am. J. Phys. Anthropol.* **138**, 90 (2009).
- It is possible that the more *Homo*-like humeral-to-femoral diaphyseal strength ratios in *Au. sediba* reflect a relative reinforcement of the femoral diaphysis in the context of femoral elongation (resulting in longer bending-moment arms) without a change in locomotor behavior. At present, we are unable to directly assess the absolute and relative length of the femur in *Au. sediba*.
- Y. Rak, *The Australopithecine Face* (Academic Press, New York, 1983).
- M. R. Lague, W. L. Jungers, *Am. J. Phys. Anthropol.* **101**, 401 (1996).
- R. R. Skelton, H. M. McHenry, *J. Hum. Evol.* **23**, 309 (1992).
- M. Collard, B. Wood, *Proc. Natl. Acad. Sci. U.S.A.* **97**, 5003 (2000).
- H. F. Smith, F. E. Grine, *J. Hum. Evol.* **54**, 684 (2008).
- We thank the South African Heritage Resources Agency for the permits to work at the Malapa site; the Nash family for granting access to the Malapa site and continued support of research on their reserve; the South African Department of Science and Technology, the South African National Research Foundation, the Institute for Human Evolution, the Palaeontological Scientific Trust, the Andrew W. Mellon Foundation, the AfricaArray Program, the U.S. Diplomatic Mission to South Africa, and Sir Richard Branson for funding; the University of the Witwatersrand's Schools of Geosciences and Anatomical Sciences and the Bernard Price Institute for Palaeontology for support and facilities; the Gauteng Government, Gauteng Department of Agriculture, Conservation and Environment and the Cradle of Humankind Management Authority; E. Mbua, P. Kiura, V. Iminjili, and the National Museums of Kenya for access to comparative specimens; Optech and Optron; Duke University; the Ray A. Rothrock Fellowship of Texas A&M University; and the University of Zurich 2009 Field School. Numerous individuals have been involved in the ongoing preparation and excavation of these fossils, including C. Dube, B. Eloff, C. Kemp, M. Kgasi, M. Languza, J. Malaza, G. Mokoma, P. Mukanela, T. Nemvundi, M. Ngcamphalala, S. Jirah, S. Tshabalala, and C. Yates. Other individuals who have given significant support to this project include B. de Klerk, C. Steininger, B. Kuhn, L. Pollarolo, B. Zipfel, J. Kretzen, D. Conforti, J. McCaffery, C. Dlamini, H. Visser, R. McCrae-Samuel, B. Nkosi, B. Louw, L. Backwell, F. Thackeray, and M. Peltier. T. Stidham helped construct the cladogram in fig. S3. J. Smilg facilitated computed tomography scanning of the specimens. R. Clarke and F. Kirera provided valuable discussions on these and other hominin fossils in Africa.

Supporting Online Material

www.sciencemag.org/cgi/content/full/328/5975/195/DC1
SOM Text 1 to 4
Figs. S1 to S5
Tables S1 and S2
References

19 November 2009; accepted 26 February 2010
10.1126/science.1184944

ERRATUM

Post date 17 December 2010

Research Articles: "*Australopithecus sediba*: A new species of *Homo*-like Australopith from South Africa" by L. R. Berger *et al.* (9 April, p. 195). In the legend of Fig. 3, the mesiodistal diameter of the RM2 of the mandible of the adult individual MH2 should be 13.1 mm (not 14.1 mm). In Fig. 4, the specimen number of the pelvis of *Australopithecus afarensis* (Lucy) should be A.L. 288-1 (not A.L. 228-1). These errors do not affect the Research Article's conclusions.



Supporting Online Material for

***Australopithecus sediba*: A New Species of *Homo*-like Australopith from South Africa**

Lee R. Berger,* Darryl J. de Ruiter, Steven E. Churchill, Peter Schmid, Kristian J. Carlson, Paul H. G. M. Dirks, Job M. Kibii

*To whom correspondence should be addressed. E-mail: profleeberger@yahoo.com

Published 9 April 2010, *Science* **328**, 195 (2009)
DOI: 10.1126/science.1184944

This PDF file includes

Materials and Methods
SOM Text S1 to S4
Figs. S1 to S5
Tables S1 and S2
References

TEXT S1. Fossil preservation, ontogenetic age, and sex of Malapa hominins

Recent discoveries at the site of Malapa include associated craniodental and postcranial remains of at least two individuals. The two skeletons were found in the same stratigraphic horizon, dated to between 1.95-1.78 Ma, and separated from one another by no more than half a meter horizontally. The remains of one individual (MH2) were recovered in partial articulation, while those of the other (MH1) were somewhat more disturbed, yet still in close association (distributed over an area of less than 2 m²). The majority of the hominin fossils are in very good condition, and this, combined with the spatial distribution of the skeletons, the partial articulation of one individual (and of some of the associated faunal remains), and the geological context indicates rapid deposition and contemporaneity of the two hominin individuals (1).

MH1 is a partial skeleton preserving much of the cranium and a partial mandible, maxillary and mandibular teeth, and portions of the postcranial axial skeleton, pectoral girdle, upper limb, pelvic girdle, and lower limb (Table S1). The first element of MH1 found (UW 88-1, clavicle) was discovered by Matthew Berger on August 15, 2008. Secondary growth centers of the proximal humerus, humeral medial epicondyle, proximal ulna, distal radius, os coxa and proximal femur were unfused at the time of death, while that of the distal humeral epiphysis was fused. Mandibular and maxillary permanent canines, M1s and M2s and the right I¹ exhibit slight to moderate occlusal attrition. Radiographic examination and virtual preparation demonstrates that the maxillary and mandibular M3 crowns are nearing completion, but lacking root development. The state of postcranial epiphyseal fusion and the degree of development of the M3 crowns leads to the provisional conclusion that MH1 was at a developmental stage equivalent to a modern human child of 12 -13 years (2), making this specimen roughly comparable in physiological age to the type specimen of *H. habilis* (OH 7: (3)) and the *H. erectus* (*ergaster*) individual from Nariokotome (KNM-WT 15000: (4)). Pronouncement of the supraorbital torus and glabellar prominence, eversion of the gonial region of the mandible, pronouncement of the canine jugae, and relatively large and rugose muscle scars in the postcranial skeleton (despite the juvenile status of the individual) all support the suggestion that MH1 was a male. The sciatic notch of MH1 is fairly wide (stage 2 of Walker (5)), but this character state is plesiomorphic for the genus *Homo* (6) and also is commonly seen in modern human juvenile males (5). Thus, a fairly wide sciatic notch is not inconsistent with the diagnosis of a male individual.

MH2 is represented by an incomplete mandible, maxillary and mandibular teeth, and portions of the postcranial axial skeleton, pectoral girdle, upper limb, pelvic girdle, and lower limb (Table S1). The first element of MH2 (UW 88-57, humerus) was found by Lee Berger on September 4, 2008. Adult status for MH2 is indicated by full ossification, with obliterated fusions lines, of all observable epiphyseal plates, and by moderate-to-heavy wear of the maxillary and mandibular molars, including the M3s. The mandibular ramus is small in height relative to that of MH1, and the preserved but damaged gonial region evinces less eversion (the gonial region in MH2 is damaged, and owing to displacement of its inferior border it appears to exhibit slight-to-moderate eversion; however, we judge that reconstruction of the MH2 mandible would greatly reduce or even eliminate this apparent eversion). While the ramus of MH2 is slightly anteroposteriorly broader than that of MH1, the juvenile has not completed ramal growth. Despite this, the MH1 ramus at its present ontogenetic stage is already taller than the adult morphology exhibited by MH2, while both corpora are approximately equal in robusticity (Fig. S2). The pubic body of the os coxa is mediolaterally broad and square in shape, and the

postcranial muscle scars are generally weakly-to-moderately rugose, all suggesting that MH2 was a female.

TEXT S2. Comparative craniodental materials examined in this study.

Au. afarensis. The samples attributed to *Au. afarensis* from Hadar, Laetoli, and the Middle Awash were utilized. For this taxon we relied on published reports (7) and casts.

Au. africanus. The samples attributed to *Au. africanus* from Taung, Sterkfontein and Makapansgat were employed. Original specimens were examined first-hand.

Au. garhi. The cranium BOU-VP-12/130 from Bouri was included, with data taken from a published report (8).

Au. aethiopicus. The cranium KNM-WT 17000 was examined first-hand for this study.

Au. boisei. Samples from the Omo Shungura sequence, East Lake Turkana, and Olduvai Gorge were included in this study. Original specimens from East Lake Turkana were examined first-hand, while casts and published reports (9) were used to study the Omo and Olduvai materials.

Au. robustus. The samples from Kromdraai, Swartkrans, Sterkfontein, Drimolen, Gondolin, and Coopers were included in this study. First-hand observations of original specimens from all localities were used with the exception of Drimolen fossils, which were compared using published reports (10, 11).

H. habilis. Samples from Olduvai Gorge, East Lake Turkana, the Omo Shungura sequence, and Hadar were included in this study. Original East Lake Turkana fossils were examined first-hand, while for the Olduvai, Omo, and Hadar materials we relied on casts and published reports (12, 13, 14). We include the following fossils in the hypodigm of *H. habilis*: AL 666-1, KNM-ER 1478, KNM-ER 1501, KNM-ER 1502, KNM-ER 1805, KNM-ER 1813, KNM-ER 3735, OH 4, OH 6, OH 7, OH 13, OH 15, OH 16, OH 21, OH 24, OH 27, OH 31, OH 37, OH 39, OH 42, OH 44, OH 45, OH 62, and OMO-L894-1.

H. rudolfensis. Samples from Olduvai Gorge, East Lake Turkana, and Lake Malawi were included in this study. The East Lake Turkana fossils were examined first-hand, while for the Olduvai and Lake Malawi fossils we relied on casts and published reports (15, 16). We include the following fossils in the hypodigm of *H. rudolfensis*: KNM-ER 819, KNM-ER 1470, KNM-ER 1482, KNM-ER 1483, KNM-ER 1590, KNM-ER 1801, KNM-ER 1802, KNM-ER 3732, KNM-ER 3891, OH 65, and UR 501.

H. erectus. Samples from Baringo, Chemeron, Dmanisi, East and West Lake Turkana, Konso, Olduvai Gorge, Sangiran, Swartkrans, Tighenif, Trinil, and Zhoukoudian were included in this study. In particular, the following specimens from Swartkrans are considered to represent *Homo erectus*: SK 15, SK 18a, SK 27, SK 43, SK 45, SK 68, SK 847, SK 878, SK 2635, SKW 3114, SKX 257/258, SKX 267/2671, SKX 268, SKX 269, SKX 334, SKX 339, SKX 610, SKX 1756, SKX 2354, SKX 2355, SKX 2356, and SKX 21204. It has been suggested (17, 18) that SK 847 and Stw 53 might represent the same taxon, and that this taxon is a currently undiagnosed species of *Homo* in South Africa. However, we agree with Clarke (19, 20) that SK 847 can be attributed to *H. erectus*, and that Stw 53 represents *A. africanus*. Since there is no clear indication that more than one species of *Homo* is represented in the Swartkrans sample, we consider all this material to belong to *H. erectus*. Original Baringo, Chemeron, Lake Turkana and Swartkrans fossils were all examined first-hand, while the remainder were based on casts and published reports (21, 22, 23, 24, 25).

TEXT S3. Character states based on measures from Table 2

Here we describe the character states displayed in Table 1 that are based on measurements presented in Table 2.

1. Cranial capacity: <600=small; 600-700=intermediate; >700=large
5. Postorbital constriction index: >80=slight; 71-79=moderate; <70=marked
6. Horizontal distance between the TMJ and M²/M³: <58=short; >58=long. MH1 does not have the M³ erupted, thus additional growth would almost certainly influence this measure; however, we judge that such growth would not exceed the 58mm cutoff length required to necessitate a designation of long.
7. Facial prognathism: <65=prognathic; 65-70=mesognathic; >70=orthognathic. For this measure we use the sellion-prosthion angle since the M³ of MH1 is not yet erupted. We note that additional growth in MH1 might have altered this angle.
9. Anteromedial (A-M) incursion of temporal lines on frontal bone based on minimum frontal breadth (ft-ft): >60=weak; 40-60=moderate; <40=strong
25. Inferior nasal bridge breadth: <10=narrow; >10=wide
31. Malar thickness: <15=thin; >15=thick
32. Infraorbital foramen height relative to the inferior orbital margin: >20=low; <20=high
35. Masseter origin index: <100=low; >100=high
38. Subnasal projection index: <100=weak; 100-150=moderate; >150=marked
50. Mandibular corpus cross sectional area at M₁: <700=small; >700=large
57. Maxillary post-canine crown area: <700=small; 700-800=moderate; >800=large
59. Mandibular molar crown area: <500=small; 500-600=moderate; >600=large
60. Maxillary incisor to post-canine ratio: <12=small; 12-20=moderate; >20=large
61. Maxillary canine to post-canine ratio: <10=small; >10=large
62. Mandibular canine to post-canine ratio: <10=small; >10=large

TEXT S4. Digital reconstruction and virtual preparation

Virtual preparation of specimens was undertaken when mechanical preparation was no longer feasible (e.g., [Figs. S1 and S5](#)). The protocol for virtual preparation of a volume is briefly described. Through the use of computed tomography (CT), serial stacks of images representing entire fossils were acquired (e.g., 500 images for MH1 cranium). CT scanning was performed at Johannesburg Hospital (Johannesburg, South Africa) on a Philips Brilliance 16P medical CT scanner (Philips Healthcare, Andover, MA). Bone reconstruction algorithms were applied to raw scan data in order to produce image stacks (DICOM format) that could be used in subsequent analyses. Pixel dimensions in images ranged between 0.23 – 0.47 mm, depending on object size, while scan slice thickness was always 0.8 mm, and reconstruction increment always 0.4 mm (i.e., space between images). An attempt was made to use isotropic voxels (e.g., 0.4 mm), whenever specimen size made it feasible.

Following data acquisition, image stacks were segmented to produce isosurfaces using Avizo 6.1 software (Visualization Sciences Group, Mérignac, France). During the creation of an isosurface, threshold choices were verified using external dimensions of exposed morphology on specimens in order to corroborate equivalent dimensions of morphology on rendered specimens. Minor variations in threshold choice had very little effect on these dimensions. When possible, automated segmentation routines were used to render volumes. When automated routines were not feasible, for example when specimen and matrix densities were too similar, rendering was performed by manual segmentation. In the latter case, image stacks were assessed in three orthogonal directions, one of which was determined by the orientation of the original scan plane. The decision to include an individual voxel within a rendered volume was finalized after consulting each of the three orthogonal views, as well as voxels in the same line of sight through the preceding and following images of the stack. When more extensive preparation was required (e.g., the cranium of MH1, see [Fig. S1](#)), this process was repeated a second time.

In order to estimate cranial capacity on the rendered cranium of MH1, the left parietal and portions of the articulating left temporal squama were duplicated and mirror-imaged to fill-in missing morphology on the right side of the cranium. The mirror-imaged bones were aligned by including areas of overlap between existing frontal and temporal bones on the right side and mirror-imaged areas from the left side. In this way, curvatures could be aligned and the shape of the cranial vault estimated. We recognize that this approach reduces bilateral asymmetry in vault shape, but we note that the area of overlap was minimized to the extent possible and we balanced this criterion with the importance of aligning the mirror-imaged areas.

The cranial vault reconstruction is missing only the occipital, petrous portions of both temporal bones, and small areas of the parietal bones along the length of the sagittal suture. The endocranial surface of the reconstructed vault, including the duplicated and mirror-imaged portion on the right side of the cranial vault, was isolated and rendered. The volume of the rendered partial endocast is 363 cc. There are two regions that must be added to the partial endocast volume in order to complete it, both of which must be estimated: a small posteriorly-located area containing much of the occipital lobes, and specifically the occipital poles, and the posterior cranial fossa. The missing portion at the posterior aspect of the cranium is estimated to be approximately 7-10 cc. This estimate is based on comparable volumes that were removed or added to the endocast during early stages of its virtual reconstruction. Estimating size of the missing posterior cranial fossa is less straightforward. Two australopith (AL 23000 and STS 19) cerebellar volumes are reported as 40-50 cc, while three early members of the genus *Homo*

(KNM-ER 1813, KNM-ER 1805, and KNM-ER 1470) have cerebellar volumes approximately ranging between 55-75 cc (26). A conservative estimate of 50 cc for the posterior cranial fossa of the MH1 juvenile, therefore, seems justified. This is the basis for the minimum estimated cranial capacity of 420 cc (363 cc + 7 cc + 50 cc).

Humeral and femoral specimens of MH1 and MH2 were CT scanned and rendered using the same procedure as outlined above. In order to create diaphyseal cross sections, humeral and femoral medullary spaces were identified and matrix was subtracted following the same manual segmentation procedure as outlined above. Subsequently, humeral regions of interest (e.g., midshaft and mid-proximal diaphysis) were identified on virtual specimens, cross sections obtained, and cross-sectional geometric properties calculated following an established protocol (27, 28, 29). Femoral regions of interest (e.g., mid-proximal diaphyses) were identified on virtual specimens using a chimpanzee femur in order to estimate approximate location along the diaphysis of MH1. This was accomplished by overlapping the MH1 specimen onto the proximal region of a chimpanzee femur, then orientating the MH1 reconstructed proximal femur following established criteria (27, 28, 29). A chimpanzee femur was selected because of a greater assumed similarity with MH1 in overall length than comparative human femora. If absolute femur length of MH1 ultimately resembles modern human length more than chimpanzee length, then the percent length of the femoral cross section of interest would increase (e.g., 75% rather than 70%, etc.). Once positioned correctly, cross sections of the diaphysis were obtained, and cross-sectional geometric properties were calculated following the established protocol (27, 28, 29).

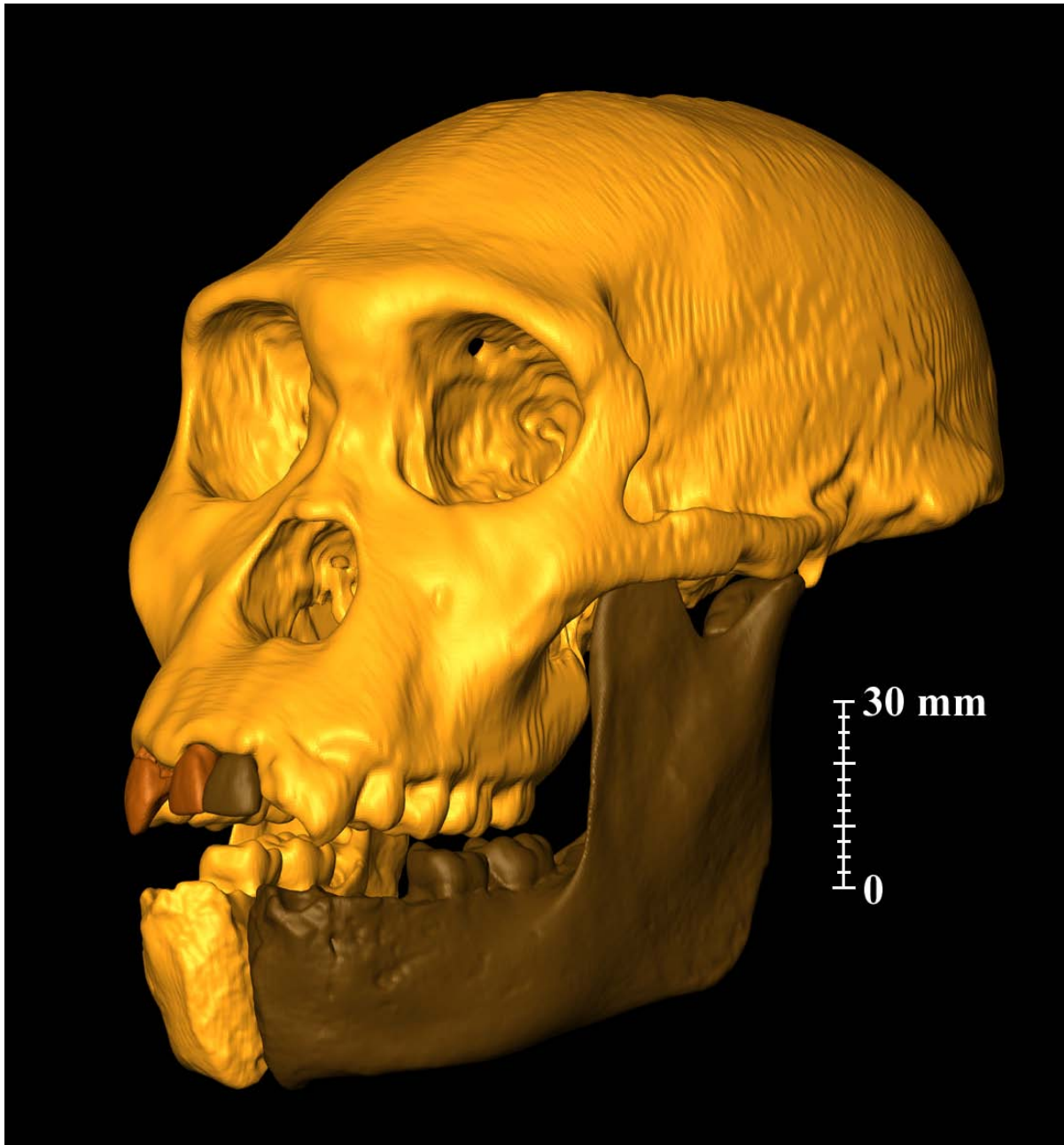


[Figure S1](#). Virtual reconstruction of the skull of MH1. Orange signifies intact portions of the cranium and mandible that were manually segmented from the surrounding matrix. Copper-colored teeth signify isolated teeth that were virtually refit to the rendered cranium. Brown signifies mirror-imaged antimeres. See [Text S4](#) for details of the virtual reconstruction process.

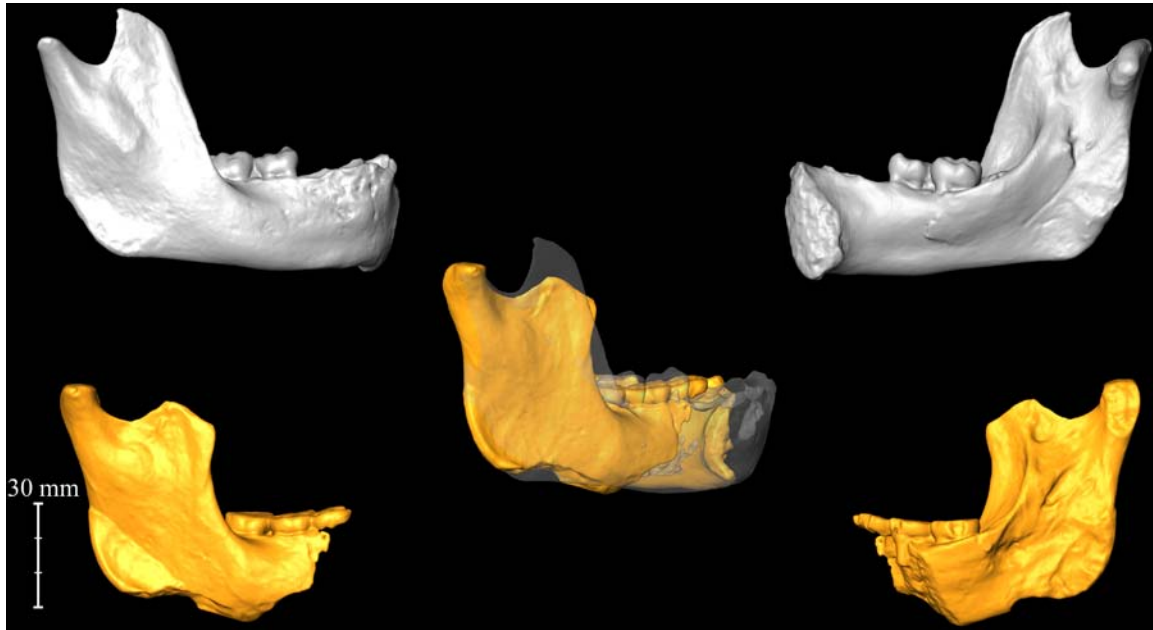


Figure S2. Virtual reconstructions of the mandible of MH1 (grey) in (a) lateral and (b) medial views, and MH2 (orange) in (c) lateral and (d) medial views. We overlap the specimens (e), aligning them at the condyle. Note that although the ramus of the adult female MH2 is anteroposteriorly broader, the ramus of the juvenile male MH1 (transparent) is already taller, indicating some degree of sexual dimorphism.

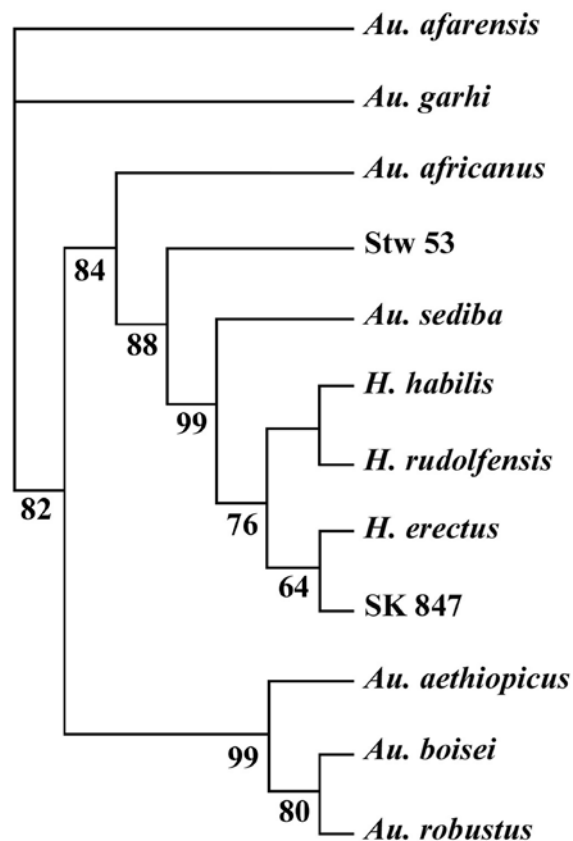


Figure S3. Most parsimonious cladogram produced from the characters presented in Table 1, using PAUP 4.0 (beta version 10). Tree length is 128 steps if character states are unordered and multistate characters are treated as either uncertainties or as variable; tree length is 137 steps if character states are ordered and multistate characters are treated as either uncertainties or as variable; tree length is 165 if character states are unordered and multistate characters are treated as polymorphisms, and 175 steps if character states are ordered and multistate characters are treated as polymorphisms. When run with unordered character states, only one tree results; when run with ordered character states, two trees result: the one presented here, and another where KNM-ER 1470 resides with the *H. erectus*/SK 847 clade. The consistency index is 0.672, the homoplasy index is 0.328, and the retention index is 0.744. Bootstrap numbers are based on 10000 replicates. The inclusion of postcranial character states in the phylogenetic analysis would necessitate the exclusion of *H. rudolfensis* from the analysis. Also, the postcranial features that *Au. sediba* shares with *Homo* are found primarily in the os coxa, an element that is completely unrepresented in *H. habilis*. Taxonomic diagnoses and phylogenetic interpretations are generally based on craniodental remains, which necessitate such a focus even in taxa such as *Au. sediba* that preserve a more complete representation of the skeleton. This is not to say, however, that postcranial attributes cannot enlighten phylogenetic studies, and for these reasons the significance of the postcranial morphology of Malapa is discussed. What is important is that the postcranial remains support phylogenetic inferences derived from study of the craniodental material.

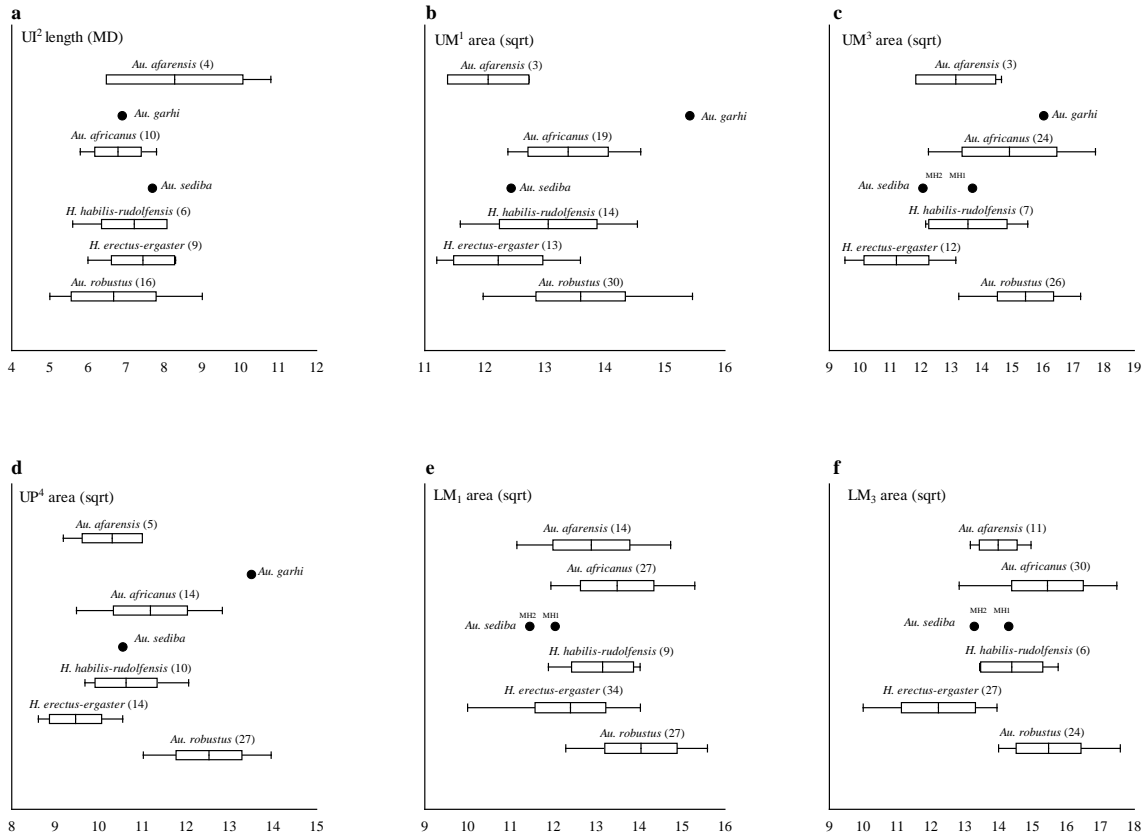


Figure S4. Dental size of *Au. sediba* compared to other early hominin taxa. These are additional teeth preserved in MH1 and MH2 that were not included in Fig. 3 in the main text. Owing to small sample sizes, *H. habilis* and *H. rudolfensis* samples were combined. (a) Upper lateral incisor MD length; (b) Square root of calculated (MD x BL) upper first molar area; (c) Square root of calculated (MD x BL) upper third molar area; (d) Square root of calculated (MD x BL) upper fourth premolar area; (e) Square root of calculated (MD x BL) lower first molar area; (f) Square root of calculated (MD X BL) lower third molar area. Measures taken on original specimens by DJD for *Au. africanus*, *Au. robustus*, and *Au. sediba*. Measurements for *Au. afarensis*, *H. habilis*, *H. rudolfensis*, and *H. erectus* from (30).

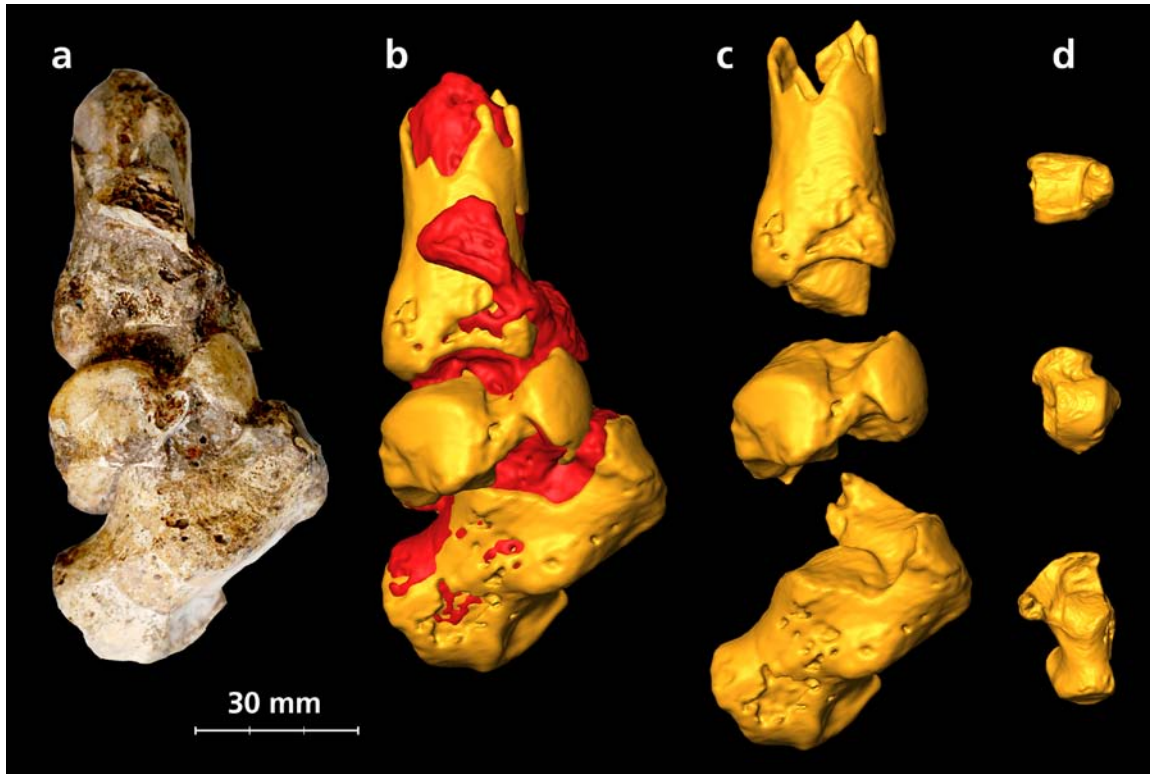


Figure S5. Right distal tibia, talus and calcaneus of MH2, illustrating the virtual separation of elements undertaken to allow for measurement of the talus as reported in SOM Table S2: (a) partial leg and foot skeleton as preserved, showing tibia, talus and calcaneus in near-anatomical relationship and cemented together with calcified sediment; (b) virtual reconstruction of the partial leg and foot skeleton, with areas of calcified sediments indicated in red; (c) distal tibia (top), talus (middle) and calcaneus (bottom) after virtual removal of calcified sediment and separation of the elements; (d) virtual reconstructions of tibia in inferior view (top) and talus (middle) and calcaneus (bottom) in superior view, all at 50% of size of elements depicted in the other three columns.

Table S1: List of elements currently attributed to MH1 and MH2^a

Element	Catalog number UW88 ^b
Malapa Hominin 1 (MH1)	
Cranium with RP ³ -M ³ , LI ² and LP ³ -M ³	50
Cranial vault fragments (2)	31, 32
Right I ¹	29
Right C ¹	30
Right hemi-mandible with erupted RM ₁ , RM ₂ and unerupted RM ₃ crown	8
LC ₁ with anterolateral wall of mandibular corpus	2
Cervical vertebrae (3)	9, 72, 83
Thoracic vertebrae (3)	11, 37, 69
Thoracic vertebral fragments (2)	70, 90
Rib fragments (6)	13, 15, 17, 41, 74, 86
Lumbar vertebra (1)	92
Acromial end and lateral shaft of right clavicle	1
Scapular fragment (root of spine)	113
Right humerus (3 conjoined pieces: lacking proximal epiphysis)	34, 42, 88
Left proximal humeral metaphysis/diaphysis	36
Right proximal ulna	3
Distal epiphysis of right radius	12
Right third metacarpal	112
Inferior portion of right ilium (2 conjoined pieces)	6, 7
Left ilium and associated fragments	67, 68, 102
Left ischium	14
Right proximal femur (4 conjoined pieces)	4, 5, 39, 89
Right distal tibia (2 conjoined pieces) ^c	21, 40
Metatarsal diaphyses (2)	16, 22
Malapa Hominin 2 (MH2)	
Partial left M ²	19
Left M ³	20
Partial right mandible with M ₁ -M ₃	54
Partial left mandibular corpus with M ₃ and partial M ₂	55
Cervical vertebra (1)	93
Thoracic vertebrae (3)	43, 44, 96
Right first rib	58
Right rib (complete)	61
Rib fragments (6)	45, 46, 47, 48, 59, 60
Acromial end and lateral shaft of right clavicle	38
Acromial end of left clavicle	94
Right scapula (2 conjoined pieces)	56
Left scapular glenoid fossa	104
Left scapular acromion process	103

Right humerus	57
Left humeral head	101
Right ulna	62
Right radius	85
Left capitate	105
Right hamate	95
Left hamate	106
Right metacarpals I, II, III, IV and V	115, 116, 117, 118, 119
Right manual proximal phalanges (2)	108, 120
Right manual intermediate phalanges (3)	121, 122, 123
Right manual distal phalanx	124
Right pubis	52
Left ischiopubic ramus and partial pubic symphysis	10
Right femoral head and partial neck	51
Right distal femur	63
Right patella (2 conjoined pieces)	79, 100
Right proximal tibia (2 conjoined pieces)	64, 78
Right distal tibia	97
Left proximal tibia fragment	24
Left proximal fibula (2 conjoined pieces)	23, 84
Left distal fibula ^d	76
Right talus	98
Right calcaneus	99
Pedal proximal phalanx ^d	91
Pedal distal phalanx	111

a. While all of the material recovered from Malapa is considered to represent *Au. sediba*, attribution of elements to specific individuals is subject to change.

b. Catalogue numbers assigned for individual sites based on the University of the Witwatersrand collections numbering system (31). Malapa is designated site UW88, therefore all numbers indicated above are preceded by the prefix UW88-.

c. Attribution to MH1 uncertain.

d. Attribution to MH2 uncertain.

Table S2: Phenetic comparisons of postcranial morphology in *Australopithecus* and early *Homo*. The postcranial features described in this table are not intended as an exhaustive list of the morphological attributes of the Malapa hominin postcranial skeletons. Postcranial character states for various taxa were derived from the literature where noted, otherwise data derive from measurements and observations by the authors on the original fossil material, or, in the case of specimens from Hadar and Olduvai Gorge, casts.

	<i>Au. afarensis</i> ^a	<i>Au. africanus</i> ^b	<i>Au. sediba</i>	<i>H. habilis</i> ^c	<i>H. sp. indet.</i> ^d	<i>H. erectus</i> ^e
BODY PROPORTIONS						
Body size (femoral head SI diameter)	Variable (but generally small) (28.6 – 39.4) (32)	Variable (but generally small) (30.8 – 38.4) (33, 34)	Small (29.8 ^f – 32.7)	Small? (35)	Large (38.9 – 42.6)	Variable (but generally large) (33.4 - 46.1) (6, 36-38)
Brachial index	72.8-90.7(39)	-	87.9	79.5-93.2(39)	-	79.9(37)
Relative humeral length (humeral length/femoral head diameter) ^g	Long 9.23	-	Intermediate 7.86 – 8.15	-	-	Short 6.93 – 7.38
Humeral-to-femoral diaphyseal strength (humeral mid-proximal/femoral midshaft polar section modulus)	-	-	0.383 ^h	0.590 ⁱ (40)	-	0.303-0.442 (41)
Upper-to-lower limb joint size proportions (humeral distal articular breadth/femoral head diameter)	Large (1.05)	Large (1.11) ^j	Large (1.08)	-	-	Small (0.88)
CLAVICLE						
Angle of acromial extremity to plane of shaft	-	Anterosuperiorly inflected	Anterosuperiorly inflected	Uninflected	-	Anterosuperiorly inflected
Conoid tubercle	Angular margin(42)	Angular margin	Angular margin	Weak/absent tubercle	-	Weak/absent tubercle
Mid-lateral shaft cross-sectional shape	Dorsoventrally-elongated oval (42)	Dorsoventrally-elongated oval	Dorsoventrally-elongated oval	Rounded	-	Variably dorsoventrally-elongated oval or rounded

SCAPULA

Spine thickness	Moderately thick(43)	Moderately thick	Moderately thick	Thick(43, 44)	-	Moderately thick(43)
Axillary border ventral pillar	Strongly developed	Strongly developed	Strongly developed	-	-	Moderately developed
Axilloglenoid angle	116°	115°(36)	114°	-	-	128°(36)
HUMERUS						
Midshaft (40-50%) xsect %CA	-	63-74	75 ^k	79.7(40)	-	81.7(40)
Humeral torsion	124°	126°	103°	-	-	110° - 126°(36)
Projection of medial epicondyle (medial epicondyle /biepicondylar breadth)	Weak-moderate (0.16 – 0.25)	Moderate (0.25)	Strong (0.31)	Strong(45) (0.29)	-	Strong (0.32) ¹
Lateral epicondyle	Moderately projecting, proximally-positioned	Pronounced, proximally-positioned	Pronounced, proximally-positioned	Pronounced, proximally-positioned	-	Moderately projecting, distally-positioned
Brachioradialis crest	Variable	Marked	Marked	-	-	Weak
Septal aperture (supratrochlear foramen)	Present	Absent	Present	Present(45)	-	Absent
Supracapitular fossa	Moderate	Moderate	Moderate to deep	Well excavated(45)	-	Shallow
Olecranon fossa	Relatively large and deep	Relatively narrow and deep	Relatively large and deep	Relatively large and deep (contra (46))	-	Relatively narrow and shallow
Capitular morphology (Capitular superoinferior breadth/ humeral distal articular breadth)	Superoinferiorly elongated (0.42)	Superoinferiorly elongated (0.43)	Superoinferiorly elongated (0.43-0.44)	Superoinferiorly elongated (0.47)	-	Moderately superoinferiorly elongated (0.40)
Trochlear/capitular keel	Marked	Marked	Marked	Marked(45)	-	Moderate
RADIUS						
Head diameter/neck length	0.38	0.60	(0.50)	0.49	-	-

ULNA						
Orientation of trochlear notch	Anterior (47) to Anteroproximal	Anteroproximal	Anteroproximal	-	-	Anterior
M. flexor carpi ulnaris tubercle	Weak-moderate	Pronounced	Pronounced	-	-	Weak-moderate
Trochlear keel	Mild (47)	Mild	Mild	-	-	Moderate
Orientation of plane of radial notch	Slight proximolateral	Slight proximolateral	Slight proximolateral	-	-	Lateral
M. flexor digitorum superficialis origin	Crest	Crest	Crest	-	-	Tubercle
Supinator crest	Weak	Moderate	Moderate	-	-	Prominent
Mid-proximal diaphyseal shape	Rounded	Laterally-flattened triangle	Laterally-flattened "D"	-	-	Anteriorly-flattened triangle
Interosseous crest	Moderate	Weak	Weak	-	-	Prominent
OS COXA						
Acetabulocrystal buttress	Slight-to-absent	Slight-to-absent	Pronounced ^k	-	Pronounced	Pronounced
Position of crystal tubercle	Anterior	Anterior	(Posterior) ^k	-	Posterior	Posterior
Iliac crest shape	Shallow sigmoid	Shallow sigmoid	(moderate sigmoid) ^k	-	Deep sigmoid	Deep sigmoid
Anterior inferior iliac spine shape	Rectilinear	Rectilinear	Sigmoid ^k	-	Sigmoid	Sigmoid
Posterior fossa for M. gluteus medius	Small	Moderately expanded	Moderately expanded ^k	-	Expanded	Expanded
Posterior iliac height	Short	Intermediate	Tall ^k	-	Tall	Tall
Retroauricular area	Short	Short	Expanded ^k	-	Expanded	Expanded
Tuberoacetabular sulcus	Wide	Wide	Narrow ^k	-	Narrow	Narrow
Relative tuberoacetabular sulcus width (TAS/acetabular width) ^m	0.50(48)	0.52	0.29	-	0.25	-
Relative auricular-acetabular distance (acetabuloauricular distance/femoral head SI diameter) ⁿ	Long (1.68)	Long (1.62)	Intermediate ^k (1.31)	-	Short (1.12-1.15)	Short (1.00)

Acetabulosacral buttress	Moderate	Small	Pronounced ^k	-	Pronounced	Pronounced
Minimum thickness of acetabulosacral buttress(19)	15.5	13.9	18.0	-	20-26(49)	19.2
Retroauricular height (posterior superior iliac spine to junction of the two limbs of the auricular area of posterior border)	(30)	33	≥ 50.5	-	52-53(49)	(47)
Pubic symphyseal face	Short, ovoid(6)	Short(6)	Tall, thin	-	Tall, thin(6)	Tall, thin(6)
FEMUR						
Relative neck length (neck length ^o /femoral head SI diameter)	1.14	0.951-1.442 (34)	1.02 ^k		1.06-1.12	1.26 ^p
Neck-shaft angle	Variably high (117°-125°)(32, 50)	Variably high (118° - 122°)	Low ^k (115°)	High (123°)(35)	Moderate (118°-119°)	Low (110°-115°)
Neck shape index (100* neck AP/SI diameter)	68.7-86.9(51)	73.4(51)	69.4 ^k	-	73.6-79.0	73.7
Neck cross-sectional long axis	Superoinferiorly oriented	Superoinferiorly oriented	Anterosuperior to posteroinferiorly oriented ^k	Superoinferiorly oriented	Moderately anterosuperior to posteroinferiorly oriented	Moderately anterosuperior to posteroinferiorly oriented
Proximal diaphyseal cross-sectional shape	Mediolaterally expanded but not buttressed	Strongly mediolaterally buttressed	Mediolaterally expanded but not buttressed ^k	Approx. circular(10)	Strongly mediolaterally buttressed	Strongly mediolaterally buttressed(10)
Meric index (proximal diaphyseal AP/ML diameter)	66.7 - 71.6(35, 50)	74.1	79.6 ^k	1.00(35)	71.0 - 74.3	74.1
Midshaft-to-mid-proximal (50-65%) xsect %CA	-	(80)	84.4 ^h	83.2(50)	85.6(52)	65.2-86.8(40, 41)
pilaster	Variably present(32, 53)	Well-developed	Absent ^k	Well-developed(40, 43, 54)	Absent	Slight

Linea aspera	Weak(32, 53)	Weak	Weak ^k	Prominent(45)	Prominent	Prominent
TIBIA						
Popliteal (soleal) line	Prominent(32)	Prominent(55)	Moderate? ^k	Strongly marked(56)	Marked?	Marked
Proximal shaft curvature	Slight, convex medially	Absent	Absent ^k	Slight, convex medially(56)	Absent	Absent
Diaphyseal anterior border	Rounded?	-	Sharp ^k	Rounded (56)	Sharp?	Rounded
Midshaft relative muscle attachment size (midshaft)	-	-	Flexor digitorum longus \cong tibialis posterior ^k	Tibialis posterior > flexor digitorum longus(56)	-	Flexor digitorum longus > tibialis posterior
Distal shaft curvature	Slight (convex laterally) to absent	-	Slight, convex laterally ^k	Slight, convex laterally(56)	-	Slight, convex laterally
Morphology of triangular attachment area for inferior interosseous ligament	Poorly marked, superoinferiorly short	Poorly marked, superoinferiorly short	Poorly marked, superoinferiorly short	Well-marked and elongate(56)	Well-marked and elongate	Poorly marked, elongate
Distal tibiofibular articular facet	Small and crescentic	Small and crescentic	Small and crescentic	Small and crescentic(56)	L-shaped (superoinferiorly expanded anteriorly)	Superoinferiorly narrow rectangle
Talar articular surface orientation (as seen in lateral view)	Variably anteriorly or posteriorly tilted(18)	Variably anteriorly tilted or neutral	Anteriorly tilted	Anteriorly tilted(56)	Neutral (90°)	Neutral (90°)
FIBULA						
Malleolar breadth	Broad	-	Broad	Narrow(56)	Broad	Narrow? ^q
Distal tibiofibular articular facet	Small and crescentic	-	Rectangular	Small and crescentic(56)	Oval	-
Talar articular surface orientation	Laterally sloping	-	Vertical	Vertical(56)	Vertical	-
FOOT^f						
Talar trochlear surface	Flat (references in (57))	Flat to slightly grooved	Flat	Deeply grooved(58)	-	Deeply grooved

Talar trochlear medial and lateral radii of curvature	Roughly equal (references in (57))	Roughly equal to elevated medial margin	Roughly equal	Roughly equal(59)	-	Elevated lateral margin
Talar medial malleolar surface	Extends onto talar neck	Extends onto talar neck	Does not extend onto neck	Extends onto talar neck(60)	-	Does not extend onto neck
Talar neck	Short, stout, medially twisted	Short, stout, medially twisted	Short, stout, medially twisted	Short, stout, medially twisted(60)	-	Longer, less robust, not twisted
Talar head/neck orientation angle	Neutral (90°)	Neutral (90°)	Neutral (90°)	Valgus deviation (75°)(60)	-	Varus deviation (105°)
Horizontal angle of talar neck	21°	21°-26°	28°	28°(60)	-	15°-26°(36)
Angle of inclination of talar neck	10°	11°	30°	8° (60)	-	(16°)
Talar neck torsion angle	25°	21°	29°	40° (60)	-	40°
Talar fibular facet/neck length index	195	182	181	125(60)	-	132
Talar head projection index	37	(37)	61	45 (60)	-	-
Talar trochlear breadth/length index	87	80	72	100 (60)	-	(84)
Talar trochlear breadth/fibular facet projection index	253	336	267	330 (60)	-	239
Calcaneal fossa on inferomedial surface for cuboid projection	-	-	Absent	Present(61)	-	-
Metatarsal diaphyses	Gracile	Gracile	Gracile	Robust(58)	-	Gracile(36)

a. As represented by AL 137-48A, AL 211-1, AL 288-1, AL 322-1, AL 333-3, AL 333-4, AL 333-6, AL 333-7, AL 333-9a, AL 333-9b, AL 333-75, AL 333-85, AL 333-95, AL 333-111, AL 333w-37, AL 333X-6/9, AL 333x-26, AL 438-1, Mak VP 1/1 and Mak VP 1/3.

b. As represented by MLD 46, Sts 7, Sts 14, Stw 25, Stw 88, Stw 99, Stw 102, Stw 181, Stw 311, Stw 347, Stw 358, Stw 363, Stw 389, Stw 392, Stw 403, Stw 431, Stw 443, Stw 479, Stw 486, Stw 501, Stw514, Stw 522, Stw 527, Stw 573, and Stw 598.

c. *H. habilis* postcranial hypodigm taken as OH7, OH8, OH35, OH 48, OH62 and KNM ER 3735.

d. Postcranial material conventionally considered to represent early *Homo*, but without associated taxonomically-diagnostic craniodental remains: KNM ER 1472, KNM ER 1475, KNM ER 1481, KNM ER 3228 and OH 28.

- e. *H. erectus (ergaster)* represented by KNM WT 15000, KNM ER 813, KNM ER 1808, KNM BK 66, BSN49/P27, and postcranial material from Dmanisi possibly associated with the D2600 cranium (D4166, D4161, D4507, D4167, D3901, D4110, D2021, D4165, D4058).
- f. As determined from the epiphyseal plate. Observation of adult femora reveals that the points defining the maximum SI diameter of the head correspond, both superiorly and inferiorly, with the line of fusion of the head epiphysis. Therefore the measurement taken on the epiphyseal plate should correspond closely with the actual SI diameter of the head at the time of death. We note also that further appositional growth of the articular surface up until skeletal maturity may have increased this dimension somewhat.
- g. We note that femoral head size tends to be smaller relative to body size in *Australopithecus* compared to *Homo*, which exaggerates somewhat the perception of long arms in *Australopithecus* in the ratio presented here. If the Malapa hominins share with *Australopithecus* the trait of small femoral heads relative to body mass, their relative humeral length would be slightly closer to that observed in *Homo* (thus they would be more *Homo*-like in relative upper limb length, but more *Australopithecus*-like in relative femoral head size).
- h. Damage to the midshaft necessitated use of the mid-proximal diaphysis (at about 70% of biomechanical length, from the distal end) in MH1. Given uniformity in diaphyseal diameters and cortical thickness from this location down to the approximate midshaft, the use of this location is not expected to significantly bias the comparison with other taxa. It should also be noted that MH1 was a juvenile at the time of death (but comparable in age to KNM-WT 15000, whose values are also used), and that adult values may differ. We also note that lack of knowledge of femoral biomechanical length hinders the interpretation of relative upper-to-lower limb strength ratios. Rather than using dubious estimates of femoral length, we instead follow the logic outlined in (40) and limit this comparison to a ratio of unstandardized humeral to femoral dimensions.
- i. Section locations taken between 40-50% of biomechanical length for the humerus, and 50-65% of biomechanical length for the femur (40).
- j. No *A. africanus* specimen preserves both a distal humerus and a femoral head, although Stw 431 preserves a distal humerus and an acetabulum. Femoral head diameter for this specimen was estimated from the diameter of the acetabulum as 36 mm (62).
- k. Based on morphology observable in MH1 juvenile. Additional growth and development to skeletal maturity would have potentially altered morphology.
- l. Estimated from photograph in (36).
- m. TAS = minimum width of the tuberoacetabular sulcus. Based on values provided by (48), the two *Australopithecus* specimens – AL 288-1 and Sts 14 – for which TAS and acetabular width (AD) can be measured have TAS/AD ratios that are 3.5 and 3.7 standard deviations, respectively, above the mean ratio in a sample of 98 modern humans. AL 288-1 and Sts 14 also fall 6.6 and 6.9 standard deviations, respectively, above the mean value obtained for a sample of 18 modern human females. The early *Homo* sample (KNM-ER 3228 and OH 28, both with ratios = 0.25) falls within one standard deviation of both the pooled sex and the female modern human samples. Acetabular diameter in MH1 was estimated from the fossil as between 33 and 35.5 mm: we have used the lower value to produce the most conservative (least *Homo*-like) value possible. The value obtained falls within one standard deviation of the pooled sex sample of modern humans, but 1.6 standard deviations above the modern human female mean.
- n. Acetabuloauricular distance = instrumentally determined minimum distance from margin of auricular surface to the lunate surface. Femoral head SI dimensions were estimated for some specimens (Sts 14, OH 28, ER 3228) from acetabular maximum diameter. Os coxa measurements for some specimens (AL 288-1 and OH 28) were taken on casts.
- o. Intertrochanteric crest to junction between head and neck (63).
- p. The ratio provided is based on KNM WT 15000, which clearly has a long femoral neck relative to the size of the femoral head (and which would have likely gotten longer with continued growth to skeletal maturity). However, the illustration of the D4167 femur (5) suggest that this trait may have been variable in early *H. erectus*.
- q. As judged from the distal fibular metaphysis of KNM WT 15000.

r. Dimensions of the talus were obtained from a 3D virtual reconstruction of the partial foot skeleton of MH2, as illustrated in SOM Figure S5.

REFERENCES

1. P.H.G.M. Dirks, J.M. Kibii, B. F. Kuhn, C. Steininger, S.E. Churchill, J.D. Kramers, R. Pickering, D.L. Farber, A.S. Mériaux, A.I.R. Herries, G.C. P. King, L.R. Berger, *Science* **XXX**, XXX (2009). Companion paper.
2. L. Scheuer, S. Black, *The Juvenile Skeleton* (Elsevier Academic Press, London, 2004).
3. R. L. Susman, *Am. J. Phys. Anthropol.* **137**, 356 (2008).
4. B. H. Smith, in *The Nariokotome Skeleton*, A. C. Walker, R. E. F. Leakey, Eds. (Harvard University Press, Cambridge, 1993), pp. 195-220.
5. P. L. Walker, *Am. J. Phys. Anthropol.* **127**, 385 (2005).
6. S. W. Simpson *et al.*, *Science* **322**, 1089 (2008).
7. D.C. Johanson *et al.*, *Am. J. Phys. Anthropol.* **57** (1982) (all papers within).
8. B. Asfaw, T. White, O. Lovejoy, B. Latimer, S. Simpson, G. Suwa, *Science* **274**, 629-635 (1999).
9. P. V. Tobias, *The Cranium and Maxillary Dentition of Australopithecus (Zinjanthropus) boisei* (Cambridge University Press, Cambridge, 1967).
10. A.W. Keyser, *S. Afr. J. Sci.* **96**, 189-193 (2000).
11. A.W. Keyser, C.G. Menter, J. Moggi-Cecchi, T.R. Pickering, L.R. Berger, *S. Afr. J. Sci.* **96**, 193-197 (2000).
12. P. V. Tobias, *Olduvai Gorge Volume 4: the Skulls, Endocasts and Teeth of Homo habilis* (Cambridge University Press, Cambridge, 1991).
13. N. T. Boaz, F. C. Howell, *Am. J. Phys. Anthropol.* **46**, 93 (1977).
14. W. H. Kimbel, D. C. Johanson, Y. Rak, *Am. J. Phys. Anthropol.* **103**, 235 (1997).
15. R. J. Blumenshine *et al.*, *Science* **299**, 1217 (2003).
16. T. G. Bromage, F. Schrenk, F. W. Zonneveld, *J. Hum. Evol.* **28**, 71 (1995).
17. R. J. Clarke, Unpublished PhD dissertation, University of the Witwatersrand, Johannesburg (1977).
18. R. J. Clarke, *S. Afr. J. Sci.* **104**, 443 (2008).
19. F. E. Grine, B. Demes, W. L. Jungers, T. M. Cole. *Am. J. Phys. Anthropol.* **92**, 411 (1993).
20. F. E. Grine, W. L. Jungers, J. Schultz, *J. Hum. Evol.* **30**, 189 (1996).
21. F. Weidenreich, *Palaeontologia Sinica* **10**, 1 (1943).
22. G. Suwa *et al.*, *Nature* **389**, 489 (1997).

23. A. Rosas, J. M. Bermudez de Castro, *Am. J. Phys. Anthropol.* **107**, 145 (1998).
24. S. C. Anton, *Yrbk. Phys. Anthropol.* **46**, 126 (2003).
25. G. P. Rightmire, D. Lordkipadnize, A. Vekua, *J. Hum. Evol.* **50**, 115 (2006).
26. A. H. Weaver, *Proc. Nat. Acad. Sci.* **102** (10), 3576 (2002).
27. K. J. Carlson, *Am. J. Phys. Anthropol.* **127**, 312 (2005).
28. K. J. Carlson et al., *Int. J. Primatol.* **29**, 1401 (2008).
29. K. J. Carlson et al., in *Primate Locomotion: Linking Field and Laboratory Research*, E. Vereecke, K. D'Aout, Eds. (Springer Press, Berlin, in the press).
30. B. Wood, *Koobi Fora Research Project, Volume 4: Hominid Cranial Remains* (Clarendon Press, Oxford, 1991).
31. B. Zipfel, L. R. Berger, *Palaeont. Afr.* **44**, 77 (2009).
32. C. O. Lovejoy, D. C. Johanson, Y. Coppens, *Am J Phys Anthropol* **57**, 679 (1982).
33. H. M. McHenry, *Am J Phys Anthropol* **87**, 407 (1992).
34. E. Harmon, *J Hum Evol* **56**, 551 (2009).
35. D. C. Johanson et al., *Nature* **327**, 205 (1987).
36. D. Lordkipadnize et al., *Nature* **449**, 305 (2007).
37. A. C. Walker, R. E. Leakey, in *The Nariokotome Skeleton*, A. C. Walker, R. E. Leakey, Eds. (Harvard University Press, Cambridge, 1993), pp. 95-160.
38. F. Spoor et al., *Nature* **448**, 688 (2007).
39. B. G. Richmond, L. C. Aiello, B. A. Wood, *J Hum Evol* **43**, 529 (2002).
40. C. Ruff, *Am J Phys Anthropol* **138**, 90 (2009).
41. C. Ruff, *J Hum Evol* **54**, 383 (2008).
42. C. O. Lovejoy, D. C. Johanson, Y. Coppens, *Am J Phys Anthropol* **57**, 637 (1982).
43. M. Haeusler, H. M. McHenry, *J Hum Evol* **53**, 383 (2007).
44. R. E. Leakey, A. Walker, C. V. Ward, H. M. Grausz, in *Hominidae: Proceedings of the 2nd International Congress of Human Paleontology*, G. Giacobini, Ed. (Jaca Book, Turin, 1989), pp. 167-173.
45. R. E. F. Leakey, A. C. Walker, *Am J Phys Anthropol* **67**, 135 (1985).
46. R. E. Leakey, A. Walker, in *Hominidae: Proceedings of the 2nd International Congress of Human Paleontology*, G. Giacobini, Ed. (Jaca Book, Turin, 1989), pp. 209-215.

47. M. S. M. Drapeau, C. V. Ward, W. H. Kimbel, D. C. Johanson, Y. Rak, *J Hum Evol* **48**, 593 (2005).
48. J. T. J. Stern, R. L. Susman, *Am J Phys Anthropol* **60**, 279 (1983).
49. M. D. Rose, *Am J Phys Anthropol* **63**, 371 (1984).
50. C. O. Lovejoy, R. S. Meindl, J. C. Ohman, K. G. Heiple, T. D. White, *Am J Phys Anthropol* **119**, 97 (2002).
51. K. E. Reed, J. W. Kitching, F. E. Grine, W. L. Jungers, L. Sokoloff, *Am J Phys Anthropol* **92**, 1 (1993).
52. F. E. Grine, W. L. Jungers, P. V. Tobias, O. M. Pearson, *Am. J. Phys. Anthropol.* **97**, 151 (1995).
53. D. C. Johanson *et al.*, *Am J Phys Anthropol* **57**, 403 (1982).
54. M. Haeusler, H. M. McHenry, *J Hum Evol* **46**, 433 (2004).
55. L. R. Berger, P. V. Tobias, *J Hum Evol* **30**, 343 (1996).
56. P. R. Davis, *Nature* **201**, 967 (1964).
57. J. T. J. Stern, R. L. Susman, *Am J Phys Anthropol* **60**, 279 (1983).
58. W. E. H. Harcourt-Smith, L. C. Aiello, *J Anat* **204**, 403 (2004).
59. M. H. Day, J. R. Napier, *Nature* **201**, 969 (1964).
60. L. S. B. Leakey, P. V. Tobias, J. R. Napier, in *Nature*. (1964), vol. 202, pp. 7-9.
61. M. H. Day, B. A. Wood, *Man* **3**, 440 (1968).
62. R. L. Susman, J. T. Stern, *Science* **217**, 931 (1982).
63. H. M. McHenry, L. R. Berger, *J Hum Evol* **35**, 1 (1998).
64. L. C. Aiello, M. C. Dean, *An introduction to human evolutionary anatomy*. (Academic Press, London, 1990).

Geological Setting and Age of *Australopithecus sediba* from Southern Africa

Paul H. G. M. Dirks,^{1,2*} Job M. Kibii,³ Brian F. Kuhn,³ Christine Steininger,^{3,2} Steven E. Churchill,^{4,3} Jan D. Kramers,^{2,5,6} Robyn Pickering,⁷ Daniel L. Farber,^{8,9} Anne-Sophie Mériaux,¹⁰ Andy I. R. Herries,^{11,12} Geoffrey C. P. King,¹³ Lee R. Berger^{3,2}

We describe the geological, geochronological, geomorphological, and faunal context of the Malapa site and the fossils of *Australopithecus sediba*. The hominins occur with a macrofauna assemblage that existed in Africa between 2.36 and 1.50 million years ago (Ma). The fossils are encased in water-laid, clastic sediments that were deposited along the lower parts of what is now a deeply eroded cave system, immediately above a flowstone layer with a U-Pb date of 2.026 ± 0.021 Ma. The flowstone has a reversed paleomagnetic signature and the overlying hominin-bearing sediments are of normal polarity, indicating deposition during the 1.95- to 1.78-Ma Olduvai Subchron. The two hominin specimens were buried together in a single debris flow that lithified soon after deposition in a phreatic environment inaccessible to scavengers.

Two hominin fossils assigned to *Australopithecus sediba* (*I*) were found in deposits in Malapa cave (Fig. 1). This newly discovered site is one of several Plio-Pleistocene cave deposits in the Cradle of Humankind World Heritage Site (South Africa) that host hominin fossils and associated faunal and archaeological remains, including Sterkfontein, Swartkrans, Kromdraai, and Coopers (2–8). The fossiliferous deposits in these caves formed in broadly similar ways, mostly as debris cone accumulations beneath vertical cave openings (6–11). Clastic sedimentation alternated with periods of erosion (7) or flowstone formation (11), producing unconformities representing time markers between caves. Here we describe the geological, geochronological, geomorphological, and faunal context of the Malapa site and the fossils of *Au. sediba* (*I*).

Malapa cave formed in stromatolite-rich dolomite of the late Archaean [2.64 to 2.50 billion

years ago (Ga)] Malmani Subgroup (12, 13), which is subdivided into five formations (from base to top: the Oaktree, Monte Christo, Lyttelton, Eccles, and Frisco formations) (13, 14). Malapa cave is located 15 km north-northeast of Sterkfontein, in the steep-sided valley of the spring-fed Grootvleispruit. It is situated at the north end of a line of north-south-trending caves that are stratigraphically bound to the top 40 m of the 155-m-thick Lyttelton Formation, in layered dolomite that dips 8° to 13° to the north-northwest, an

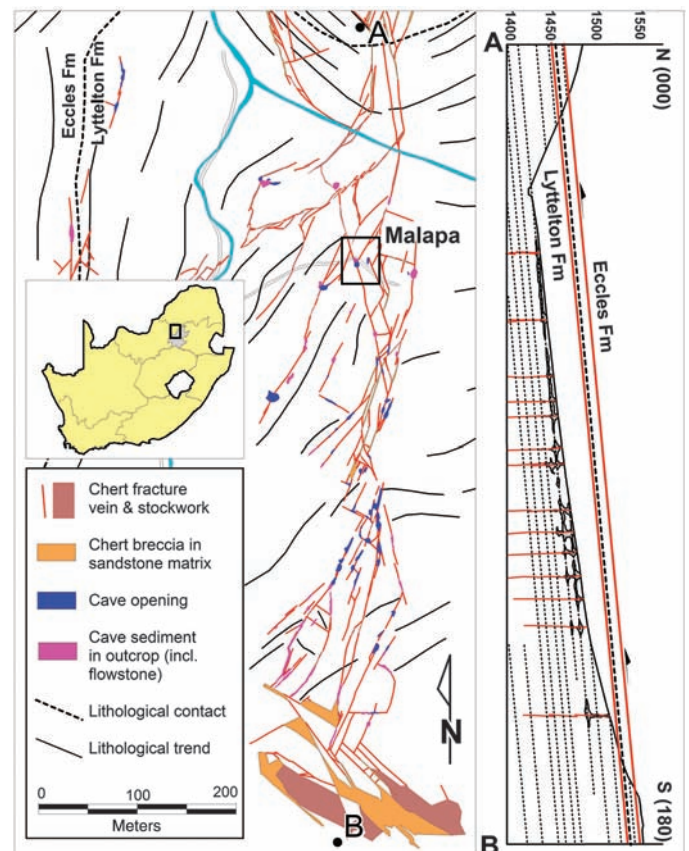
angle 2° to 5° shallower than the slope of the valley where the caves are exposed (Fig. 1).

Caves near Malapa define a 500-m-long and 100-m-wide network of interconnected openings along chert-filled fractures (Fig. 1). In the immediate vicinity of Malapa (elevation: 1442 m above mean sea level), erosion remnants of cave deposits form shallow depressions. Caves farther upslope are progressively deeper and preserve interconnected subterranean caverns that reach a vertical depth of 25 to 30 m. The cave system closes above an elevation of ~ 1490 m, directly below the sheared upper contact of the Lyttelton formation (Fig. 1). These trends, combined with valley slope and bedding orientation, suggest that Malapa lies near the base of an originally >30 -m-deep, strata-bound and fracture-controlled cave system eroded by valley incision.

Malapa cave formed at the intersection of a north-northeast and a north-northwest fracture, with hominin remains occurring in a 3.5-m-deep excavation (3.3 m by 4.4 m in size) centered on the north-northwest fracture. Minor limestone mining took place at Malapa in the early 20th century, exposing in situ hominin material. The cave deposits comprise five distinct sedimentary facies called, from base to top, A to E. Facies A–B occur below a central flowstone sheet (Fig. 2 and fig. S1). The fossils of *Au. sediba* (*I*) are in facies D, with additional hominin remains in facies E (Fig. 2).

Facies A consists of dark-colored, moderately sorted, coarse-grained clastic sediment, with abun-

Fig. 1. Location of the Malapa site in the valley of the Grootvleispruit, showing the principal geological controls on cave formation. Malapa is positioned along a complex fracture system in the most deeply eroded parts of a 500-m-long cave system as illustrated by section A–B.



¹School of Earth and Environmental Sciences, James Cook University, Townsville, QLD 4811, Australia. ²School of Geosciences, University of the Witwatersrand, Johannesburg, Private Bag 3, Wits 2050, South Africa. ³Institute for Human Evolution, University of the Witwatersrand, Johannesburg, Private Bag 3, Wits 2050, South Africa. ⁴Department of Evolutionary Anthropology, Box 90383, Duke University, Durham, NC 27708, USA. ⁵Institute of Geological Sciences, University of Bern, Baltzerstrasse 3, 3012 Bern, Switzerland. ⁶Department of Geology, University of Johannesburg, Auckland Park 2006, South Africa. ⁷School of Earth Sciences, University of Melbourne, VIC 3010, Australia. ⁸Center for Accelerator Mass Spectrometry, Lawrence Livermore National Laboratory, Livermore, CA 94550, USA. ⁹Department of Earth and Planetary Sciences, University of California, Santa Cruz, Santa Cruz, CA 95064, USA. ¹⁰School of Geography, Politics and Sociology, Newcastle University, Claremont Road, Newcastle upon Tyne NE1 7RU, UK. ¹¹UNSW Archaeomagnetism Laboratory, School of Medical Sciences, University of New South Wales, Sydney, NSW 2052, Australia. ¹²Geomagnetism Laboratory, Oliver Lodge, Department of Earth and Ocean Science, University of Liverpool, L69 3BX, UK. ¹³Laboratoire Tectonique, Institut de Physique du Globe Paris, 4 Place Jussieu, 75252 Paris, France.

*To whom correspondence should be addressed. E-mail: paul.dirks@jcu.edu.au

dant rounded grains (0.5 to 6 mm) of chert, quartz, dolomite, iron oxide-coated grains or ooids, bone fragments and peloids, and little feldspar and mica schist. The openly packed framework grains are embedded in blocky sparite. Bedding is defined by normal and inverse grading, and a weak preferred orientation of rock and bone fragments. The coarsest-grained parts of facies A occur toward the center of the unit defining a shallow central channel.

Facies B consists of peloidal grainstone alternating with clastic sandstone. The grainstone contains >50% rounded peloids and lesser amounts of bone fragments and clastic grains (mostly quartz), many iron oxide-coated, to form an open framework cemented with blocky sparite. Fenestrae with sparry calcite are common along horizontal bedding planes. Peloids (0.4 to 1 mm) consist of fine-grained (0.02 to 0.10 mm) angular quartz grains in a micaceous mud and sparite matrix. Sandstone rich in bone fragments and rounded iron oxide-coated grains forms layers preserving grading (coarsening and fining upward) and grain imbrication. Small stalagmite bosses growing on a grainstone substrate, and isolated limestone blocks (<40 cm), are incorporated in facies B.

After deposition, facies A and B were eroded and covered by a flowstone carapace that dips moderately to the north-northeast, indicating north-directed water flow along the cave axis. The flowstone contains intercalations of fossil-bearing, detrital sandstone. A milky quartz vein

surrounded by an alteration halo of iron oxide and clay intruded facies A–B, but does not appear to intrude the flowstone (Fig. 2).

Facies C is identical to the peloidal grainstone units in facies B. It is preserved as a 5- to 30-cm-thick erosion remnant that drapes over the flowstone in the northwest corner of the pit (Fig. 2). Subrounded fragments of quartz, limestone, and shale, many iron oxide-coated, as well as bone fragments, occur toward the top of the layer, and fenestrae are common.

Facies D overlies flowstone in the center and east of the pit and sits unconformably on facies C in the west. This massive, up to 1.5-m-thick, light-colored unit contains abundant, well-preserved macro- and micromammal fossils, including the remains of two skeletons of *Au. sediba* (1) and articulated remains of *Equus* sp. (Fig. 2). The poorly sorted, coarse-grained sandstone is cemented by blocky sparite, which displays isopachous (radial outward) overgrowths in larger pore spaces. Framework grains are mostly 0.5 to 2.5 mm in size and consist of quartz, chert, dolomite, peloids, and, less commonly, iron oxide-coated grains, ooids, shale, and feldspar (microcline). Rounding varies from well-rounded ooids to angular vein-quartz crystals. Angular limestone blocks (<50 cm) and flowstone fragments (<5 cm) occur throughout facies D. Peloids are common, but peloidal boundaries are diffuse, and groups of peloids are fused in irregular patches. The hominin skeletons are in close spatial association, separated by no

more than 40 cm vertically (Fig. 2). The recovered remains of the juvenile occur in close association (1) toward the top of facies D, and the partly articulated remains of the adult (1) occur near the base.

Facies E consists of calcareous sandstone, similar to facies D, but darker colored and finer grained, with a higher degree of sorting and rounding, and preserving 4- to 15-cm-scale horizontal layering. The basal layer of facies E consists of well-sorted, coarse-grained sandstone dominated by 0.6- to 1.5-mm-large iron oxide-coated chert and quartz grains and aggregates of peloids. The layer preserves northwest-dipping laminations, indicating directional water flow. Horizontal layering in facies E is defined by grain-size variations (coarsening and fining upward), mud partings, thin (<1 mm) flowstone drapes, and orientated bone fragments. Fossil bone is abundant, but less well preserved than bone in facies D, with solution damage and partial fragmentation suggesting exposure to standing or flowing water before final burial and cementation (15).

The rocks of facies A–E were water-laid with all sandstone units displaying loose packing of framework grains indicating little postdepositional compaction (16). Abundant fenestrae in facies B and C reflect trapped gas possibly formed from the decay of organic matter (16, 17). The abundant peloids are interpreted as fecal remains (16, 17) or soil micropeds (11, 18). Coalescence of peloids in facies D and E reflects mechanical

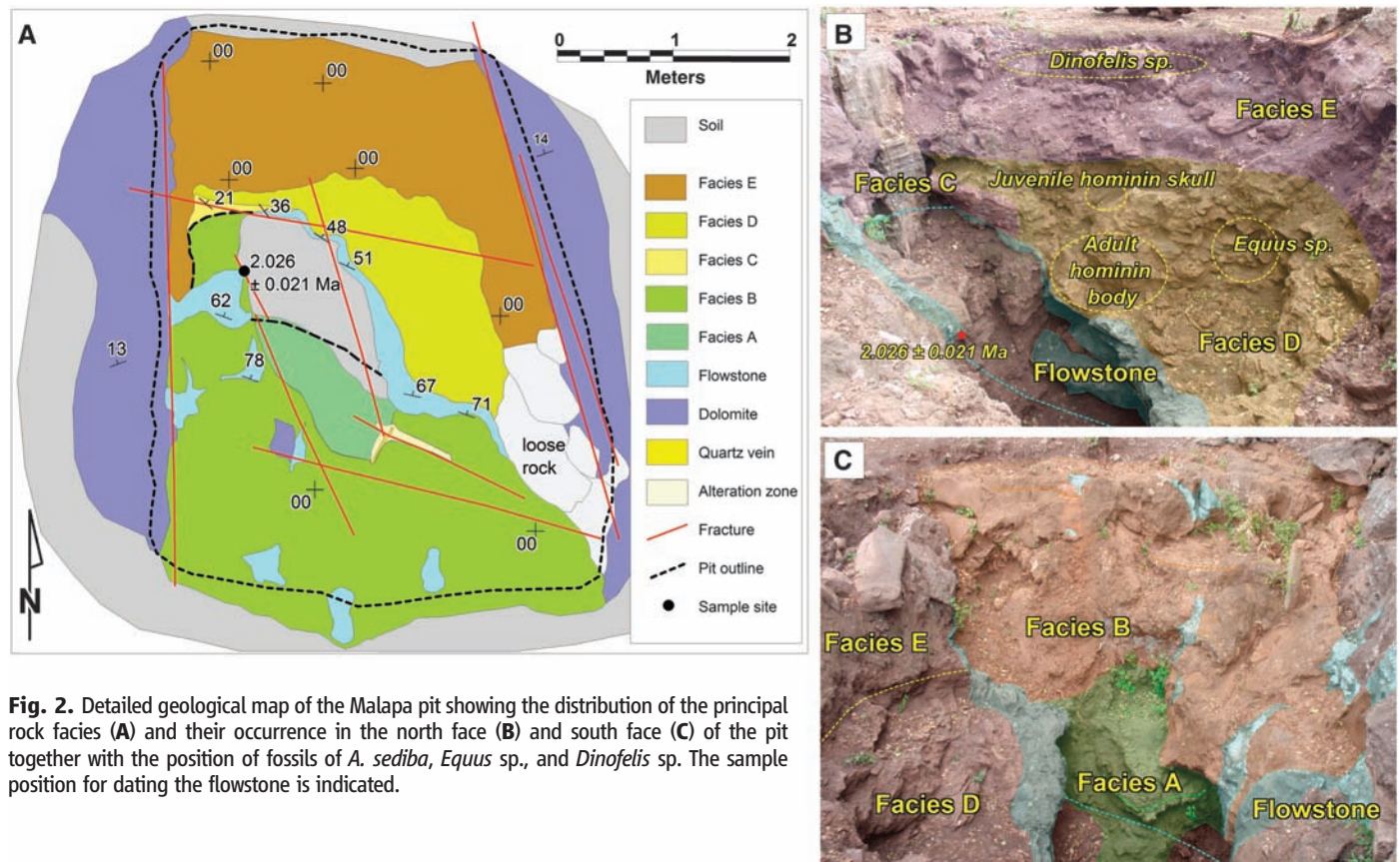


Fig. 2. Detailed geological map of the Malapa pit showing the distribution of the principal rock facies (A) and their occurrence in the north face (B) and south face (C) of the pit together with the position of fossils of *A. sediba*, *Equus* sp., and *Dinofelis* sp. The sample position for dating the flowstone is indicated.

reworking of unconsolidated peloids deposited in a water-logged environment. The homogeneous sandstone of facies D contains allochthonous material (chert, shale and feldspar grains, bone fragments) mixed with cave-derived sediment and coarse blocks, suggesting deposition as a single debris flow that carried partially articulated (i.e., only partially decomposed) hominins with it. The superb preservation and state of articulation of fossil material (1) indicate rapid deposition, limited transport distance, and laminar flow conditions consistent with debris flows (17, 19). The presence of isopachous sparite indicates that cementation occurred soon after deposition in a phreatic environment (16). After the debris flow, the cave filled with horizontally layered clastic deposits (facies E) dominated by autochthonous sediment with sedimentary structures indicating north-directed water flow that weakened and strengthened from time to time, carrying with it bone fragments and partially articulated faunal remains. Absence of carnivore damage in the fossil assemblage indicates that scavengers had no access to the cave.

We collected 209 nonhominin fossil specimens from facies D–E, of which 25 specimens have been identified to at least the genus level (Table 1). Representatives of the extant species *Felis silvestris* and *Parahyaena brunnea*, as well as *Lycaon* sp., *Tragelaphus* cf. *strepsiceros*, and *Equus* sp., have their earliest recorded appearance in Africa at ~2.36 million years ago (Ma) (20–22). The extinct felid *Megantereon whitei* collected from facies E has a last recorded appearance in Africa at ~1.5 Ma (23). These ages thus bracket the depositional age of the fossil hominins.

The flowstone underlying facies C and D was dated independently at two separate laboratories (Bern and Melbourne) by slightly different U-Pb techniques (8, 24) (SOM Text S1). Dates were obtained from thin, U-bearing (0.7 parts per million) seams near the base of a flowstone sheet (figs. S1 and S2) stratigraphically 20 cm below the adult hominin skeleton (Fig. 2), but separated from the skeleton by an erosional surface along the top of the flowstone. The dates of 2.024 ± 0.062 Ma (Bern) and 2.026 ± 0.021 Ma (Melbourne) are identical within error and provide a maximum

age limit for the hominin remains (table S1 and fig. S3).

To further constrain the age of deposition of the fossils, we took samples for paleomagnetic analysis from across the flowstone layer and the overlying sedimentary facies (SOM Text S2, table S3, and figs. S1, S4, and S5). The flowstone mainly preserves reverse polarity, but near its base, a normal polarity excursion occurs that is interpreted as the Huckleberry Ridge Subchron at 2.06 ± 0.04 Ma (25). The sediments of facies C, D, and E above the flowstone record normal polarity that is interpreted as the beginning of the 1.95- to 1.78-Ma Olduvai Subchron (26).

To constrain the level of erosion and original depth of the cave system, we collected samples for cosmogenic ^{10}Be analysis from two sites (SOM Text S3, table S4, and fig. S6) to bracket the minimum and maximum erosion rates Malapa experienced: (i) the plateau 650 m south and 82 m above Malapa (TNHL08) equated to the African Erosion Surface (5) that is thought to have experienced low erosion rates (<10 m) over the past tens of millions of years, and (ii) the gently northwest-dipping bedrock channel of the Grootvleispruit, 3400 m west-northwest and 85 m below Malapa (LH08). Samples from TNHL08 give consistent values for the long-term erosion rate of the surface of ~3 to 5 m per million years (My) with a mean of 3.6 ± 1.1 m/My (table S5). These rates are more than an order of magnitude higher than are common in ancient relic landscapes (27–29) and indicate that over the past ~2 million years, at least ~8 m of overburden was removed from Malapa. To constrain the down-cutting rate of the river into shale overlying the Malmani Subgroup, and thus the rate of valley formation, we collected bedrock samples from LH08 from a chert layer forming a dip slope and the stream channel (SOM Text S3 and fig. S7). A linear fit to data collected from ~1 to 6 m above the active channel spans a time frame of 10^5 years and yields a river incision rate of 53 ± 9 m/My (fig. S8). This suggests that erosion rates at Malapa are significantly greater than those measured on the plateau, indicating that Malapa cave was tens of meters deep when the *Hominin* fossils were deposited.

As a taphonomic hypothesis, we suggest that at the time of burial of the hominins, the complex cave system near Malapa had opened along deep vertical shafts that operated as death traps to animals on the surface (Fig. 3). In addition to being inconspicuous drops into which animals accidentally wandered, the cave openings may have been loci of animal activity, enhancing their operation as natural traps. Animals might have been attracted to the smell of water coming from the shaft, and carnivores might have been attracted to the smell of decomposing bodies. These factors could have operated to accumulate a diverse assemblage of carcasses in the chamber below, away from carnivore activity. The sediments imply that subsequent high-volume water inflow, perhaps the result of a large storm, caused a

Table 1. Nonhominin faunal material recovered from Malapa with estimates of minimum numbers of individuals (MNI) and number of identified specimens (NISP).

Order	Family	Tribe	Genus and species	MNI	NISP	
Carnivora	Felidae		<i>Dinofelis</i> sp.	1	2	
			<i>Megantereon whitei</i>	1	1	
			<i>Felis silvestris</i>	1	1	
		Hyaenidae		<i>Parahyaena brunnea</i>	2	8
		Canidae		<i>Lycaon</i> sp.	1	1
		Herpestidae		<i>Atilax mesotes</i> *	1	1
Perissodactyla	Equidae		<i>Mungos</i> sp.	1	1	
			<i>Equus</i> sp.	1	1	
Artiodactyla	Suidae		<i>Equus</i> sp.	1	1	
			<i>Suidae</i> Indet.	1	1	
	Bovidae	Neotragini	<i>Oreotragus</i> sp.	1	1	
		Alcelaphini	<i>Megalotragus</i> sp.	1	1	
		Large-sized alcelaphine	1	1		
		Tragelaphini	<i>Tragelaphus</i> cf. <i>scriptus</i>	1	1	
			<i>Tragelaphus</i> cf. <i>strepsiceros</i>	1	1	
Lagomorpha	Leporidae		<i>Lepus</i> sp.	1	3	
Total				16	25	

*Considered by some to be *Herpestes mesotes*.

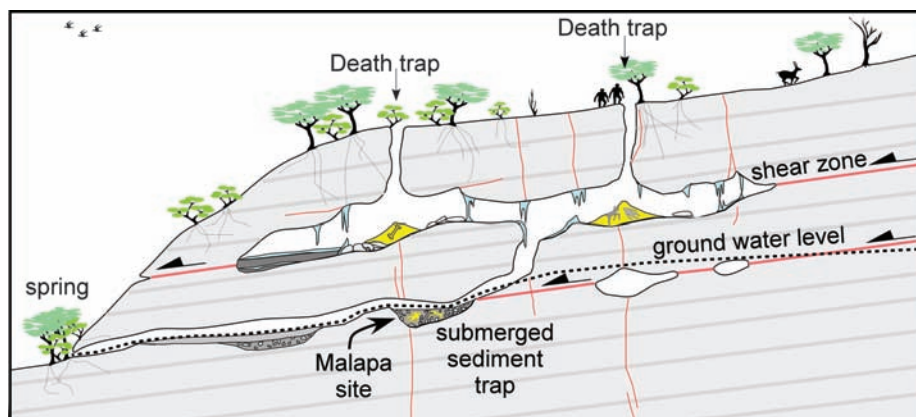


Fig. 3. Cartoon illustrating how two hominins might have become trapped and buried in alluvial sediments at the bottom of a Pliocene cave.

debris flow that carried the still partially articulated bodies deeper into the cave, to deposit them along a subterranean stream (Fig. 3).

References and Notes

- L. R. Berger *et al.*, *Science* **328**, 195 (2010).
- R. Broom, J. T. Robinson, *Nature* **164**, 322 (1949).
- A. R. Hughes, P. V. Tobias, *Nature* **265**, 310 (1977).
- R. Clarke, *S. Afr. J. Sci.* **94**, 460 (1998).
- T. C. Partridge, in *The Cenozoic of Southern Africa*, T. C. Partridge, R. R. Maud, Eds. (Oxford Univ. Press, New York, 2000), pp. 100–125.
- T. C. Partridge, D. E. Granger, M. W. Caffee, R. J. Clarke, *Science* **300**, 607 (2003).
- C. K. Brain, in *Swartkrans: A Cave's Chronicle of Early Man*, C. K. Brain, Ed. (Monogr. 8, Transvaal Museum, Pretoria, ed. 2, 2004).
- D. J. de Ruiter *et al.*, *J. Hum. Evol.* **56**, 497 (2009).
- T. C. Partridge, *Nature* **275**, 282 (1978).
- C. K. Brain, in *Palaeoclimate and Evolution, with Emphasis on Human Origins*, E. S. Vrba, Ed. (New Haven, 1995), pp. 385–424.
- R. Pickering *et al.*, *J. Hum. Evol.* **53**, 602 (2007).
- D. McB. Martin, C. W. Clendennin, B. Krapez, N. J. McNaughton, *J. Geol. Soc. London* **155**, 311 (1998).
- P. G. Eriksson *et al.*, in *The Geology of South Africa*, M. R. Johnson, C. R. Anhaeusser, R. J. Thomas, Eds. (Geological Society of South Africa, Johannesburg, 2006), pp. 237–260.
- K. A. Eriksson, J. F. Truswell, *Trans. Geol. Soc. S. Afr.* **77**, 211 (1974).
- C. K. Brain, *The Hunters or the Hunted? An Introduction to African Cave Taphonomy* (Univ. of Chicago Press, Chicago, 1981).
- H. Blatt *et al.*, *Petrology: Igneous, Sedimentary and Metamorphic* (Freeman, New York, ed. 3, 2006).
- M. E. Tucker, *Sedimentary Petrology* (Blackwell, Oxford, ed. 2, 1991).
- G. J. Retallack, *Soils of the Past: An Introduction to Palaeopedology* (Harper Collins, London, 1990).
- P. Cossot, M. Meunier, *Earth Sci. Rev.* **40**, 209 (1996).
- L. R. Berger, R. Lacruz, D. J. De Ruiter, *Am. J. Phys. Anthropol.* **119**, 192 (2002).
- J. P. Brugal, H. Roche, M. Kibunjia, *C. R. Palevol.* **2**, 675 (2003).
- F. H. Brown, I. McDougall, I. Davies, R. Maier, in *Ancestors: The Hard Evidence*, E. Delson, Ed. (Liss, New York, 1985), pp. 82–90.
- M. E. Lewis, L. Werdelin, in *Hominin Environments in the East African Pliocene: An Assessment of the Faunal Evidence*, R. Boe, Z. Alemseged, A. K. Behrensmeyer, Eds. (Springer, Netherlands, 2007), pp. 77–105.
- J. D. Woodhead *et al.*, *Quat. Geochronol.* **1**, 208 (2006).
- M. A. Lanphere, D. E. Champion, R. L. Christiansen, G. A. Izett, *GSA Bull.* **114**, 559 (2002).
- J. G. Ogg, A. G. Smith, in *A Geologic Time Scale 2004*, F. Gradstein, J. G. Ogg, A. G. Smith, Eds. (Cambridge Univ. Press, Cambridge, UK, 2004), pp. 63–86.
- K. Nishiizumi, M. W. Caffee, R. C. Finkel, G. Brimhall, T. Mote, *Earth Planet. Sci. Lett.* **237**, 499 (2005).
- S. R. Hall, D. L. Farber, L. Audin, R. C. Finkel, A. S. Meriaux, *Tectonophysics* **459**, 186 (2008).
- A. Matmon *et al.*, *Geol. Soc. Am. Bull.* **121**, 688 (2009).

We thank the South African Heritage Resource Agency for allowing work on the Malapa site; the Nash family for granting access to the Malapa site and continued support; the Palaeontological Scientific Trust (PAST), the Institute for Human Evolution, University of the Witwatersrand and the School of Geosciences, University of the Witwatersrand, for funding; and the University of the Witwatersrand's Schools of Geosciences and Anatomical Sciences and the Bernard Price Institute for Palaeontology for support and facilities. Further support was provided by AfricaArray (P.H.G.M.D.), the France-SA, !Khole Africa project (G.C.P.K., D.L.F., A.-S.M.), and LLNL GEO-CAMS and the US-NSF EAR-0345895 (D.L.F.). R.P. is supported by a Swiss National Science Foundation Post-Doctoral Grant and gratefully acknowledges J. Woodhead, A. Grieg, and the team at Melbourne University. A.I.R.H. was funded through a UNSW Faculty of Medicine research grant and ARC Discovery Grant DP0877603 and acknowledges the support of the Liverpool University Geomagnetism Laboratory staff. Contributions to mapping and sample preparation by G. Charlesworth and Z. Jinnah are kindly acknowledged.

Supporting Online Material

www.sciencemag.org/cgi/content/full/328/5975/205/DC1
SOM Text S1 to S3
Figs. S1 to S8
Tables S1 to S4
References

19 November 2009; accepted 26 February 2010
10.1126/science.1184950

Why Copy Others? Insights from the Social Learning Strategies Tournament

L. Rendell,^{1*} R. Boyd,² D. Cownden,³ M. Enquist,^{4,5} K. Eriksson,^{5,6} M. W. Feldman,⁷ L. Fogarty,¹ S. Ghirlanda,^{5,8} T. Lillicrap,⁹ K. N. Laland^{1*}

Social learning (learning through observation or interaction with other individuals) is widespread in nature and is central to the remarkable success of humanity, yet it remains unclear why copying is profitable and how to copy most effectively. To address these questions, we organized a computer tournament in which entrants submitted strategies specifying how to use social learning and its asocial alternative (for example, trial-and-error learning) to acquire adaptive behavior in a complex environment. Most current theory predicts the emergence of mixed strategies that rely on some combination of the two types of learning. In the tournament, however, strategies that relied heavily on social learning were found to be remarkably successful, even when asocial information was no more costly than social information. Social learning proved advantageous because individuals frequently demonstrated the highest-payoff behavior in their repertoire, inadvertently filtering information for copiers. The winning strategy (discountmachine) relied nearly exclusively on social learning and weighted information according to the time since acquisition.

Human culture is widely thought to underlie the extraordinary demographic success of our species, manifest in virtually every terrestrial habitat (1, 2). Cultural processes facilitate the spread of adaptive knowledge, accumulated over generations, allowing individuals to acquire vital life skills. One of the foundations of culture is social learning, learning influenced by observation or interaction with other individuals (3), which occurs widely in various forms across the animal kingdom (4). Yet it remains something of a mystery why individuals profit by copying others and how best to do this.

At first sight, social learning appears advantageous because it allows individuals to avoid

the costs, in terms of effort and risk, of trial-and-error learning. However, social learning can also cost time and effort, and theoretical work reveals that it can be error-prone, leading individuals to acquire inappropriate or outdated information in nonuniform and changing environments (5–11). Current theory suggests that to avoid these errors individuals should be selective in when and how they use social learning, so as to balance its advantages against the risks inherent in its indiscriminate use (9). Accordingly, natural selection is expected to have favored social learning strategies, psychological mechanisms that specify when individuals copy and from whom they learn (12, 13).

These issues lie at the interface of multiple academic fields, spanning the sciences, social sciences and humanities, from artificial intelligence to zoology (5, 14–18). Formal theoretical analyses [e.g., (2, 5–9, 11–13, 19)] and experimental studies (20, 21) have explored a small number of plausible learning strategies. Although insightful, this work has focused on simple rules that can be studied with analytical methods and can only explore a tiny subset of strategies. For a more authoritative understanding of when to acquire information from others and how best to do so, the relative merits of a large number of alternative social learning strategies must be assessed. To address this, we organized a computer tournament in which strategies competed in a complex and changing simulation environment. €10,000 was offered as first prize. The organization of similar tournaments by Robert Axelrod in the 1980s proved an extremely effective means for

¹Centre for Social Learning and Cognitive Evolution, School of Biology, University of St. Andrews, Queen's Terrace, St. Andrews, Fife KY16 9TS, UK. ²Department of Anthropology, University of California, Los Angeles, CA 90095, USA. ³Department of Mathematics and Statistics, Queen's University, Jeffrey Hall, University Avenue, Kingston, Ontario K7L 3N6, Canada. ⁴Department of Zoology, Stockholm University, 11691 Stockholm, Sweden. ⁵Centre for the Study of Cultural Evolution, Stockholm University, 11691 Stockholm, Sweden. ⁶School of Education, Culture, and Communication, Mälardalen University, 72123 Västerås, Sweden. ⁷Department of Biological Sciences, Stanford University, Stanford, CA 94305, USA. ⁸Department of Psychology, University of Bologna, 40127 Bologna, Italy. ⁹Centre for Neuroscience Studies, Queen's University, 18 Stuart Street, Kingston, Ontario K7L 3N6, Canada.

*To whom correspondence should be addressed. E-mail: ler4@st-andrews.ac.uk (L.R.); knl1@st-andrews.ac.uk (K.N.L.)



Supporting Online Material for

Geological Setting and Age of *Australopithecus sediba* from Southern Africa

Paul H. G. M. Dirks,* Job M. Kibii, Brian F. Kuhn, Christine Steininger, Steven E. Churchill, Jan D. Kramers, Robyn Pickering, Daniel L. Farber, Anne-Sophie Mériaux, Andy I. R. Herries, Geoffrey C. P. King, Lee R. Berger

*To whom correspondence should be addressed. E-mail: paul.dirks@jcu.edu.au

Published 9 April 2010, *Science* **328**, 205 (2010)
DOI: 10.1126/science.1184950

This PDF file includes:

SOM Text S1 to S3
Figs. S1 to S8
Tables S1 to S4
References

Geological Setting and Age of Australopithecus sediba from Southern Africa

Paul H.G.M. Dirks*, Job M. Kibii, Brian F. Kuhn, Christine Steininger, Steven E. Churchill, Jan D. Kramers, Robyn Pickering, Daniel L. Farber, Anne-Sophie Mériaux, Andy I.R. Herries, Geoffrey C. P. King, Lee R. Berger

*To whom correspondence should be addressed. Email: paul.dirks@jcu.edu.au

This PDF file includes:

Text S1, S2, S3

Figures S1, S2, S3, S4, S5, S6, S7 and S8

Tables S1, S2 and S3 and S4

References

Text S1. U-Pb dating of flowstone from the Malapa site.

Of 4 samples taken by JDK from the flowstone layer immediately underlying the hominin-bearing fossil unit (facies D) in January and February 2009, only one (NHL 09/2) has layers containing sufficient U for U-Pb dating (about 0.7 ppm U, see below; Fig. S1). The sample was halved with both halves (NHL 09/2a and NHL 09/2b) containing all layers of the

flowstone. U-Pb analyses were conducted at the University of Bern (sample NHL 09/2a) by JDK and at the University of Melbourne (sample NHL 09/2b) by RP in July 2009. JK did not communicate his results to RP before the latter's analyses and data reduction were finalized (except for $^{234}\text{U}/^{238}\text{U}$ activity ratios) ensuring a blind test.

i) Sample pre-screening

The success of U-Pb dating of speleothems in part depends on the U concentrations in collected samples. As a rule, flowstones in the Cradle of Humankind site have extremely low U contents (less than 0.05 ppm), with only rare, localized, U-rich layers, making pre-screening of a range of samples a necessary step. In Bern a FUJIFilm BAS-1800 beta-scanner was used to pre-screen samples for their U content. This technique utilises an erasable X-ray imaging plate that stores radiation emitted from the samples, in this case, from the U (for detail see (S1)). At the University of Melbourne pre-screening was done with laser-ablation using a 193nm excimer laser ablation system (termed 'HelEx') coupled to a Varian high sensitivity quadrupole ICPMS. The mobile stage of the HelEx set up allows for continuous-track laser scans, which can be used to map the U, Pb and other trace element concentrations through the sample (S2). Sample NHL09/2b was cut in half, smoothed and cleaned in distilled water ultrasonically. Three pre-ablation runs with a slit width of 350 μm were done next to clean off any surface contamination. The sample run is bracketed with shots of NIST 612 glass, all runs using a 55 μm spot size at 5Hz. Data reduction and concentration calculations was done using the Iolite software (<http://www.earthsci.unimelb.edu.au/isotope/iolite/index.html>). The laser ablation data for U and Pb is plotted against time and superimposed (to scale) over the NHL09/2b sample in Fig. S2.

From both the beta-scanner image and the laser data, two U-rich layers towards the base of the sample are apparent. This positioning of U-rich layers in the first few cm above the underlying sediments is a pattern observed at all the caves in this region (*S1*, *S3*). In sample NHL09/2b, these layers are labelled b1, b2 and b3 (Fig. S2). Layer b1 corresponds to the layer identified via beta-scanner image in sample NHL09/2a, and dated in Bern.

ii) Sample preparation and measurements

Blocks from the U-rich layers smaller than 0.5cm in size were mechanically removed using a dentist drill (Melbourne) or small diamond wheel saw (Bern). Mixed spikes added in dissolution were ($^{236}\text{U} + ^{202}\text{Pb}$) in Bern and ($^{233}\text{U} + ^{205}\text{Pb}$) in Melbourne. U-Pb isotope measurements were done using Nu-Instruments multicollector ICP-mass spectrometers in both locations. Chemical separation and measurement protocols were as described in (*S4*) for Melbourne, and as in (*S1*) for Bern.

iii) Data and age calculations

Results are shown in Table S1. U concentrations for layers 1 and 2 were between 0.6 and 0.9 $\mu\text{g/g}$ with Pb varying from 0.002 to 0.028 $\mu\text{g/g}$. Analytical Pb blanks were 50 pg (Bern) and 5-15 pg (Melbourne) and results were blank corrected. In sample NHL09/2b, Layer b1 contained the most radiogenic Pb, with 206/204 ratios of up to 34. This corresponds closely to the range of values for the layer in sample NHL09/2a analysed in Bern (Table S1). Layer b3 is low in U and

dominated by common Pb, and is, therefore not suitable for dating. This layer is also very thin, meaning that the blocks were small, yielding low signals.

Ages were calculated from these data sets using different approaches (Fig. S3). In Bern ages are calculated using a ^{238}U - ^{204}Pb vs. ^{206}Pb - ^{204}Pb isochron followed by a Monte Carlo simulation calculation to factor in the initial $^{234}\text{U}/^{238}\text{U}$ disequilibrium, which is constrained by measuring the residual ($^{234}\text{U}/^{238}\text{U}$) disequilibrium still present in the sample (Table S2). For more details see (S1). The calculated initial ($^{234}\text{U}/^{238}\text{U}$) activity ratio is 4.34 ± 0.39 . In Melbourne ages are calculated using an ^{238}U - ^{206}Pb vs ^{207}Pb - ^{206}Pb inverse concordia diagram. The initial ($^{234}\text{U}/^{238}\text{U}$) equilibrium is normally factored into the age calculation by using an assumed initial disequilibrium and running this through a solver macro in excel. This procedure relies on measurements of present-day dripwater or young speleothems from the same site and could not be followed in this case. Also, previously determined initial ($^{234}\text{U}/^{238}\text{U}$) activity ratios of speleothems in the Cradle of Humankind heritage site are strongly heterogeneous (S1), ranging from 2.5 to 6.9, and do not provide a guideline. Therefore, the present-day value measured in Bern was used (Table S2), and the calculation adapted to utilize this parameter. The calculated initial ($^{234}\text{U}/^{238}\text{U}$) activity ratio was identical to the value listed above, and thus well within the range of previously determined ones.

Text S2. Magnetostratigraphy of the Malapa site.

A series of 8 independently oriented samples (UW88-PM01-07 & 09) were taken from the Malapa site (Figs S1, S4). The samples were taken as block samples and were oriented in situ using a Suunto magnetic compass and clinometer. Subsequent corrections were made for the

local dip of the stratigraphy and the declination of the local field according to the International Geomagnetic Reference Field (IGRF), accessed through the British Geological Survey (<http://www.geomag.bgs.ac.uk/gifs/igrf.html>). Three block samples (UW88-PM01, 02 and 03) were taken from the basal flowstone layers, and five samples were taken from the overlying hominin-bearing deposits: UW88-PM04 from facies C; UW88-PM05 from facies D, and UW88-PM06 and UW88-PM07 from facies E (Fig. S3). Sample UW88-PM09 was taken across an erosional contact between facies C and facies E along the NW sidewall of the cave. More concentrated sampling was not possible at this time due to the density of fossils within the deposits. This also limited the size of the blocks sampled.

A series of standard mineral magnetic measurements were undertaken on the sediment blocks (see 5 for methodology) to establish the origin of the magnetic remanence preserved within the sediments. Dual frequency, magnetic susceptibility measurements were undertaken using the Bartington MS2B and χ/T system for frequency-dependant, room-temperature and low-temperature analysis, down to -196°C . Isothermal Remanent Magnetization (IRM) acquisition curves and backfields, hysteresis loops and Curie curves were run on a Magnetic Measurements Variable Field Translation Balance (VFTB). Stepwise demagnetisation was undertaken using a laboratory built alternating field demagnetizer capable of imparting fields as high as 100mT, and a Magnetic Measurements Thermal Demagnetizer (MMTD).

Measurements were made using an AGICO JR6 spinner magnetometer. The samples' characteristic remanent magnetizations (ChRM) were isolated using a combination of cleaning methods (Fig. S5). Firstly, the samples were subjected to a 10-16 point alternating field demagnetization (AFd). This indicated that a strong viscous overprint occurred in many of the samples, but was typically removed by 12-15mT to reveal a stable ChRM. Stability of

remanence during AFd varied from sample to sample, but ranged between 30 and 100mT. A 10 point stepwise thermal demagnetization of sister specimens was undertaken on the clastic deposits. Additionally, a hybrid method was also undertaken on another set of sister specimens. This involved an AFd cleaning step at 12-15mT, followed by a 10 point stepwise thermal demagnetization. This was undertaken to ensure that the strong viscous overprint was being successfully removed before any high temperature alteration of the specimens occurred.

After magnetic cleaning, ChRMs were determined using principle component analysis (*S6*). Samples were deemed acceptable if they had a mean angle of deviation (MAD) less than 10°. Fisher statistics (*S7*) were utilized to determine 'virtual geomagnetic pole latitude' (VGPlat) for each block sample or layers within each block sample. This produced a sequence of polarity intervals and reversals that were then correlated to the globally known dated record of polarity changes, or Geomagnetic Polarity Time scale (GPTS; *S8*) to produce potential age ranges for the various deposits and site as a whole (Table S3).

Mineral magnetic measurements indicate that both magnetite and maghaemite occur in grain sizes from superparamagnetic (SP) to stable single domain (SSD). A high proportion of viscous single domain (vSD) to superparamagnetic boundary grains are shown by a high frequency dependence of magnetic susceptibility (~9%), and these grains are responsible for the strong, but soft viscous overprint seen in all the samples. Low temperature magnetic susceptibility measurements also indicate an SP-vSD grain size range with no evidence for multi-domain particles. This overprinting remanence is removed by AFd to between 12 and 15 mT or temperatures in excess of 250-325°C to reveal a weak, but stable primary remanence formed during deposition within the cave.

Samples PM06 and PM07 gave inconsistent directions of magnetisation from one sub-sample to another and generally gave randomly oriented directions. Over half of the sub-samples from PM05 also gave inconsistent random directions due to the presence of a large clast of dolomite in the middle of the sample. The random directions from a number of the block samples are considered to be due to the breccia-like nature of these samples, and the inclusion of fragments of older cave sediments and country rock within the deposits. In contrast sample PM09 gave consistent normal polarity directions of magnetization due to the formation of stabilizing layers of calcite during its deposition. Equally, the base of sample PM04 gave consistent normal polarity directions for a similar reason. Two sub-samples from PM05 also recorded a stable normal magnetic polarity. The upper part of PM04 also gave consistent directions of magnetization perhaps due to its more fine grained nature. However, this sample records an intermediate direction of magnetization similar to a sub-sample direction from the base of PM05. All sub-samples from the upper part of the flowstone (PM03 and 02) record a stable reversed polarity and show a swing from negative to positive directions during stepwise demagnetization as the viscous overprint is removed (Fig. S5). The basal flowstone sample (PM01) records a normal magnetic polarity.

The fauna assemblage associated with the hominin fossils indicates that the sediments at Malapa were deposited between 2.36 Ma and 1.5 Ma. In this time period a number of short duration geomagnetic excursions or events are known to occur, but their precise age and sequence has been a matter of debate (S9). The best defined and longest of these is the Olduvai normal polarity Subchron between 1.95 and 1.78 Ma. The R union Subchron has been argued to consist of just a single normal polarity event or two events (R union I and R union II) that have been dated in different locations to various ages between 2.31 and 2.07 Ma. A third normal

polarity excursion, the Huckleberry Ridge Subchron has also been proposed, and is dated to 2.059 ± 0.04 Ma at the type locality (*S10*), but some argue that this may represent the same event as R union II (*S9*). Whether R union I, R union II and Huckleberry Ridge represent three distinct events or just two events remains a topic of debate. (*S9*) only identified two normal polarity excursions in a study of the Omo Valley in Ethiopia. The older event was dated to 2.21-2.14 Ma and the younger to 2.09-2.05 Ma. Similarly, (*S11*) identified a single normal polarity event at 2.153–2.115 Ma and anomalous directions at ~2.04 Ma in ODP site 981. This data suggests that perhaps only two normal polarity events occur, the older R union I event and the younger R union II or Huckleberry Ridge. Due to the fact that only the older event seems to occur on the island of R union, it has been suggested that the younger, shorter excursion is best referred to as the Huckelberry Ridge event (*S10*).

The U-Pb age (2.026 ± 0.021 Ma) for the flowstone from Malapa suggests that the normal polarity zone identified near the base of the otherwise reverse polarity flowstone represents the Huckleberry Ridge event (aka R union II) consistent with the U-Pb age assessment. The normal polarity zone identified in the overlying hominin-bearing deposits would, therefore represent the Olduvai Subchron at 1.95 Ma to 1.78 Ma giving the maximum extent of the age range for the *Au. sebiba* fossils from facies D (Table S3). The occurrence of stable intermediate directions of magnetization in facies C may suggest that this deposit formed soon after the reversed flowstone stopped growing, and during the transition to the Olduvai Subchron at ~1.95 Ma.

Text S3. Cosmogenic isotope study

At site TNHL08 (Fig. S6), samples were collected from pure quartz veins in chert breccia. At site LH08 (Fig. S6), samples were collected from a weathering resistant, chert breccia layer, which forms a gently NW dipping dip slope along the southern side of the valley. Quartz purification and separation of beryllium were done at the University of California, Santa Cruz, following Kohl and Nishiizumi (*S12*). The $^{10}\text{Be}/^9\text{Be}$ ratio measurements were made at the Center for Accelerator Mass Spectrometry of the Lawrence Livermore National Laboratory (LLNL) and normalized to LLNL standards (sample parameters and specific standards are provided in Table S4).

At TNHL08, given the measured radionuclide abundances and known antiquity of the African Erosion Surface, the erosion rate (ε) can be determined from the relation:

$$\varepsilon = \left(\frac{P}{N - \lambda} \right) / \left(\frac{\rho}{\Lambda} \right)$$

Where P is the local site production rate, N the measured radionuclide inventory, λ the disintegration constant ($\text{Be} = 5.10 \pm 0.26 \cdot 10^{-7} \text{ yr}^{-1}$; *S13*), ρ the density and (2.6 g/cm^3) and Λ the attenuation rate (177 g/cm^2 ; *S14*).

To establish incision rates, we have directly dated a bedrock section of the Grootvleispruit river exposed by incision of the river (Fig. S7). At LH08, we sampled and dated a dipping chert surface of exposed bedrock forming the channel of the Grootvleispruit, which is a bedrock stream throughout the upper reaches of its catchment (i.e. the section of the river that drains the dolomitic units of the Malmani Subgroup and overlying shale belonging to the Time Ball Hill Formation of the Pretoria Group; *S15*). At the site, the dipping chert horizon shows

clear evidence of fluvial erosion with pot holes and fluvial, polished surfaces, and along the sampled section there is no evidence of paleo-fluvial terraces. Thus, by dating the chert horizon, we can directly obtain the age altitude relationship of the paleo-stream channel, and derive the incision rate of that river for the last 110 ka.

For the determination of the river down-cutting rate, we fit a simple linear function to the height above the active channel of the samples and the age (Fig. S8). In order to provide a common reference for the sample ages, the reported sample ages were determined using the CRONUS-Earth Online Age Calculator (*S16*). The ages and errors reported use the constant production rate model, which yields the most conservative down cutting rates. All the time-varying production models give model ages that are 7-10% younger.

Figures and Tables

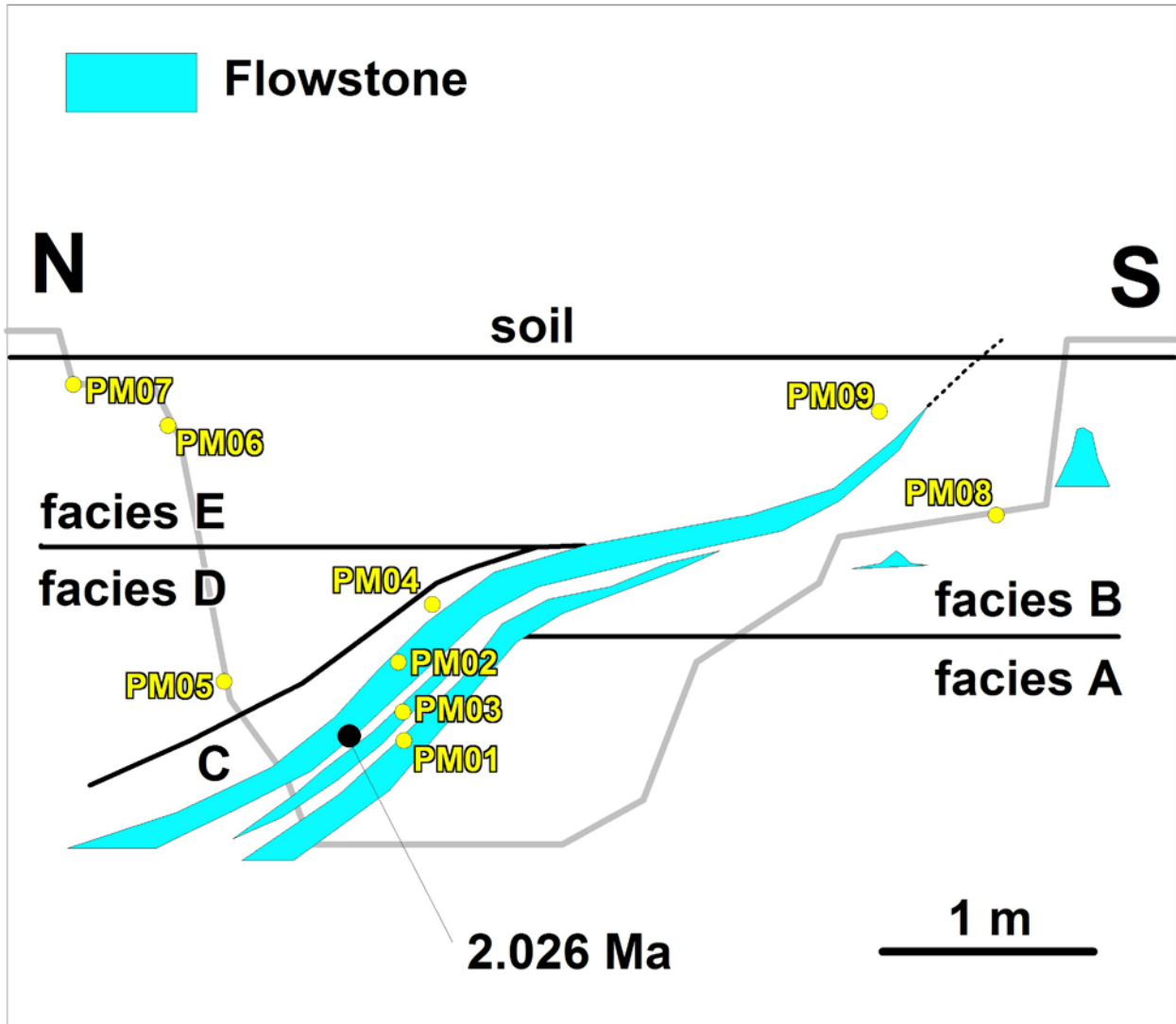


Fig. S1. Schematic north-south section through Malapa pit illustrating the vertical distribution of facies A-E relative to the central flowstone sheet. The flowstone is intercalated with thin layers of clastic sediment. The relative positions of the U-Pb dating sample (2.026 ma) and the palaeomagnetic samples (PM01-09) have been indicated. Further details regarding the exact sample positions are shown in figures 2 and S4.

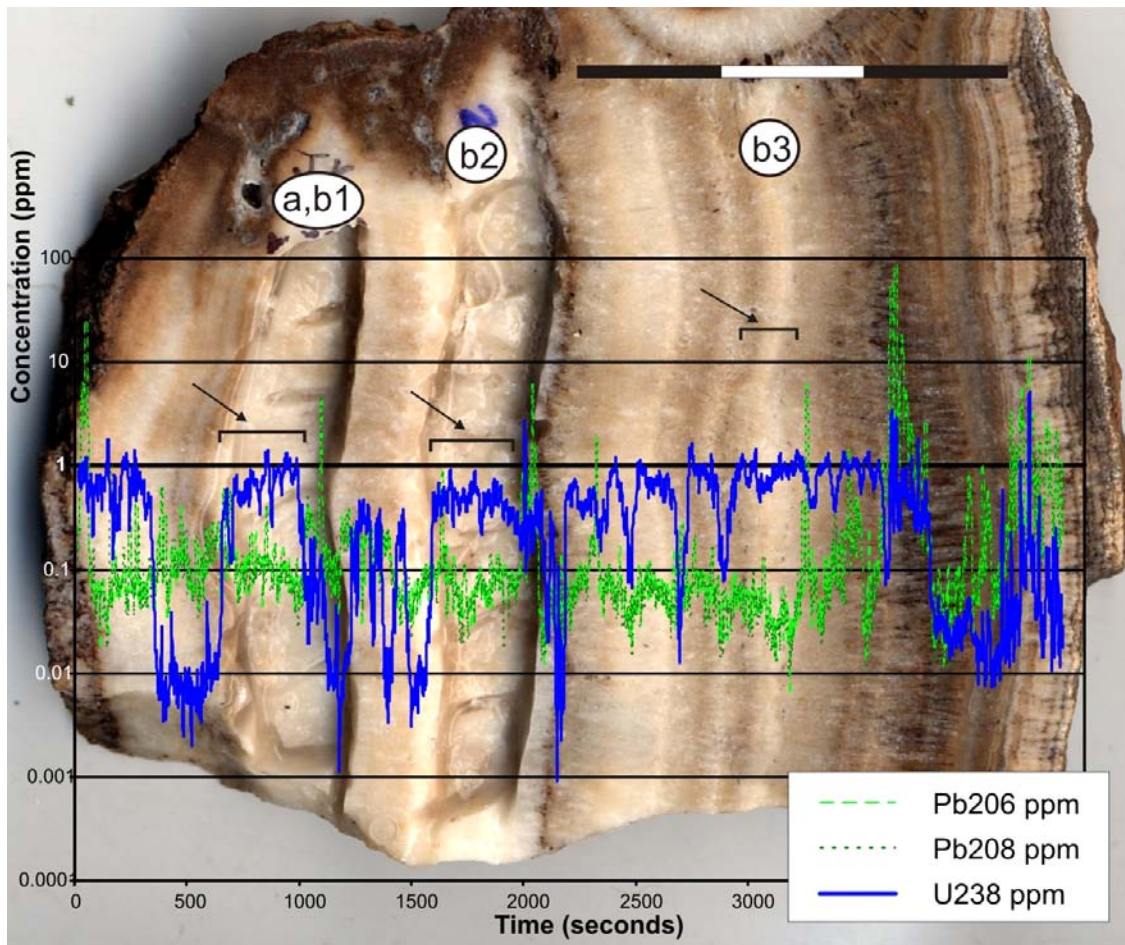


Fig. S2. Laser ablation data (U and Pb concentrations) plotted against time and superimposed on sample NHL 09/2b. U-rich layers b1 and b2 were cut out for dating in Melbourne. Layer b1 corresponds to layer 'a' from sample NHL 09/2a dated in Bern. Scale bar in centimetres.

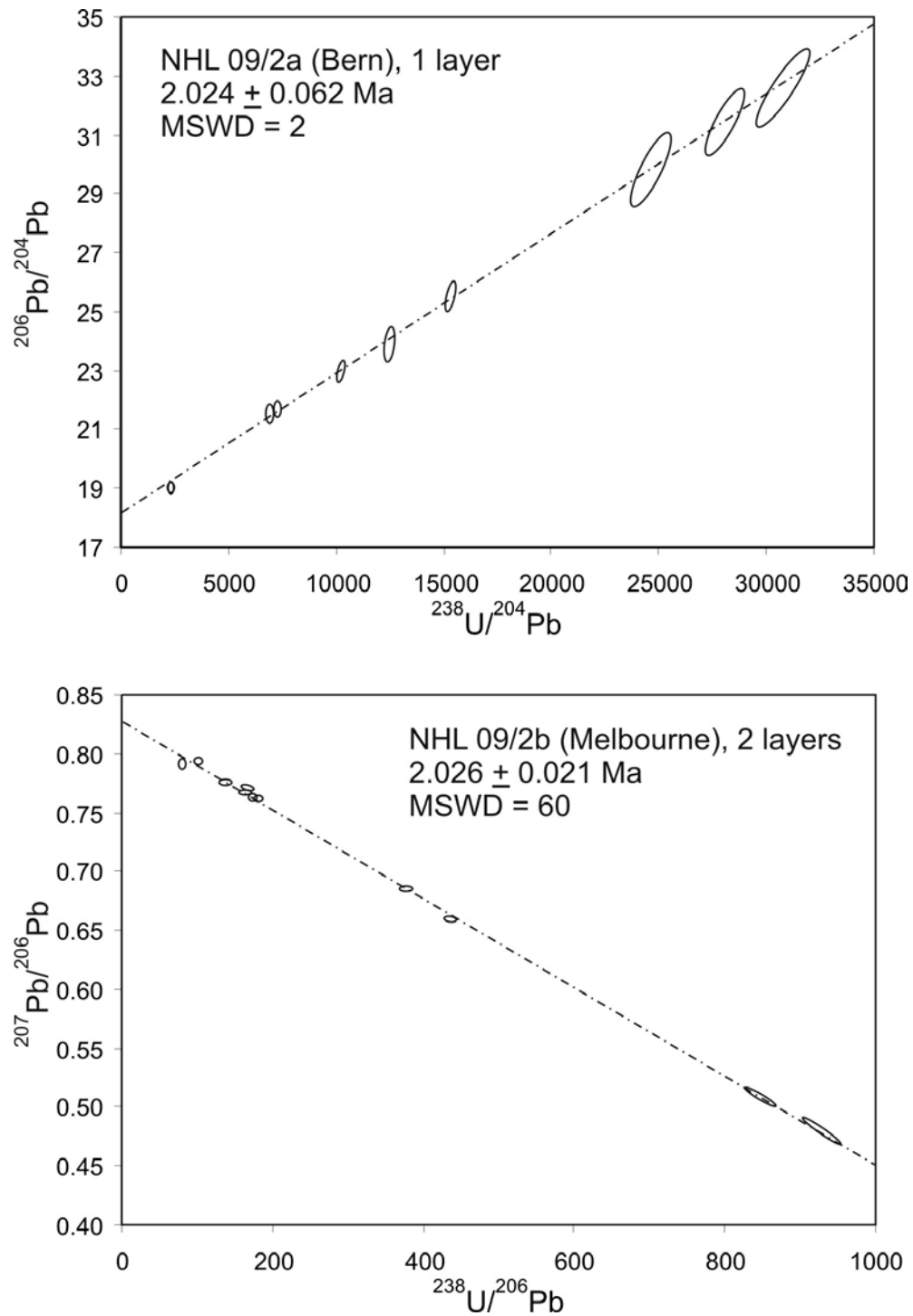


Fig. S3. U-Pb isochron diagrams and dating results for flowstone samples NHL09/2a and NHL09/2b.

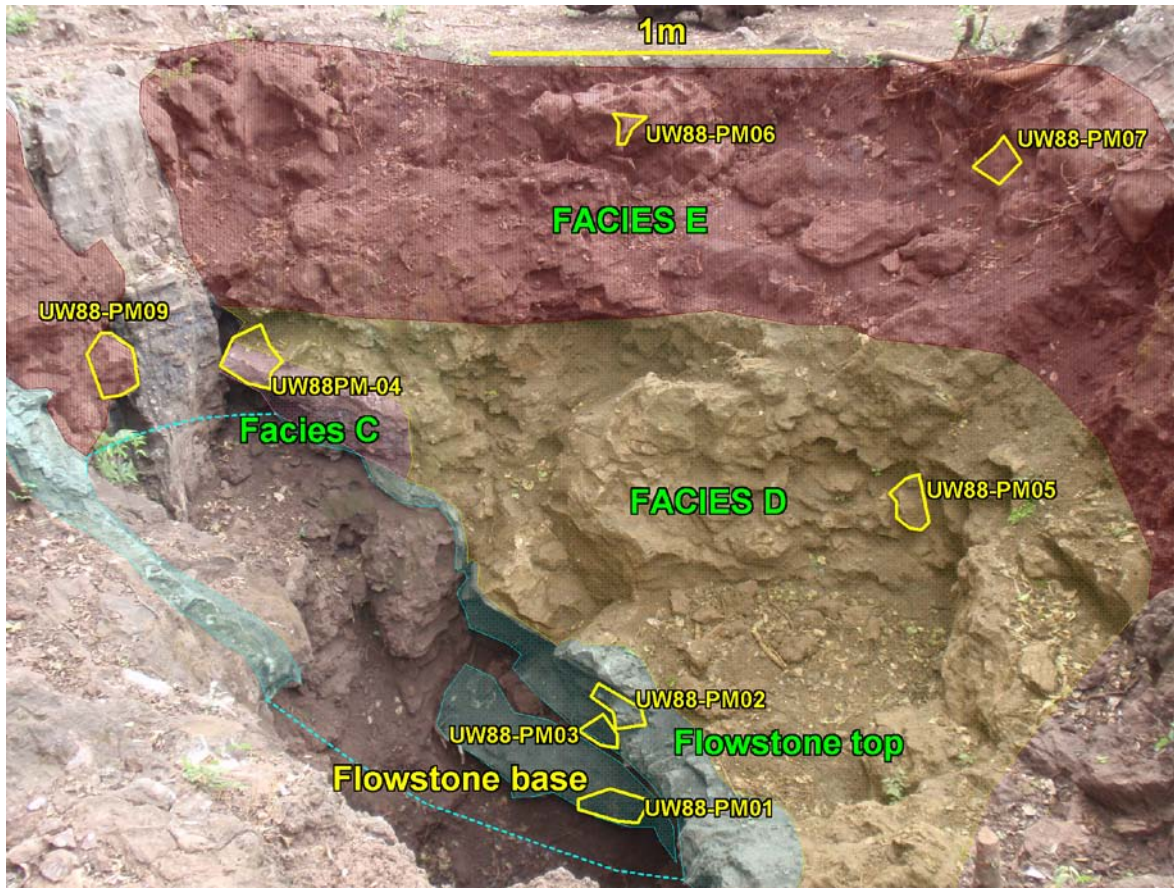


Fig. S4. View of the north face of Malapa pit showing the position of the samples taken for paleomagnetic analysis relative to the different rock types.

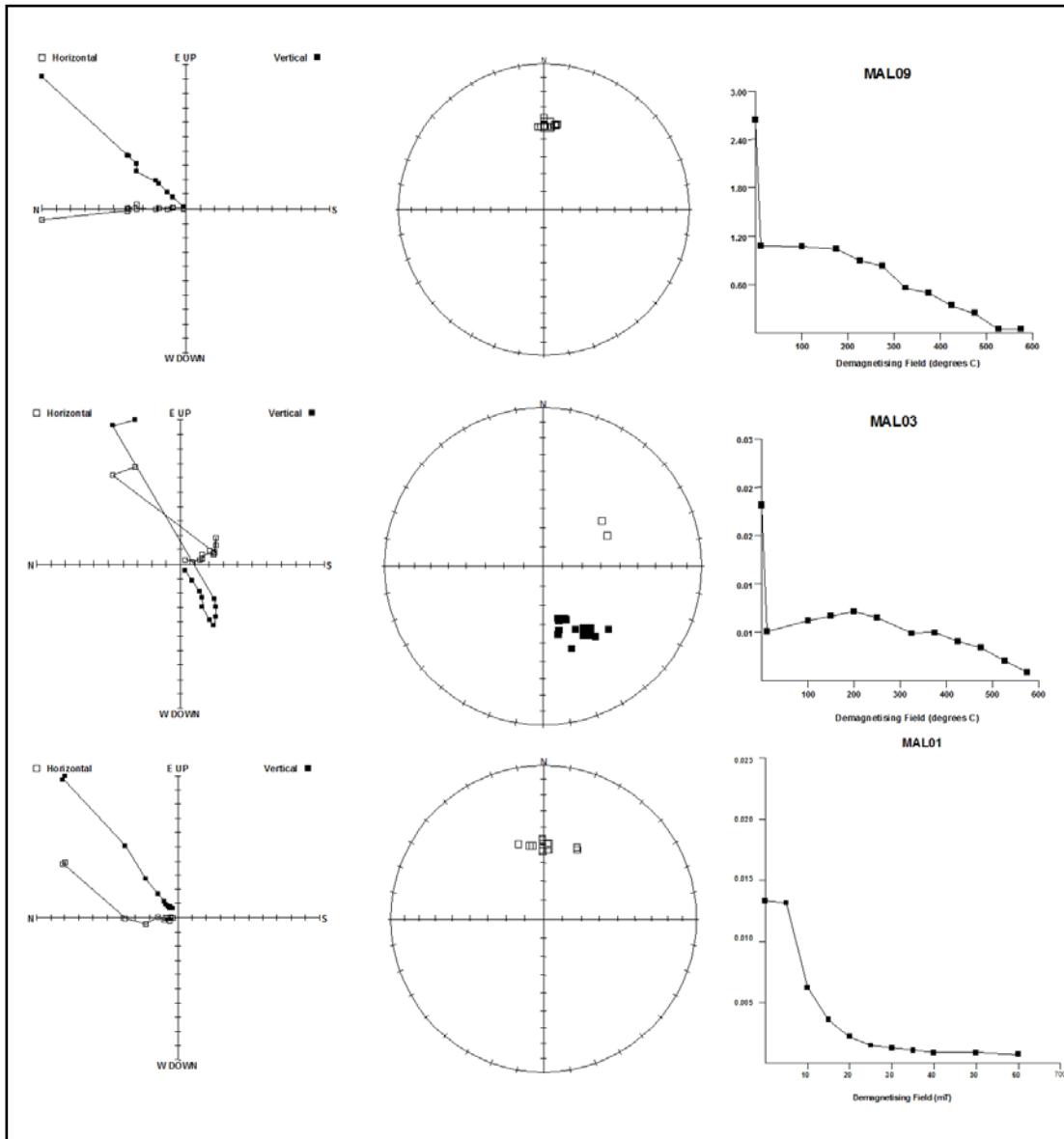


Fig. S5. Orthogonal, stereo and intensity (A/m) plots for reversed polarity palaeomagnetic sample UW88-PM03 (flowstone) and normal polarity samples UW88-PM09 (facies D) and PM01 (flowstone); marked Mal03, Mal09 and Mal01. Samples PM03 and PM09 were demagnetized using the hybrid AF and thermal demagnetization methods, and PM01 using standard alternating field demagnetization.

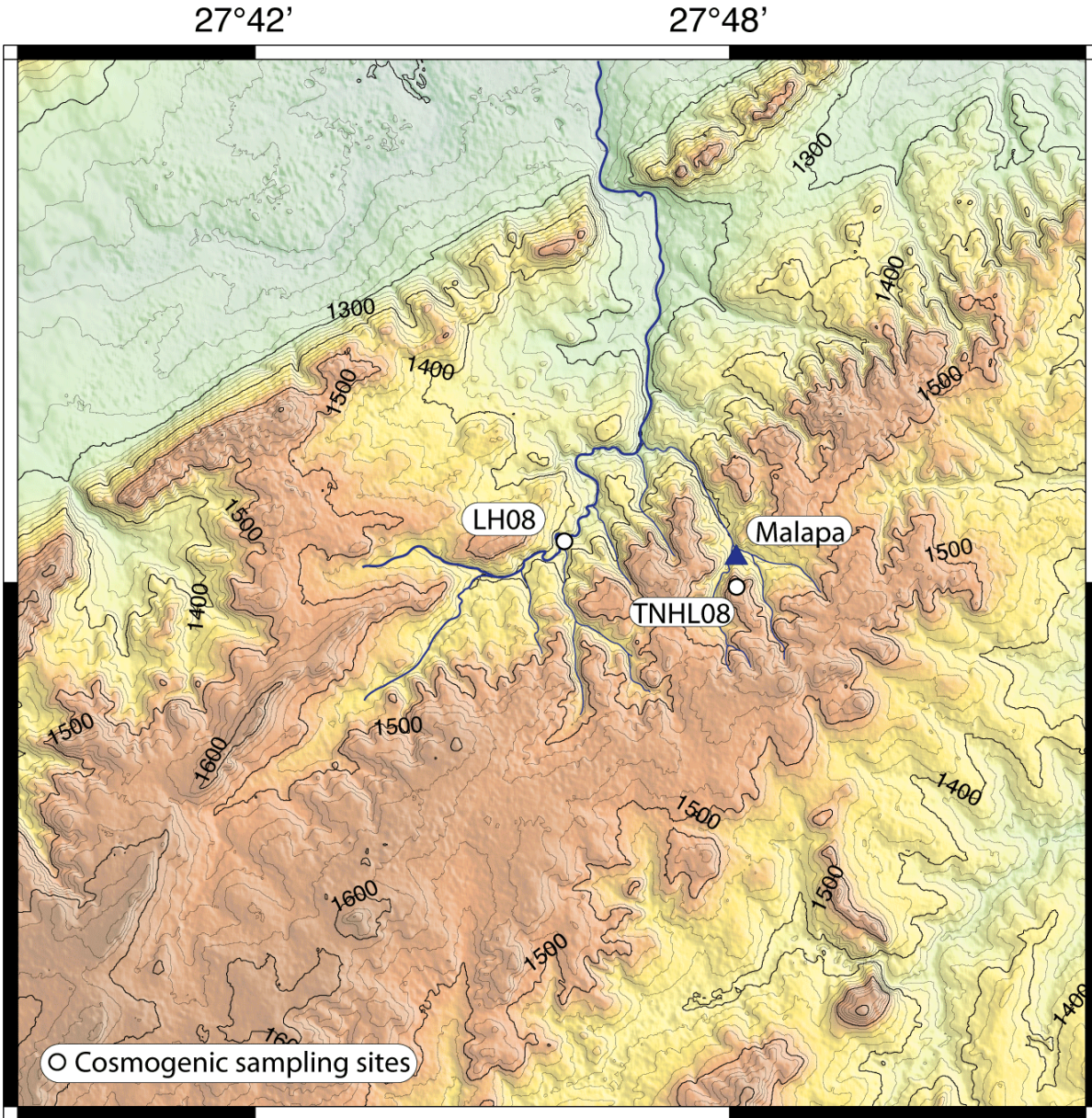


Fig. S6. map illustrating the geomorphology of the area around Malapa and showing the cosmogenic sampling sites marked at ‘Little Heaven’ (LH08) and the plateau south of Malapa (TNHL08).

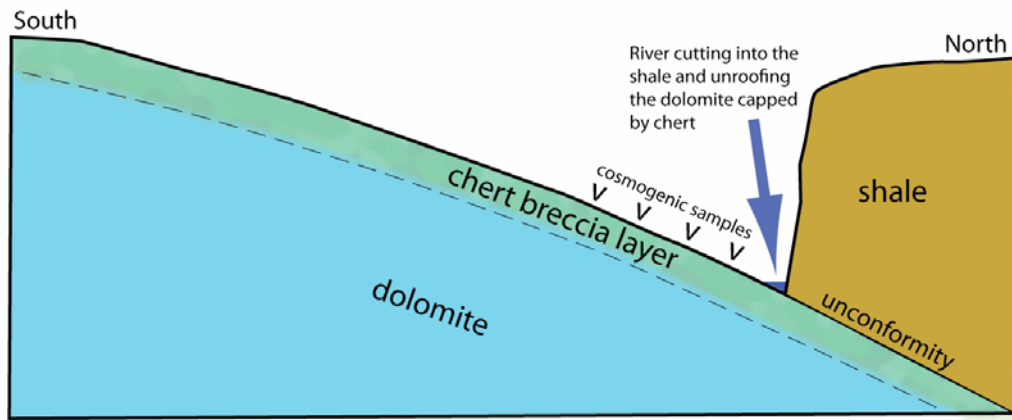


Fig. S7. Section illustrating the geological and geomorphological position of cosmogenic samples taken at site LH08. The samples were taken along a dip slope of gently NW dipping chert breccia capping dolomite of the Malmani Subgroup. Overlying shale of the Time Ball Hill Formation was removed by river incision along the chert layer.

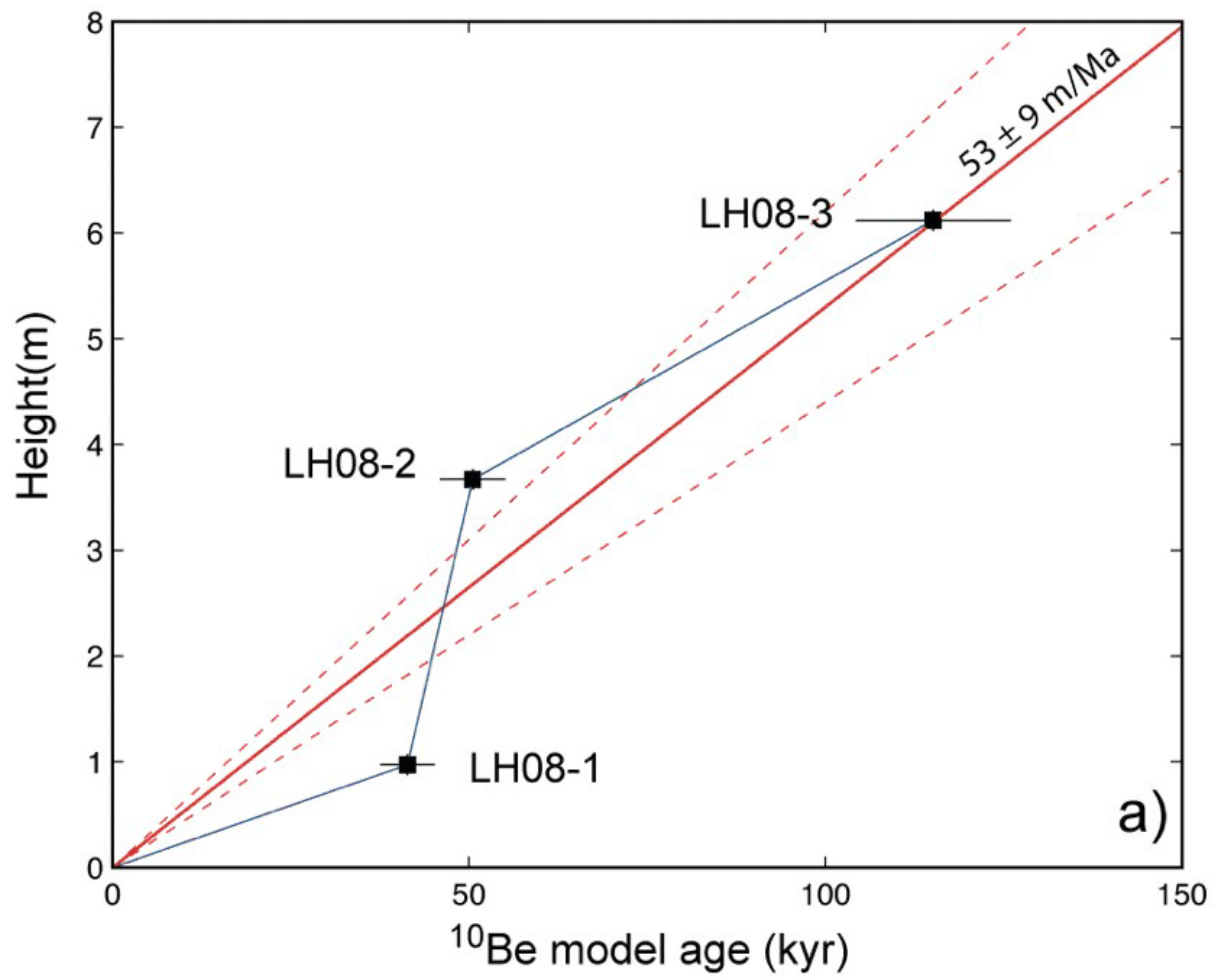


Fig. S8. Little Heaven cosmogenic sampling site (sample LH08). The plot shows the sample height above the stream bed vs. the ^{10}Be model age from which an average down-cutting rate of 53 ± 9 m/m.y. has been calculated.

Table S1. Combined U-Pb isotopic data from Bern (*) and Melbourne for flowstone samples NHL09-2a and NHL09-2b

Sample	Wt. (mg)	U ($\mu\text{g/g}$)	Pb ($\mu\text{g/g}$)	$\left(\frac{^{234}\text{U}}{^{238}\text{U}}\right)$	2SE	$\frac{^{238}\text{U}}{^{206}\text{Pb}}$	2SE	$\frac{^{238}\text{U}}{^{204}\text{Pb}}$	2SE	$\frac{^{207}\text{Pb}}{^{206}\text{Pb}}$	2SE	$\frac{^{206}\text{Pb}}{^{204}\text{Pb}}$	2SE	$\frac{^{207}\text{Pb}}{^{204}\text{Pb}}$	2SE	$\frac{^{208}\text{Pb}}{^{204}\text{Pb}}$
*NHL 09-2a 1	106.9	0.811	0.0069	1.0098	0.0017			7250	88			21.69	0.31	15.61	0.23	37.62
*NHL 09-2a 2	80.9	0.861	0.0024	1.0119	0.0016			24610	973			29.80	1.28	15.68	0.73	36.97
*NHL 09-2a 3	131.7	0.865	0.0037	1.0094	0.0014			15303	280			25.51	0.54	15.65	0.35	37.55
*NHL 09-2a 5	86.4	0.921	0.0047	1.0118	0.0018			12460	260			23.88	0.58	15.66	0.41	37.52
*NHL 09-2a 5a	79.1	0.908	0.0237					2277	17			19.00	0.18	15.52	0.15	37.67
*NHL 09-2a 6	91.2	0.946	0.0022	1.0125	0.0016			30745	1220			32.61	1.40	15.85	0.75	37.21
*NHL 09-2a 7	102.9	0.924	0.0023	1.0117	0.0016			28034	937			31.40	1.14	15.82	0.63	37.45
*NHL 09-2a 8	106.4	0.968	0.0060	1.0107	0.0014			10204	147			22.96	0.39	15.63	0.28	37.61
*NHL 09-2a 9	100.8	0.937	0.0085	1.0116	0.0014			6846	83			21.51	0.32	15.65	0.24	37.87
NHL 09/2b/1-1	165.9	0.616	0.004			435.7	5.3	10557	183	0.6589	0.0030	24.23	0.14	15.97	0.10	
NHL 09/2b/1-2	201.9	0.681	0.0282			79.1	0.1	1575	3	0.7914	0.0040	19.91	0.10	15.76	0.07	
NHL 09/2b/1-4	184.8	0.822	0.0064			377.1	2.7	8741	84	0.6849	0.0016	23.18	0.07	15.88	0.05	
NHL 09/2b/1-5	128.5	0.872	0.0022			927.8	21.6	31693	1494	0.4807	0.0100	34.16	0.84	16.42	0.38	
NHL 09/2b/1-6	147.8	0.861	0.0025			847.0	15.8	27201	963	0.5079	0.0075	32.11	0.55	16.31	0.29	
NHL 09/2b/2-1	161.7	0.531	0.0097			174.0	1.0	3601	25	0.7625	0.0008	20.70	0.03	15.78	0.03	
NHL 09/2b/2-2	116.1	0.547	0.0106			165.8	1.2	3384	30	0.7702	0.0010	20.41	0.03	15.72	0.03	
NHL 09/2b/2-3	136	0.626	0.0112			178.4	1.1	3710	27	0.7611	0.0008	20.79	0.03	15.82	0.02	
NHL 09/2b/2-4	89.6	0.608	0.0119			164.3	1.4	3379	36	0.7667	0.0012	20.57	0.07	15.77	0.05	
NHL 09/2b/2-5	127.1	0.583	0.0137			137.5	0.7	2799	18	0.7755	0.0007	20.36	0.04	15.79	0.03	
NHL 09/2b/2-6	93.4	0.476	0.0151			103.3	0.7	2046	16	0.7933	0.0007	19.80	0.03	15.71	0.02	
NHL 09/2b/3-1	19.7	0.33	0.0148			75.4	2.5	1475	56	0.7928	0.0037	19.56	0.18	15.51	0.12	
NHL 09/2b/3-2	34.3	0.476	0.0103			151.8	4.0	3103	98	0.7663	0.0037	20.44	0.13	15.66	0.09	
NHL 09/2b/3-3	39.3	0.569	0.0122			151.8	2.9	3129	73	0.7650	0.0028	20.61	0.11	15.77	0.08	
NHL 09/2b/3-4	37.9	0.357	0.011			106.9	2.4	2173	58	0.7806	0.0029	20.33	0.12	15.87	0.08	
NHL 09/2b/3-5	37.8	0.59	0.0156			124.0	1.9	2515	48	0.7803	0.0021	20.28	0.09	15.82	0.06	
NHL 09/2b/3-6	67.8	0.429	0.0191			74.3	0.5	1457	12	0.7987	0.0012	19.60	0.04	15.65	0.03	

Table S2. Summary of ($^{234}\text{U}/^{238}\text{U}$) activity ratios for spiked and unspiked runs conducted in Bern

	Value	2SE	2SD
*Average of NHL 09-2a spiked runs (Table S1).	1.0112		0.0023
*NHL 09-2a 4a (unspiked) run 1	1.0096	0.0012	
*NHL 09-2a 4a (unspiked) run 2	1.0109	0.0012	
*NHL 09-2a 4a (unspiked) run 3	1.0104	0.0026	
*Average of NHL 09-2a 4a (unspiked)	1.0103		0.0013

Table S3. Palaeomagnetic data for the Malapa site showing the transition from normal (N) polarity during the Huckleberry Ridge (HR; 2.06 ± 0.04 Ma) event to reversed (R) polarity during the Matuyama Chron (MTY; 2.06 ± 0.04 - 1.95 Ma) and back to normal polarity during the Olduvai Subchron (OLD; 1.95 - 1.78 Ma). No. represents the number of successful sub-samples versus the total number of sub-samples taken from a sample block.

Sample	Facies	Declination	Inclination	α_{95}	No.	VGP latitude.	Polarity	(Sub) Chron
UW88-PM06	E	x	x	x	0/3	x	x	
UW88-PM07	E	x	x	x	0/3	x	x	
UW88-PM09 upper	E	2.7	-43.4	4.8	3/3	87.6	N	OLD
UW88-PM09 lower	C	340.5	-44.0	12.3	2/2	72.4	N	OLD
UW88-PM05	D	344.6	-48.1	55.6	2/5	75.9	N	OLD
UW88-PM04 upper	C	37.3	-5.0	6.7	3/3	47.4	IN	OLD
UW88-PM04 lower	C	29.9	-41.1	13.9	2/2	62.7	N	OLD
UW88-PM02	Flowstone	199.4	61.4	8.4	3/3	-66.7	R	MTY
UW88-PM03	Flowstone	167.7	65.4	8.0	4/4	-66.0	R	MTY
UW88-PM01	Flowstone	1.9	-52.2	3.3	4/4	82.7	N	HR

Table S4. Summary of results from cosmogenic sampling sites TNHL08 and LH08

Sample name	Latitude ¹	Longitude ¹	Elevation ¹	Thickness	Density	Shielding	Erosion Rate	¹⁰ Be	error	Be AMS	Erosion rate	External error	Model age	Internal error	Elevation above stream channel ²
	(DD)	(DD)	(m)	(cm)	(g/cm ³)		(cm/yr)	(atoms/g)	(atoms/g)	(standard)	(m/My)	(m/My)	(ky)	(ky)	(m)
TNHL08	-25.90	27.80	1524												
TNHL08-1				2.0	2.6	1	-	2160733	39068	07KNSTD	2.8	0.3	-	-	-
TNHL08-2				2.0	2.6	1	-	1445020	41736	07KNSTD	4.5	0.5	-	-	-
TNHL08-3				2.0	2.6	1	-	2317687	71013	07KNSTD	2.6	0.3	-	-	-
TNHL08-4				2.0	2.6	1	-	1402200	33657	07KNSTD	4.6	0.4	-	-	-
LH08	-25.89	27.76	1367												
LH08-1				2.0	2.6	0.94	5.00E-5	393236	10116	07KNSTD	-	-	41.39	1.08	0.97
LH08-2				2.0	2.6	0.94	5.00E-5	478748	10770	07KNSTD	-	-	50.54	1.16	3.62
LH08-3				2.0	2.6	0.97	5.00E-5	1100691	29537	07KNSTD	-	-	115.15	3.21	6.12

¹ Production rates of ¹⁰Be at each site were calculated using an average location given by a GARMIN GPS.

² Relative heights were measured using an inclinometer and tape measure.

References

- S1. R. Pickering, J.D.Kramers, T.C. Partridge, Quaternary Geochron., in press.
- S2. J.Woodhead, J.Hellstrom, J.Hergt, A. Greig, R. Maas, J. Geostand. Geoanal. Res., 31, 331-343 (2007).
- S3. R. Pickering, A new Uranium-Lead chronology for the early hominin bearing caves of South Africa. Unpublished Ph.D thesis, University of Bern, 165pp (2009)
- S4. J.D. Woodhead, J.Hellstrom, R.Maas, R. Drysdale, G. Zanchetta, P. Devine, E. Taylor, Quaternary Geochron 1, 208-221 (2006)
- S5. J. Walden, F. Oldfield, J. Smith, Environmental Magnetism: a practical guide, (Quaternary Research Association Technical Guide. V. 6, London, 1999)
- S6. J.L. Kirschvink, Geophys. J. Roy. Astro. Soc. 62, 699-718 (1980)
- S7. R. Fisher, Phil. Trans. R. Soc. London A. 306, 295-305 (1953)
- S8. J.G. Ogg, A.G. Smith, in A Geologic Time Scale 2004, F. Gradstein, J.G. Ogg, A.G. Smith Eds., (Cambridge University Press; UK, 2004), pp 63-86.
- S9. T. Kidane, Y Otofujii, Y. Komatsu, H. Shibasaki, J. Rowland. Earth Planet. Sci. Lett. 262, 240-256 (2007)
- S10. M.A. Lanphere, D.E. Champion, R.L. Christiansen, G.A. Izett, J.D. Obradovich, GSA Bull. 114, 559-568 (2002)
- S11. J.E.T. Channell, J. Labs, M.E. Raymo, Earth Planet. Sci. Lett. 215, 1-12. (2003)
- S12. C. P. Kohl, K. Nishiizumi, Geochim. et Cosmochim. Ac. 56, 3583-3587 (1992)
- S13. K. Nishiizumi, M. Imamura, M. Caffee, J. Southon, R. Finkel, J. McAnich. Nucl. Instrum. Met. B 258, 403-413 (2007)
- S14. D.L. Farber, A.S. Meriaux, R.C. Finkel, Earth Planet. Sci. Lett. 274, 295-300 (2008)
- S.15 P.G. Eriksson *et al.*, in *The Geology of South Africa*, M.R. Johnson, C.R. Anhaeusser, R.J. Thomas, Eds. (Geol. Soc. S. Afr., Johannesburg, 2006), pp. 237-260.
- S16. G. Balco, J. O. Stone, N. A. Lifton and T. J. Dunai, Quaternary Geochron., 3, 174-195 (2008)